

**STRUCTURAL AND DAMAGE ASSESSMENT OF MULTI-SECTION
MODULAR HYBRID COMPOSITE WIND TURBINE BLADE**

A Dissertation

by

NORIMICHI NANAMI

Submitted to the Office of Graduate and Professional Studies of
Texas A&M University
in partial fulfillment of the requirements for the degree of

DOCTOR OF PHILOSOPHY

Chair of Committee,	Ozden O. Ochoa
Committee Members,	Alan Palazzolo
	Thomas Strganac
	William Schneider
Head of Department,	Andreas A. Polycarpou

August 2014

Major Subject: Mechanical Engineering

Copyright 2014 Norimichi Nanami

ABSTRACT

Wind energy is one of the most promising and mature alternatives to satisfy the global demand for energy as the world population and the economic activity surge. The wind energy market has grown rapidly in the last couple of decades, boosting up the size of wind turbines to generate higher power output. Typically, the larger/longer blade designs rely on hybrid material systems such as carbon and/or glass fiber (CF/GF) reinforced polymers to improve specific stiffness/strength and damage tolerance. In addition to the operational loads such as aerodynamic loads, the blade is also exposed to various impact scenarios such as hail damage and bird strike where safe operation and subsequent safe shut down are of significant importance.

Herein, we propose a computational design concept that includes a multi-section modular hybrid composite wind turbine blade with successful joints while maintaining structural integrity and stability requirements. The configuration of the blade will simplify manufacturing-assembly processes and reduce expenses both in transportation and facilities requirements. The large-scale single continuous wind turbine blade is modeled based on our model of an 80 m blade with sandwich skin, spar cap and shear web reinforcements. The 80 m single continuous blade is employed to distinguish potential damage modes when subjected to aerodynamic as well as impact loads. The single continuous blade studies revealed that balsa core vs. foam core led to different damage initiation modes and that the blade provided sufficient damage tolerance below the operational loads associated with a wind speed of 8.9 m/s. Upon the 2 kg-bird impact

in the vicinity of the blade tip, the blade with operational preloading conditions provided adequate impact resistance due to the absence of damage in the composite layers and the balsa core. Our study showed that the modular blade followed the single length blade response without any significant alterations to its structural response. It is concluded that the proposed computational design concept that allow two modular blades to create full-length blade with sufficient joints is achievable. This modular concept can be easily extended for further multi-section modular blade designs.

DEDICATION

In loving memory of my father, *Seinosuke Nanami*, for inspiring my fascination in science, engineering, technology, and nature.

ACKNOWLEDGEMENTS

First of all, I would like to thank my committee chair, Dr. Ochoa, and my committee members, Dr. Palazzolo, Dr. Schneider, and Dr. Straganac, for their guidance and support throughout the course of this research. They have inspired and motivated me to work towards my academic goals. Working with them has been one of the most fantastic academic experiences for me.

Thanks also go to my friends and colleagues and the department faculty and staff, for making my time at Texas A&M University a wonderful experience. I would like to express my unending gratitude to my sweet girlfriend, Pilar. She has always been with me, and I don't have enough words to appreciate her.

I really appreciate the Pilant family and Mondragon family, provided valuable suggestions with the thesis and helped me to adapt to life in U.S. I cannot find any words to describe their hospitality during my time in Texas. I also want to extend my gratitude to the Texas A&M Energy Institute Energy Institute and ConocoPhillips, which awarded the 2012-2013 Energy Institute/ConocoPhillips Fellowship to support energy research by outstanding graduate students.

Finally, I dedicate this graduate research to my parents who have physically and mentally supported me to study in the U.S. I would not have been able to complete my graduate program without their encouragement and support through my academic career. I express my deepest respect and gratitude for their support and understanding during the long and arduous journey.

TABLE OF CONTENTS

	Page
ABSTRACT	ii
DEDICATION	iv
ACKNOWLEDGEMENTS	v
TABLE OF CONTENTS	vi
LIST OF FIGURES.....	ix
LIST OF TABLES	xiii
1. INTRODUCTION.....	1
1.1 Overview	1
1.2 Literature Review.....	6
1.2.1 Wind Turbine Blade Design.....	6
1.2.2 State-of-the-Art Wind Turbine Studies	12
1.3 Objective and Approach.....	16
2. TURBINE BLADE DESCRIPTION	17
2.1 Blade Geometry/Constraint Description	17
2.2 Material Selection/Composite Layup.....	20
2.3 Design Loads.....	24
2.3.1 Aerodynamic Loads	25
2.3.2 Impact Loads	27
3. COMPUTATIONAL SIMULATION.....	28
3.1 Element/Mesh Selection.....	28
3.1.1 Lagrangian Shell Elements.....	28
3.1.2 Lagrangian Solid Elements	30
3.1.3 Eulerian Elements.....	31
3.2 Loading and Boundary Conditions	32
3.2.1 Boundary Conditions.....	32
3.2.2 Static Analyses	32
3.2.2.1 Lift and drag loads.....	32
3.2.2.2 Flexural rigidity.....	34

3.2.3	Frequency Analyses	35
3.2.4	Impact Analyses	36
3.3	Constitutive Properties	37
3.3.1	Mechanical Behavior of Materials	37
3.3.1.1	Progressive damage in composites.....	37
3.3.1.2	Shear failure in isotropic materials.....	41
3.3.1.3	Elastic properties and allowables	42
3.3.2	Soft Body Impact Representation.....	43
3.3.2.1	Constitutive model	43
3.3.2.2	Representative bird geometry/material	45
3.3.2.3	Bird model validation.....	45
4.	THE SINGLE BLADE ASSESSMENT	47
4.1	Case Study Description	48
4.1.1	Core Material Comparison for Case Study I.....	48
4.1.2	Direct/Oblique Impact for Case Study II	49
4.1.3	The Blade with/without Preloads for Case Study II.....	50
4.1.4	Low Velocity Impactor Representation for Case Study II.....	52
4.1.5	The Target Structure Selections for Case Study II.....	53
4.2	Deformed Shape.....	54
4.2.1	Displacements Due to Operational Loads	54
4.2.2	Deformation Due to Impact.....	58
4.2.2.1	Deformed shape: Direct/oblique impacts	58
4.2.2.2	Deformed shape: Preloading conditions	61
4.2.2.3	Deformed shape: Lagrangian bird impact.....	63
4.3	Stresses, Strains, and Damage Mechanisms.....	67
4.3.1	Operational Loads	67
4.3.1.1	The SB model with balsa core.....	67
4.3.1.2	The SB model with H160 foam core.....	70
4.3.1.3	Structural integrity subsequent to local core damage.....	73
4.3.2	Impact Loads	75
4.3.2.1	Damage due to direct impact.....	75
4.3.2.2	Damage due to oblique impact.....	76
4.3.2.3	Impact response with preloading conditions.....	79
4.3.2.4	Lagrangian impactor representation.....	81
4.4	Energy Dissipation	84
4.4.1	Energy Balance of Direct Impact	84
4.4.2	Energy Balance in Lagrangian Bird Impact.....	85
4.4.3	Energy Balance of Bird Impact on the 5 m vs. 80 m Blade	87
4.5	Frequency	89
4.6	Discussion	92
4.6.1	Core Material Comparison for Case Study I.....	92
4.6.2	Direct/Oblique Impacts for Case Study II.....	93

4.6.3 The Blades with/without Preloads for Case Study II	94
4.6.4 Low Velocity Impactor Representation for Case Study II	94
4.6.5 The Target Structure Selections for Case Study II.....	95
5. MODULAR COMPOSITE WIND TURBINE BLADE STUDY	96
5.1 Introduction to the Cable Joint Concept.....	96
5.2 Modular Blade Representation.....	101
5.3 Structural Responses Analyses.....	106
5.3.1 Analysis Description	106
5.3.2 Displacement Results	106
5.3.3 Stress Results.....	108
5.3.4 Forces Generated by Cable Mechanisms	112
5.3.5 Natural Frequency Results	115
5.4 Discussion	116
6. CONCLUSIONS.....	118
REFERENCES.....	120
APPENDIX A	128
APPENDIX B	131
APPENDIX C	133
APPENDIX D	135
APPENDIX E.....	137
APPENDIX F	144

LIST OF FIGURES

	Page
Figure 1.1. Schematic of a typical horizontal-axis wind turbine.	3
Figure 1.2. Architecture of a computational blade model [18, 33, 34].	9
Figure 2.1. The 80 m blade: (a) dimensions of the blade, and (b) airfoil shapes.	18
Figure 2.2. Spar cap/shear web configuration.	19
Figure 2.3. Sections of the blade skin.	22
Figure 3.1. Boundary conditions for static analyses in the blade models.	32
Figure 3.2. Linear damage progression based on the equivalent stress-equivalent displacement relationship.	39
Figure 3.3. Progressive damage variable as a function of an equivalent displacement.	39
Figure 3.4. Eulerian bird impactor validation using impact test data on instrumented plates [50].	46
Figure 4.1. The bird described by EVF on the cross-sectional view at $r = 77.5$ m for the direct impact ($\theta = 0^\circ$) and oblique impact ($\theta = 30^\circ$) at $t = 0$ s.	50
Figure 4.2. The blade with preloads before bird impact: (a) deformed shape of the blade, and (b) A-A sectional view at $X = 77.5$ m.	51
Figure 4.3. The blade without preloads before bird impact: (a) virgin state of the blade, and (b) A-A sectional view at $X = 77.5$ m.	52
Figure 4.4. Global U_2 displacement contour of the SB model at $u_w = 8.9$ m/s: (a) balsa core, and (b) foam core.	54
Figure 4.5. Global U_3 displacement contour of the SB model at $u_w = 8.9$ m/s: (a) balsa core, and (b) foam core.	54
Figure 4.6. Flapping bending rigidity distribution for the SB models w/ balsa and foam cores.	56
Figure 4.7. Global U_2 displacement of the 5 m tip sectional blade: (a) 0.0025s, and (b) 0.01s.	58

Figure 4.8.	Motional states of the gel's EVF on the cross-sectional view at $r = 77.5$ m: (a) 0.001s, (b) 0.0025s, (c) 0.003s, and (d) 0.004s.	60
Figure 4.9.	The magnitudes of the global displacements of the FB-skin ($77 \text{ m} < r < 77.5 \text{ m}$) in the 5 m tip sectional blade: (a) 0.002s, and (b) 0.006s.....	61
Figure 4.10.	Global U_3 displacement in the lower blade skin of the preloaded blade ($75 \text{ m} < r < 80 \text{ m}$): (a) 0s, and (b) 0.010s.	62
Figure 4.11.	Global U_3 displacements in the lower blade skin of the blade without preloads ($75 \text{ m} < r < 80 \text{ m}$): (a) 0.001s, (b) 0.010s, and (c) 0.0125s.....	63
Figure 4.12.	Global U_3 displacements in the lower blade skin of the blade ($75 \text{ m} < r < 80 \text{ m}$) for the case of a Lagrangian impactor: (a) 0.002s, and (b) 0.005s.....	64
Figure 4.13.	The magnitudes of global displacements of the Lagrangian impactor: (a) 0.002s, and (b) 0.005s.....	66
Figure 4.14.	S_{11} stress contour of the upper blade skin ($46 \text{ m} < r < 80 \text{ m}$) at $u_w = 12$ m/s: (a) in the outermost GF fabric layer, and (b) in the balsa core.	68
Figure 4.15.	Von Mises stress contour in the balsa core ($46 \text{ m} < r < 80 \text{ m}$) at $u_w = 12$ m/s: (a) the upper blade skin, and (b) the web.....	69
Figure 4.16.	S_{11} stress contour in the outermost GF fabric layer of the upper blade skin at $u_w = 8.9$ m/s: (a) $5.6 \text{ m} < r < 46 \text{ m}$, and (b) $46 \text{ m} < r < 80 \text{ m}$	71
Figure 4.17.	S_{11} stress contour in the foam core of the upper blade skin at $u_w = 8.9$ m/s: (a) $5.6 \text{ m} < r < 46 \text{ m}$, and (b) $46 \text{ m} < r < 80 \text{ m}$	72
Figure 4.18.	Hashin matrix tensile mode in the webs ($60 \text{ m} < r < 70 \text{ m}$) at $u_w = 8.9$ m/s: (a) -45° UD-GF layer, and (b) $+45^\circ$ UD-GF layer.	72
Figure 4.19.	S_{11} stress distribution through shell thickness in the aft skin at $r = 40 \text{ m}$ at $u_w = 8.9$ m/s.....	74
Figure 4.20.	Equivalent plastic strain in the balsa core of the FB-skin and shear web (SW) at 0.006s.	75
Figure 4.21.	S_{22} stress in the outermost GF fabric of the lower FB-skin ($77 \text{ m} < r < 77.8 \text{ m}$): (a) 0.004s, and (b) 0.006s.....	76
Figure 4.22.	S_{22} stress in the innermost GF fabric of the lower FB-skin ($77 \text{ m} < r < 77.8 \text{ m}$): (a) 0.004s, and (b) 0.0045s.....	77

Figure 4.23. Von Mises stress in the balsa core of the lower FB-skin ($77 \text{ m} < r < 77.8 \text{ m}$): (a) 0.002s, and (b) 0.005s.....	78
Figure 4.24. S_{22} stress in the outermost GF fabric of the lower skin of the blade w/ preloads ($75 \text{ m} < r < 80 \text{ m}$): (a) 0s, (b) 0.001s, and (c) 0.010s.....	79
Figure 4.25. S_{22} stress in the outermost GF fabric of the lower skin of the blade w/o preloads ($75 \text{ m} < r < 80 \text{ m}$): (a) 0.001s, and (b) 0.010s.....	80
Figure 4.26. S_{22} stress in the outermost GF fabric of the lower skin of the blade w/o preloads ($75 \text{ m} < r < 80 \text{ m}$) for the case of the Lagrangian impact: (a) 0.002s, and (b) 0.005s.....	82
Figure 4.27. Von Mises stress in the balsa core of the lower skin of the blade w/o preloads ($75 \text{ m} < r < 80 \text{ m}$) for the case of the Lagrangian impactor at 0.002s.....	83
Figure 4.28. Kinetic and Internal energy balance of the whole system for the direct impact.	84
Figure 4.29. Kinetic energy balance of the Lagrangian bird impactor.	86
Figure 4.30. The magnitude of the impactor's velocities at 0.005s.	86
Figure 4.31. Kinetic energy balance of the impact models with the 5m and 80 m blades.	88
Figure 4.32. Internal energy balance of the impact models with the 5m and 80 m blades.	88
Figure 4.33. Comparison in frequencies between the SB models with balsa and foam cores.....	90
Figure 5.1. Tubular joint concept in discussion with Dr. W. Schneider.....	97
Figure 5.2. Schematic of the tubular joint concept applied for a cantilever.	99
Figure 5.3. Free body diagram of the inboard module at the joint region.	99
Figure 5.4. The conceptual schematic of the modular blade: (a) inboard and outboard modules, (b) joint-transition-region ($32 \text{ m} < r < 46 \text{ m}$), and (c) joint-reinforcement section ($36.9 \text{ m} < r < 41.1 \text{ m}$).....	102
Figure 5.5. Global U_3 displacement contours of the upper blade skin, $32 \text{ m} < r < 46 \text{ m}$: (a) SB Model, and (b) MB Model.	107

Figure 5.6.	S_{11} stress in the outermost GF fabric layer in the upper blade skin (5.6 m < r < 46 m): (a) SB Model, and (b) MB Model.....	108
Figure 5.7.	S_{11} stress in the outermost GF fabric layer in the upper blade skin (46 m < r < 80 m): (a) SB Model, and (b) MB Model.....	109
Figure 5.8.	S_{11} stress in the outermost GF fabric layer in the upper blade skin (32 m < r < 46 m): (a) SB Model, and (b) MB Model.....	110
Figure 5.9.	Von Mises stress in the balsa core of the upper blade skin (5.6 m < r < 46 m): (a) SB Model, and (b) MB Model.....	111
Figure 5.10.	S_{11} stress contour in the outermost layer of the joint region in the MB Model.....	113
Figure 5.11.	S_{11} stress distribution through shell thickness in the Joint-BS/SC region.	113

LIST OF TABLES

	Page
Table 2.1. Extracted geometrical specifications.....	18
Table 2.2. Lay-up used in the blade model	22
Table 2.3. Thickness distribution of the core material and proposed spar cap	23
Table 3.1. Loads at nine nodes along the rotor radius.....	34
Table 3.2. Linear elastic properties of composite materials.....	43
Table 3.3. Allowable strength, strain, and energy dissipation ratio	43
Table 4.1. Inertial properties of the blade models.....	49
Table 4.2. Tip displacements of the SB models w/ balsa and foam cores at 8.9 m/s.....	57
Table 4.3. S_{11} stress ratio in sandwich aft blade skin at $u_w = 8.9$ m/s	74
Table 4.4. Hinge spring stiffness in Nm.....	91
Table 5.1. Specifications of stainless cables and CFCCs.....	100
Table 5.2. Laminate stiffness in the joint-transition-region	104
Table 5.3. Density of the materials used for frequency analysis in kg/m^3	105
Table 5.4. Tip displacements of the SB Models and MB Model	107
Table 5.5. Loads generated by cable mechanisms	114
Table 5.6. Undamped natural frequencies in Hz.....	115
Table 5.7. Additional mass to the blade due to stainless cables and CFCCs	117

1. INTRODUCTION

1.1 Overview

Wind energy is a natural energy resource and is a viable alternative to satisfy the future energy needs of an increasing world population and improving economic activity. The Energy Information Administration (EIA) [1] estimates that between 2008 and 2035, global energy consumption will increase by 53%. Remarkably, energy use of the emerging non-Organization for Economic Co-operation and Development (OECD) nations is expected to grow 85% by 2035 [1].

Even though construction cost, unreliable availability of wind, bird strike, and noise have been limitations, wind energy still provides better environmental and economic benefits in comparison with the remaining energy sources [2, 3]. As an example, wind energy is capable of providing 72 TW (1 TW = 10^{12} watts) of electric power which is approximately four times the global energy consumption of 16.9 TW in 2008 [1, 4]. Also, the U.S. Department of Energy (DOE) reports that if wind energy contributed 20% of the US electricity supply, it would reduce carbon dioxide emissions from electricity generation by 25%, cumulative water use in the electric sector by 8%, and natural gas use by 11% through 2030 [2]. Due to the aftermath of the 2011 Tohoku earthquake and tsunami that resulted in severe damage to several nuclear reactors at Fukushima Daiichi Nuclear Power Plant, the Japanese government put the use of nuclear power on hold. The event may have more profound implications for the future of world nuclear power. The support of clean energy is demanded due to the possible

ramifications of Fukushima for the long-term global developments and government policies of nuclear power [5]. In fact, development of wind turbines will be a significant key factor to satisfy the prospective energy demand and to achieve a safe world.

In 2005, a unique wind power system without both blades and rotary components was proposed and developed at the Delft University of Technology. An electrostatic wind energy converter (EWICON) was utilized to directly convert wind energy into electrical energy. This was a revolutionary solution to suppress noise issues and bird strikes. Since the system could not produce massive electrical power, it was necessary to explore options to increase its power generation efficiency [6-8]. Another arrangement is the vertical-axis wind turbines (VAWT) known as Savonius and Darrieus [3]. However, the horizontal-axis wind turbine (HAWT) with propeller type blades is the dominant one in large-scale wind power systems for economic reasons. Its configuration as an upwind land-based construction is schematically depicted in Figure 1.1. A HAWT is typically composed of a foundation, tower, nacelle, hub, and two or three blades. The global (x,y,z) coordinate system as well as the blade (X,Y,Z) coordinate system originates from the center of the hub. The blades are attached to the hub at an angle to the plane of rotation (x - y plane). The hub includes the blade pitch control unit which can actively adjust this angle to mitigate the aerodynamic forces [3]. The z -axis is designated as the rotational axis of the blades, which turn in a counterclockwise direction. The foundation is designed to prevent the tower from overturning under extreme wind conditions. The tower supports the nacelle, hub, and blades. Mechanical and electrical components, such

as the gearbox, generator, brake, drive train, and control unit, are all housed in the nacelle.

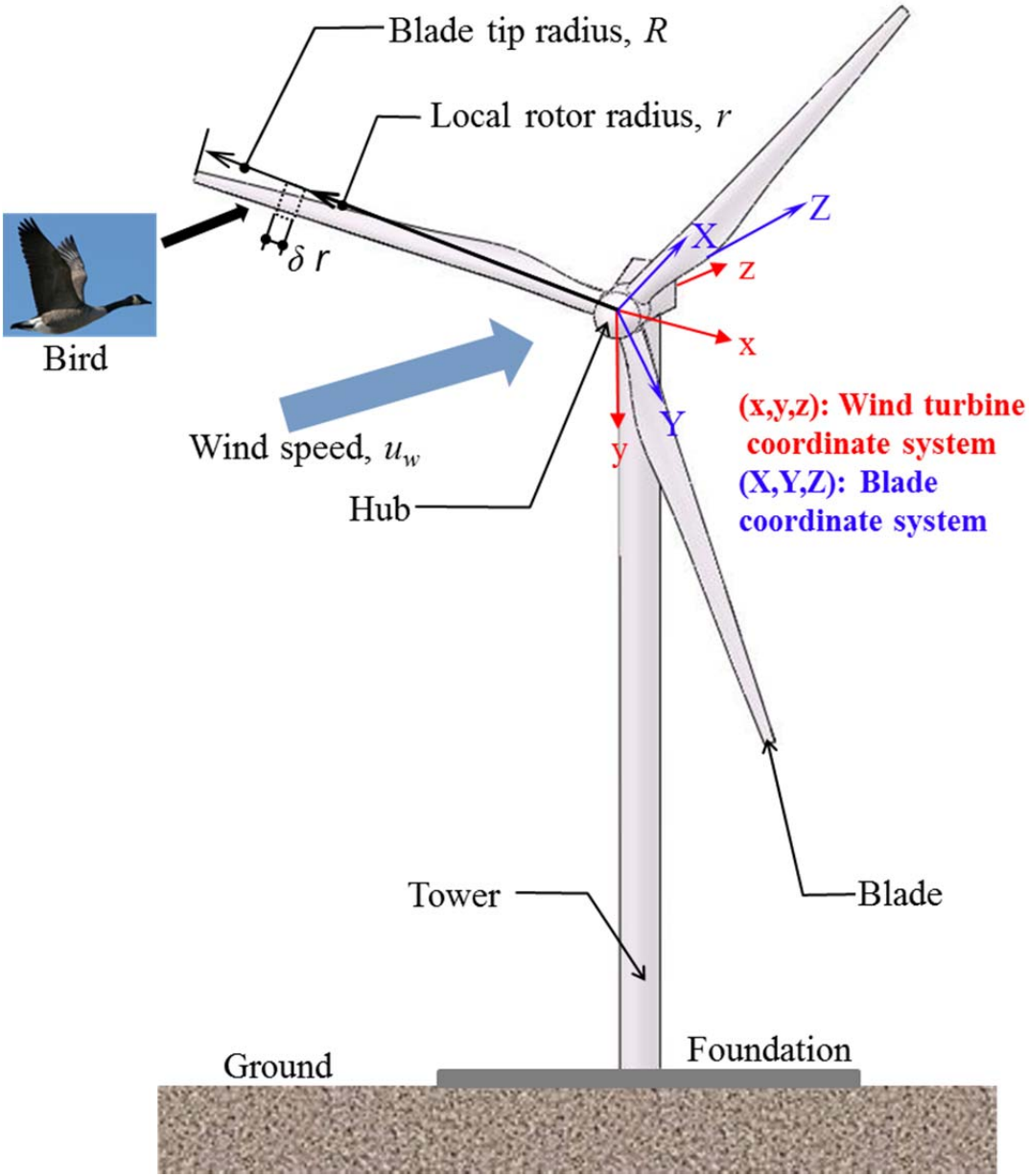


Figure 1.1. Schematic of a typical horizontal-axis wind turbine.

The size of HAWTs has grown rapidly in the last two decades, resulting in proportionally greater power output. Electrical power extracted from a wind turbine (P) is given by the well-known expression:

$$P = \frac{1}{2} \rho_{air} C_p A u_w^3 \quad (1.1)$$

where ρ_{air} is the density of air; C_p , the power coefficient of a wind turbine; A , the swept area of a wind turbine ($= \pi R^2$). The power coefficient indicates an efficiency in extracting the electrical power from the power contained in the air stream. It is obviously observed in Equation (1.1) that the electrical power is dependent on the wind speed, blade tip radius, and power coefficient. The theoretical maximum value of the power coefficient is approximately equal to 0.593, which is known as the Betz limit [9]. As stated by Eggleston *et al.* [10], practically the maximum power coefficient of HAWTs with the smooth airfoil blades is about 0.45; the power coefficient of 0.3 to 0.35 can be viewed as a good design. Since wind speed increases with elevation, an increasing wind turbine tower height enables expansion of the blade tip radius to improve energy production. Nowadays HAWTs with a blade tip radius of 50-64 m are already commercially installed, and they generate power in the range of 3.5 MW to 7.5 MW [2, 11-14]. Additionally, the first 8 MW prototype wind turbine assembled by a joint venture between Vestas and Mitsubishi Heavy Industries was successfully installed at the Danish National Test Center in January 2014 and has produced electricity [15].

As the blade length increases, the blade weight increases exponentially. In commercial blade designs, the weight scale is at an exponent of about 2.53 [2, 16-18]. Utilization of carbon fibers in the large blade enables a thinner and more efficient blade profile along with a stiffer and more slender blade, and reduced weight. This also results in increased material costs. Therefore, hybrid material systems such as carbon and glass fiber (CF/GF) reinforced composite materials are of significant attraction to the large/robust blade designs in order to improve specific stiffness/strength and damage tolerance of the blade.

In addition to the increase in the blade weight caused by the blade extension, manufacturing a large-scale wind turbine blade is a significant challenge which introduces further complications in facilities and transportation. It is very desirable to develop modular construction and successful joint designs without alterations in structural integrity and stability requirements. For example, the G128-4.5 MW blade is constructed in two sections, and they are connected together with a rigid metal joining section [12]. Additional concepts explore various connectors, receptacles, threaded fasteners, or overlapped stiffeners [19-21].

The blade has to sustain aerodynamic, inertial, gravitational, and service loads in operation. Also, the blade is exposed to various impact events such as bird strikes and hail storms where safe operation and subsequent safe shut down are of significant importance. As the local stiffness of the blade changes due to impacts, the probability of inducing dynamic instability increases. Thus, the study of damage mechanisms of the blade caused by impacts is of crucial importance as well.

1.2 Literature Review

1.2.1 Wind Turbine Blade Design

A typical wind turbine blade is composed of cylindrical and airfoil cross-sections. The cylindrical section is located near the blade root, where the blade is attached to the hub by means of metallic bolts [22]. The blade is internally reinforced to maintain the original shape of the airfoil during operation. The airfoil section belongs to the rest of the blade and determines the aerodynamic performance. The selection of appropriate cross-section profiles, taper angles, and twist angles plays an important role in sustaining aerodynamic forces. Though existing laminar airfoils, such as NACA (National Advisory Committee for Aeronautics) airfoils, were historically used for the blade designs until the 1980s, low-drag airfoils are being developed at the National Renewable Energy Laboratory (NREL) in the U.S., Delft University of Technology in Netherland, Riso National Laboratory in Denmark, etc. to specifically measure the performance of wind turbines [23-27].

Typically, the blade has upper/lower blade skins and internal stiffeners. The skin is usually of sandwich constructions to resist buckling. Either glass fiber reinforced polymers (GFRP) or carbon fiber reinforced polymers (CFRP) are utilized for the face sheets of sandwich constructions while polymeric foams, balsa wood, or honeycomb type are taken as the core materials [28]. The internal construction of the blade may take the form of a box girder, coupled double box, spar cap box, single shear web, or double shear webs [3, 28-30]. In the spar cap/shear web configuration, the spar cap is manufactured with the blade skin and then bonded to the shear web. This configuration

is located between the excess of the blade root and the vicinity of the blade tip. Since the spar cap carries flapping bending loads, its laminate is generally composed of the hybrid CF/GF reinforcement of either tape and/or fabric composites. A sandwich construction is employed for the shear web to resist a flapping shear deformation [28, 31, 32].

The chord length and blade thickness are determined based on the size of the blade tip radius. Griffin [18, 33, 34] reported non-dimensional chord length and twist angle distributions for blades with 40 m to 60 m blade tip radii. The chord length is normalized with respect to the blade tip radius. The blade thickness at the local rotor radius can be determined by the corresponding chord length multiplied by a characteristic ratio. However, this fraction for the blade thickness varies based on an airfoil selection [24, 25].

Today wind turbine blade manufacturers develop their proprietary technology design concept and manufacturing process. Due to the complex shape of the blade, various techniques such as modified filament winding, prepregs, and vacuum assisted resin transfer molding (VARTM) are adapted to manufacture the large blades. Compared with the wet lay-up approach, the latter technologies provide manufacturing advantages such as controlling and obtaining constant material properties with high specific stiffness and strength [17]. In current production, the majority of wind turbine manufacturers such as Enercon and GE Energy use VARTM which offers lower manufacturing costs as compared to prepreg technology. Nevertheless, VESTAS and GAMESA, two of the top four wind turbine manufacturers, use prepreg technology to ensure the high quality of

products [35]. Enercon, GE Energy, GAMESA, and Siemens have commercially installed wind turbines with a blade tip radius of around 60 m [11-14].

Current efforts in computational modeling of the blade are reviewed next. At the stage of blade designs, computational modeling is a powerful, economic, and time-saving approach. Computational models are utilized to understand, analyze, and predict structural behaviors of the blade. However, the modeling techniques have a certain limitation. Defects from the manufacturing process are not taken into account, and failure criteria of composites are not accurate particularly under non in-plane loading conditions [36]. Reliable computational methodologies for structural, fatigue, aeroelastic, and optimized design of composite rotor blades needs to be established to improve prediction accuracy. The proposed computational methodologies include non-linear numerical models such as failure modes, defects in materials, and complex loading conditions should be validated with experimental tests [31, 37-43].

Generally, the blade is modeled with a) shell elements with offset nodes, b) shell elements with mid-plane nodes, or c) combined shell/solid elements. In the combined shell/solid model, the solid elements are used to model sandwich cores in the skin and web. The experimental and numerical comparison of results for blade displacements and rotations points to the combined shell/solid model with the best agreement for flapping-bending and torsion cases. All computational blade models give the same results in the edgewise-bending behavior and are in good agreement with the experimental results [42, 43]. Laird *et al.* [44] used layered shell elements with mid-plane nodes in their finite element (FE) models and got more accurate solutions in torsion cases.

Griffin [18, 33, 34] selected the computational blade geometry as shown in Figure 1.2 for his analyses. The blade skin and shear web are composed of sandwich constructions utilizing triaxial glass fabric and balsa core. This triaxial fabric of 1.27 mm is employed for the face sheet with 25%, 25%, and 50% distribution of $+45^\circ$, -45° , and 0° fibers, respectively. The thicknesses of balsa cores in the forward blade skin, aft blade skin, and shear web are about 0.5%, 1%, and 1% of the chord length, respectively. The spar cap is a glass/epoxy laminate, and this stacking sequence results in the spar cap laminate with 70% unidirectional (UD) and 30% off-axis fibers by volume. The thicknesses of the spar cap are 0%, 5%, or 10% of the blade thickness. Furthermore, the constant thickness ratio of the core to the face in sandwich constructions was employed to study for the optimal design of the 60 m blade [31].

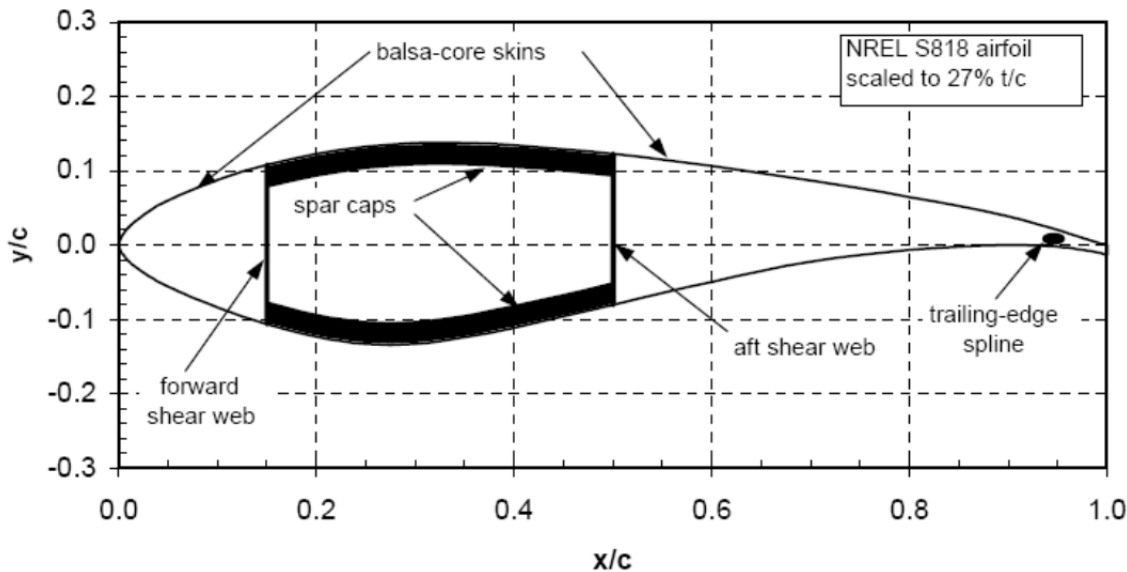


Figure 1.2. Architecture of a computational blade model [18, 33, 34].

Generally, any blade design must ensure that natural frequencies of the blades cannot be excited by rotational frequencies or harmonics of a wind turbine. There are two transverse modes (flapping and edge) and a torsional mode of the blade in natural frequencies. A Campbell diagram where natural frequencies of components (blade, tower, etc.) and relevant exciting frequencies are depicted is utilized to check if resonance phenomena occur. The exciting frequencies are defined by a rotor rotational frequency and its multiples [3, 29, 36]. The influences of four different fiber layers (S-type and E-type glass, Technora, and Kevlar) to dynamic properties of a blade were investigated, and it was demonstrated that a lower density material had higher undamped natural frequencies and larger deflections [45].

The bird impact scenario which is considered a dangerous threat to the safety in the aircraft industry is also of interest in wind turbine power plants [46-51]. Specifically, the Swedish Power Association Development Foundation [52] recommended that impact velocity and bird weight be considered as a basis for the strength and fatigue calculations where the bird strike is assumed to be in the vicinity of the blade tip at or near the leading edge (*i.e.*, $0.7 < r/R < 1.0$). The impact velocity of a bird was defined as a wind speed added to a bird's velocity of 15 m/s, and a bird mass ranged from 1 kg to 4 kg [52].

Typically bird impact tests are conducted with a high-powered gas cannon where an appropriate gelatin-body may replace the real bird according to test guidelines. These test results show appreciable scatter [53]. In order to reduce such scatter and get an in-depth description of the actual impact event, the modeling methods rely on four potential

choices: Lagrangian, Coupled Eulerian-Lagrangian (CEL), Arbitrary Lagrangian-Eulerian (ALE), and Smoothed Particle Hydrodynamics (SPH) modeling. Since a bird is mostly composed of water, the artificial bird is akin to hydrodynamic representation with a simple geometry, such as a cylinder, an ellipsoid, or a sphere [46-51, 54, 55].

A Lagrangian modeling method is the standard approach for most structural finite element analyses (FEA). The nodes of Lagrangian meshes are connected to materials of a bird and then follow the materials under motion and deformation. However, the major problem of this method is the severe mesh deformation. Large distortions of the elements may cause inaccurate results, severe hourglassing, reduced time steps, and even error termination [49, 50].

In Eulerian modeling techniques, an Eulerian mesh remains fixed in space, and materials flow through the mesh. For this reason, mesh deformations do not occur, and the explicit time step is not influenced. This method overcomes stability problems due to excessive element deformations. In typical bird impact simulations, a bird is treated as a soft body of Eulerian elements and flows in a fluid-like manner over a target structure modeled with Lagrangian elements. Thus, the CEL approach is used since the computational domain can cover the region where Eulerian materials exist at both the current and later time points. Typically, Eulerian elements are small in size to provide accurate results [49, 50].

The ALE method provides more an efficient simulation than the CEL method. While ALE and CEL methods are basically similar, the ALE method allows an Eulerian mesh to move and to deform with material flowing inside the mesh. The ALE method

contributes to saving in computational time due to reductions in the number of Eulerian elements. Its results are strongly associated with mesh dependence [49].

In the SPH method, an impactor is assumed to be fluid of free motion. This advantage is to reduce computational time significantly and to overcome severe deformations. However, this method leads to the lack of dissipation mechanisms that affect to local structure responses and hence shows unrealistic bird behavior [49, 56].

The other important aspect for bird impact simulations is the contact algorithm, which prevents penetrations and calculates reaction forces. The algorithm has to handle large deformations, splitting of a projectile, sliding of bird's materials over a target surface, and the creation of multiple contact interfaces due to possible fractures of the target structure [57]. Furthermore, Shmotin *et al.* [47] demonstrated that their best numerical results were obtained with zero friction on the contact surface in comparison with their experimental results.

1.2.2 State-of-the-Art Wind Turbine Studies

Wirz *et al.* [58] proposed an innovative biplane wind turbine blade to improve aerodynamic and structural performances. The aerodynamic performances and cross-section properties of the biplane blade were numerically obtained and were compared with the thick monoplane blade. Also, the blade model with an isotropic material and simple geometry was employed to validate their computational model and design parametric study.

Bending-torsion coupling responses of a composite wind turbine were numerically investigated to understand passive pitch-controls. Experiments were performed for validation of the numerical simulations. It was found that the highest strains appeared near the leading edge of the CF/GF hybrid composite blade due to reversed fiber angle orientations. It was suggested that one more layer with distinct fiber orientations be added to the initial laminate in the blade skin to avoid this phenomenon [30].

Buckling resistance of the blade is provided in references [28, 59-62]. Berggreen *et al.* [59-61] investigated buckling strength of glass/epoxy panels utilized in the blade. The ultimate failure loads of the panels generally decreased as imperfections of the panel increased. Local buckling and instant failure of panels arose from large and deep delaminations. The smaller delaminations closer to the surface of the panels showed stable growth. Jensen *et al.* [62] studied structural behaviors of a 34 m wind turbine blade in the elastic and plastic phase. They identified the failure modes that caused ultimate collapse. Flapping bending caused a non-linear deformation, which is called ovalization, in the box girder. The crushing pressure generated by the ovalization strongly increased the web deflection. Additionally, the rotational stiffness of the corners of the box girder was significantly important to avoid ovalization, the so-called Brazier effect, and also provided rich buckling resistance to the flange. Similarly, the rotational stiffness of the joints between the spar cap and web was crucial in the blade design. Since the flange of the box girder and the spar cap in the main spar design were usually made as monolithic composite laminates, the long blade may not have very large

stiffened monolithic shallow shell caps. The unstiffened parts are sensitive to failure in local buckling. Also, the presence of imperfection, which was produced throughout the manufacturing process, dominated the local buckling mode of failure [28].

Saravanos *et al.* [63] predicted damped natural frequencies for the glass/epoxy blade modeled with beam elements. They predicted and measured modal frequencies and modal loss factors for a 35 m wind turbine blade. A good correlation between predicted data and experimental data was achieved.

The vibration and aeroelastic analyses for an 82 m wind turbine blade were numerically conducted to estimate its power output, displacements, and natural frequencies. There was significantly different in power output between the rigid and flexible blade models; this occurred due to the effect of aeroelastic deformations [64]. Anisotropic Timoshenko beam models were developed for the aeroelastic design of the blade in order to take into account the coupling effects of anisotropic materials. Eigenvalue and static analyses were performed to validate the beam model and computational implementation. It was concluded that anisotropic characteristics should be considered to improve accuracy in numerical results [65].

The methodology for fatigue tests of the 44 m blade under the simultaneous dual-axis loading was proposed. Its fatigue responses were obtained by using the calculated two point loading conditions and a simplified beam model [39]. Furthermore, the 40 m blade was numerically analyzed under critical wind loads to assess its failure types and severities based on the Tsai-Wu failure criteria. Wind frequency and resonant mode analyses were conducted as well [66].

The performance of an adhesive joint between the blade skin and spar cap under bending and tension was investigated through FE methods. The effect of adhesive material properties and geometries, such as plasticity, fillet, and imperfections on interlaminar stresses in the adhesive layer, was examined. The strength of the joint was evaluated based on the crack initiation and propagation analysis [67].

Sandia National Laboratories (SNL) designed and evaluated a 100 m all-glass baseline wind turbine blade with its weight of 114 tons. Scaling laws were used to extrapolate existing blade model properties to the baseline blade. Strain and deflection, buckling, fatigue, and flutter analyses of the baseline blade for the design loads were performed. As a result, it was observed that it was feasible to construct a 100 m blade using conventional geometries and all-glass materials. However, the weight of the baseline blade was very high and not cost-effective for commercial purposes. The baseline blade would be targeted for weight loss, cost improvement, and development of structural and aerodynamic performances [68, 69].

1.3 Objective and Approach

The research objective is to computationally explore a design concept that consists of modular construction and successful joining while adhering to the structural integrity and stability requirements. Subsequently, the feasibility and advantages of introducing the joint concept for a modular hybrid composite wind turbine blade will be assessed with various airfoils and composite architectures for the 80 m blade. Our design and damage assessment study of the 80 m hybrid composite blade under static and dynamic conditions representative of operational and bird impact loads will further serve to design relevant scale test articles.

The research approach is briefly summarized as follows: a) the large-scale single length wind turbine blade geometry based on our initial model of the 80 m blade with sandwich skins and spar cap/shear web reinforcements is introduced as reported by Nanami [70-73]; b) further tailoring will be conducted to compensate for local high stress concentrations and to reduce the weight of the blade; c) a modular blade concept will be introduced to simplify the manufacturing - assembly processes; d) computational simulations throughout the static and dynamic operation regimes will be undertaken on commercial FE software such as ABAQUS to specifically assess displacements, stresses, strains, and vibration modes and assess damage tolerance to operational and impact loads.

2. TURBINE BLADE DESCRIPTION

An 80 m blade with traditional spar cap and shear web configuration, designed to satisfy the future energy demand, is described in this section, and this model is developed to understand static and dynamic behaviors of the blade. The 80 m blade design studies will be extended to address conceptual assembly mechanisms for multi-section configuration of the blade discussed in Chapter 5.

2.1 Blade Geometry/Constraint Description

The benchmark 8 MW class wind turbine research blade in our study has a blade tip radius of 80 m and is positioned at a 140 m hub-height. The blade geometry in Figure 2.1(a) is modeled in SolidWorks, and for simplicity, the pre-twist angle distribution is neglected in the blade model. The thick-airfoil family (NREL S817, S816, S818) is employed for its excellent aerodynamic performance as reported in [24, 25]. The corresponding cross-sections are shown in Figure 2.1(b).

The span station defined as a function of r/R describes the non-dimensional local rotor radius, *i.e.*, $r/R = 0$ indicates the hub center, and $r/R = 1$ denotes the blade tip. The non-dimensional chord (c/R) distribution along the span station is taken from Griffin [18, 33, 34]. The blade cross-section shape and ratio of the blade thickness to the chord length (t/c) along the span station are provided in Somers *et al.* [24, 25]. These non-dimensional specifications are summarized in Table 2.1, and the 80 m blade model for this study is extrapolated based on the specifications.

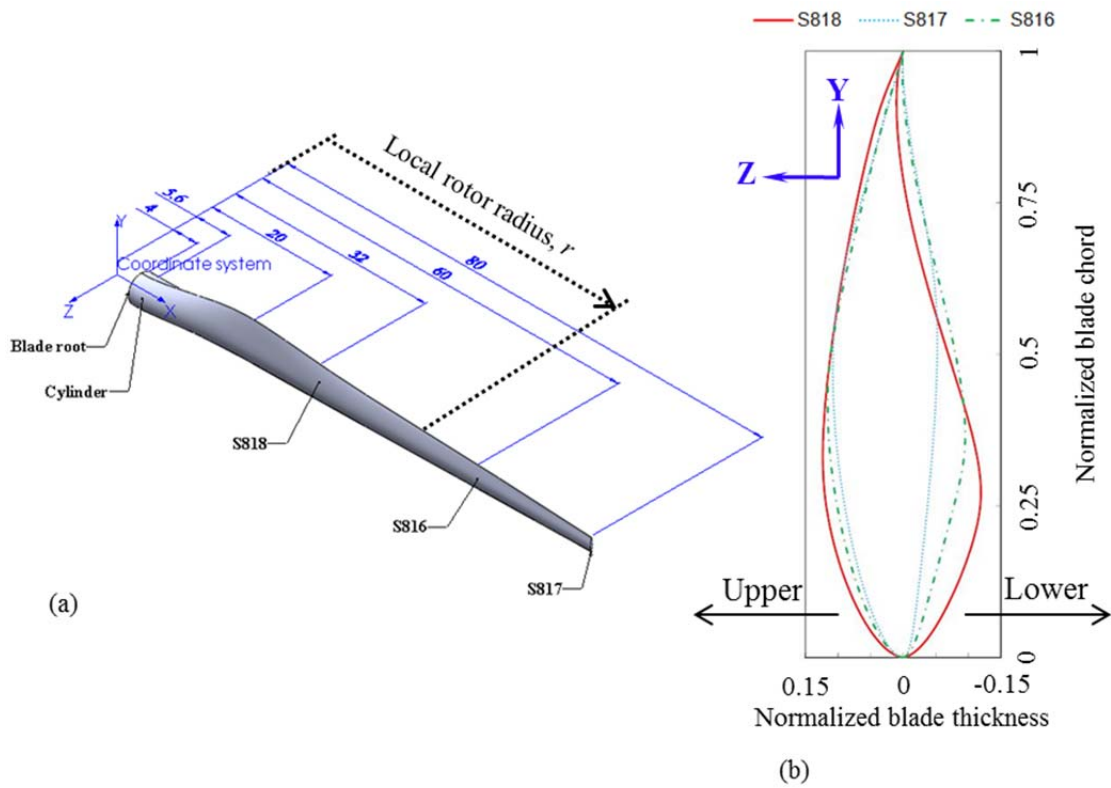


Figure 2.1. The 80 m blade: (a) dimensions of the blade, and (b) airfoil shapes.

Table 2.1. Extracted geometrical specifications

Span station, r/R	Cross-section	Chord length, c/R	Blade thickness, t/c
0.05	Cylinder	0.055	1
0.07	Cylinder	0.055	1
0.25	S818	0.08	0.24
0.4	S818	0.0692	0.24
0.75	S816	0.044	0.21
1	S817	0.026	0.16

The internal reinforcement construction is composed of spar caps and shear web, and the recommended positions for the forward and aft shear webs are placed to improve buckling stability in the blade as shown in Figure 2.2 [18, 33, 34]. Spar caps are located between the forward and aft shear webs. Dorsally the spar cap width is a constant from the blade root to 25% of the blade tip radius, and this width is linearly decreased further to the blade tip.

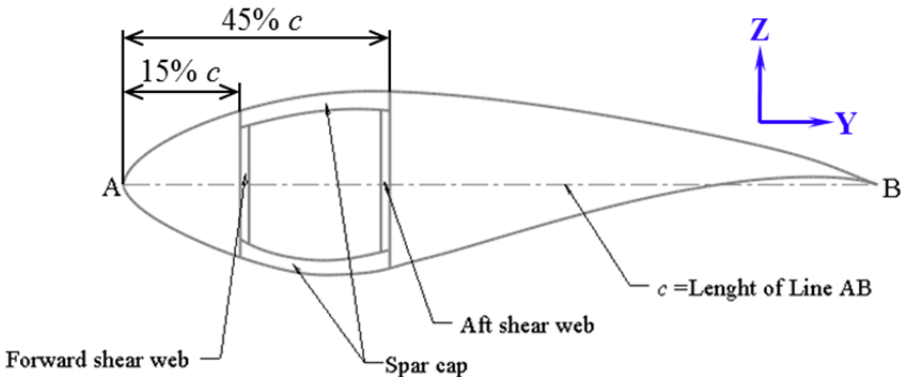


Figure 2.2. Spar cap/shear web configuration.

2.2 Material Selection/Composite Layup

Our selection of materials includes balsa wood, Divinycell H160 foam, UD-GF, GF fabric, and CF fabric. Generalized Hooke's law is adopted for all materials with reversible response. However, balsa wood and Divinycell H160 foam are treated as an elastic-perfectly plastic material that follows von Mises yield criterion. Hashin damage initiation criteria and energy-based damage evolution law are utilized to track various damage modes and mechanisms of composite materials.

Next, we describe our design for the laminate stacking sequence and corresponding layer thicknesses. The root section of the blade consists of GF fabric layers since GF fabric layers are economical and provide enough specific stiffness/strength to bond a metallic flange or bolt connection to the root section. In the airfoil section, the blade skin and shear web are treated as sandwich constructions of GF layers with either balsa wood or Divinycell foam as a core in order to avoid the occurrence of buckling. Two different core materials have similar material properties except elastic modulus and Poisson's ratio and are employed to understand the influence of the change in elastic properties of a core material to damage modes. GF fabric layers are employed for the face laminate in the skin, and the face in the webs is laminated with 0° , 45° , and -45° UD-GF layers. Hybrid GF/CF composite laminates which contain 15% CF fabric and 85% UD-GF layer reinforcement by volume are used for the spar cap. The spar cap has to provide high specific stiffness/strength and high price-performance ratio. Generally, UD fiber layers of a spar cap are used to carry bending loads while off-axis or fabric layers of a spar cap are employed to resist shear deformations. Since carbon fibers

are much expensive as compared with glass fibers, it is not feasible to use only CF layers to construct a spar cap. The hybrid CF/GF spar cap laminate is proposed based on cost, stiffness, strength, and mass. Properties of both the blade skin and spar cap laminates are assigned to the blade skin between the forward and aft shear web as shown in Figure 2.3, and these properties create the asymmetric section stiffness matrix.

The composite lay-up employed in this model is summarized in Table 2.2. Since the composite blade root is connected to the hub with large bolts, this section usually experiences high stresses. Therefore, laminates at the blade root section are much thicker than at the rest of the blade. In the root section ($4 \text{ m} < r < 5.6 \text{ m}$): 40 mm thick laminate is employed. Thickness of the core material and face sheet is as follows: In the airfoil region I ($5.6 \text{ m} < r < 46 \text{ m}$), there are 2 mm thick face sheet of composite sandwich, the core thickness assigned as 0.6% of the chord length for the forward skin (blue dash line box in Figure 2.3), and as 1% of the chord length for the aft skin (red dash line box in Figure 2.3) and shear web. In the airfoil region II ($46 \text{ m} < r < 80 \text{ m}$), there are 1 mm thick face sheet of composite sandwich, the core thickness in the forward skin, aft skin, and shear web corresponds to 0.5%, 1.1%, 0.8% of the chord length of the local airfoil, respectively. The thickness of the spar cap corresponds to 2.5% of the local maximum cross-section thickness.

The core thicknesses and laminate thickness of the spar cap are assigned as a step function. The blade is divided into eight sections. Blade thicknesses are first obtained at nine locations that form sections along the local rotor radius. Over each section of the blade, the equivalent section thickness of the core and spar cap is assigned which is

obtained by averaging the thicknesses at the two ends of the section. The core thicknesses in the skin and shear web and the laminate thickness of the spar cap are presented in Table 2.3.

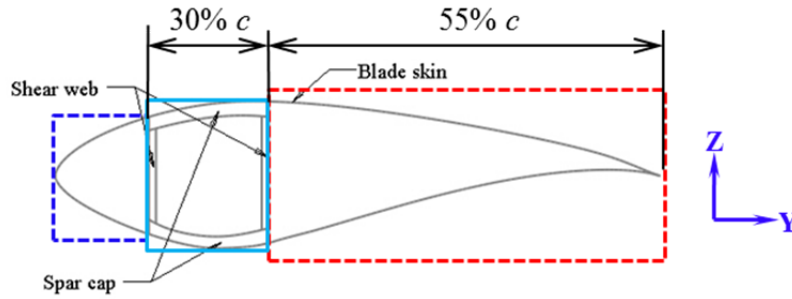


Figure 2.3. Sections of the blade skin.

Table 2.2. Lay-up used in the blade model

Layer	Blade root	Blade skin	Spar cap	Shear web
1	GF fabric	GF fabric	CF fabric	GF fabric
2	GF fabric	Core	UD-GF	45° UD-GF
3	GF fabric	GF fabric	CF fabric	-45° UD-GF
4	GF fabric	-	UD-GF	Core
5	-	-	CF fabric	-45° UD-GF
6	-	-	UD-GF	45 ° UD-GF
7	-	-	UD-GF	GF fabric
8	-	-	CF fabric	-
9	-	-	UD-GF	-
10	-	-	CF fabric	-
11	-	-	UD-GF	-
12	-	-	CF fabric	-

Table 2.3. Thickness distribution of the core material and proposed spar cap

Range of local rotor radius, r (m)	Thicknesses of core materials (m)			Spar cap (m)
	Forward blade skin	Aft blade skin	Shear web	
4-5.6	-	-	-	-
5.6-20	0.032	0.054	0.054	0.074
20-32	0.036	0.060	0.060	0.036
32-46	0.030	0.050	0.050	0.029
46-60	0.020	0.044	0.032	0.022
60-70	0.016	0.035	0.025	0.016
70-75	0.013	0.029	0.021	0.012
75-80	0.011	0.025	0.018	0.009

2.3 Design Loads

The blade is subjected to aerodynamic, gravitational, inertial, and service loads in operation. Gravity loading on the blade leads to an in-plane bending moment that sinusoidally varies along with the position of the blade. The moment due to gravity reaches the maximum value when the blade is horizontally positioned, and the acceleration of gravity (g) is 9.81 m/s. The inertial loads include centrifugal and gyroscopic loads. When the blade is rotated, a centrifugal force generates tension in the blade as expressed below.

$$F_{centrifugal} = \Omega^2 \int_r^R m(r) r dr \quad (2.1)$$

where $F_{centrifugal}$ is a centrifugal force; Ω , the angular velocity of the blade; $m(r)$, mass per unit length at r .

Since the blade is deflected in the out-of-plane direction due to aerodynamic loads, a tensile load due to a centrifugal force is slightly deviated from the rotational plane. The tensile load acts on the blade to push back the blade on the rotational plane. This phenomenon is known as a centrifugal relief. Additionally, gyroscopic loads on the blades occur when a wind turbine yaws in operation. The service loads that result from control systems of a wind turbine such as braking and blade-pitch control act on the root section of the blade [3].

2.3.1 Aerodynamic Loads

Mostly aerodynamic loads such as lift and drag forces contribute to the deformation of the blade. Lift and drag forces of an infinitesimal blade element are calculated using two-dimensional airfoil characteristics, disregarding the velocity along the rotor radius and three-dimensional effects. When the X-axis of the blade is aligned with the x-axis of the wind turbine (Figure 1.1), lift ($\delta\mathbf{L}$) and drag ($\delta\mathbf{D}$) forces for the rotating blade with an angle of attack (α) are generated. The contribution of lift forces along the y-axis enables the blade to rotate while the decomposed component of drag forces along the y-axis acts on the blade to resist its rotation. Resultant relative wind velocity (V_{rel}) for the rotating blade is represented by Equation (2.2) where u_{ta} is a tangential air flow velocity acting in the direction opposed to the tangential velocity of the blade (u_{tb}) [3]. Note that the wind speed (u_w) is aligned to the z-axis of the wind turbine.

$$V_{rel} = \sqrt{u_w^2 + u_{ta}^2} \quad (2.2)$$

Lift forces normal to a resultant relative wind velocity and drag forces parallel to a resultant relative wind velocity are given by

$$\delta L/c\delta r = \rho_{air} V_{rel}^2 C_l / 2 \quad \text{and} \quad \delta D/c\delta r = \rho_{air} V_{rel}^2 C_d / 2 \quad (2.3)$$

Here, δr is the infinitesimal blade length; ρ_{air} , an air density; C_l , a lift coefficient; C_d , a drag coefficient [3]. Air density is selected to reflect the tower height. Lift and drag coefficient corresponding to the limit angle of attack (α_l) is selected to have the upper limit of C_l in a low-drag lift coefficient range [24]. The tangential velocity of the blade is linear speed of the rotating blade with a constant angular velocity (Ω) which varies along the rotor radius. The ratio (λ) of tangential velocity of the blade to wind speed at r is presented in Equation (2.4a). At the blade tip (*i.e.*, $r = R$), Equation (2.4a) can be rewritten in Equation (2.4b), called a tip speed ratio (TSR) [3, 29].

$$\lambda = u_{tb}/u_w = r\Omega/u_w \quad (2.4a)$$

$$\text{TSR} = R\Omega/u_w \quad (2.4b)$$

Herein, the TSR is assumed to be a constant value, and the speed ratio linearly increases along the rotor radius. For a given wind speed and TSR value, the angular velocity of the blade can be determined from Equation (2.4b). The tangential velocity of the blade along the rotor radius can be obtained from Equation (2.4a). Finally, the resultant of each decomposed load component along the blade Y- and Z-axis become, respectively:

$$dP_Z = (\delta L/c\delta r)\cos\alpha_l + (\delta D/c\delta r)\sin\alpha_l \quad (2.5a)$$

and

$$dP_Y = -(\delta L/c\delta r)\sin\alpha_l + (\delta D/c\delta r)\cos\alpha_l \quad (2.5b)$$

2.3.2 Impact Loads

In addition to the above-mentioned loads, the blade is also exposed to various impact scenarios such as hail damage and bird strike where safe operation and subsequent safe shut down are of significant importance. Bird strikes at wind turbines bring out issues associated with power shut down and habitat loss. Annually 20,000 bird strike incidences to wind turbines (*i.e.*, 4.27 deaths per turbine per year) occur in the US while 9730 bird strikes to civil aircrafts were reported in 2011 [74-77].

3. COMPUTATIONAL SIMULATION

3.1 Element/Mesh Selection

The blade is represented with Lagrangian S3R/S4R linear shell elements of Abaqus, commercial FE software, and its FE model is created on HyperMesh. The fine and coarse mesh sizes (0.02 m/0.15 m) are employed in the blade model. In impact studies, for CEL analyses, EC3D8R Eulerian elements are assigned in the impact domain containing a bird whereas for Lagrangian impact analysis, Lagrangian C3D8R/C3D6 solid elements are utilized to represent an impactor.

3.1.1 Lagrangian Shell Elements

Lagrangian elements are defined as elements whose shape functions are generated with Lagrange polynomials [78]. Abaqus involves an extensive Lagrangian element library such as solid, shell, and beam elements to provide powerful solution tools for many different problems [79]. Conventional shell elements under the general-purpose shell element category are adopted for this study.

General-purpose conventional shell elements are valid choices both for thick and thin shell structures. Thin shells as described by classical (Kirchhoff) shell theory assume that transverse shear deformations are small enough to be negligible. On the other hand, thick shells are usually described by shear flexible (Mindlin) shell theory (APPENDIX A), and the transverse shear deformations are appreciable and affect the solution significantly [80]. Since an additional kinematic constraint is involved in the

Mindlin shell theory, this theory is easily applicable for both thick and thin shell problems.

Shell thicknesses in the blade models are significantly smaller than other global in-plane dimensions. Global in-plane dimensions are identified as the blade tip radius, the chord length, the blade thickness, or the radius of curvature. Conventional shell elements discretize a reference surface by defining the element's planar dimensions, its normal surface, and its original curvature. Although the nodes of the shell element do not exist through the shell thickness, this thickness is defined through section properties, and the stresses through the shell thickness are assumed to be negligible. The elements based on shear flexible shell theory are suitable to model sandwich constructions since typical sandwich composite constructions have very low transverse shear stiffness [79].

The validity of using shell theory can be checked with a slenderness ratio definition. For linear elastic materials, the slenderness ratio is defined as

$$\frac{K_{\alpha\alpha} l^2}{D_{(\alpha+3)(\alpha+3)}} \quad (3.1)$$

where $K_{\alpha\alpha}$ denotes transverse stiffness matrix, $D_{(\alpha+3)(\alpha+3)}$ a section stiffness matrix, $\alpha = 1$ or 2 (no sum on α), and l is a characteristic length on the surface of the shell structures. Note that the characteristic length is independent of the element's characteristic length. The ratio can be used as a guideline to determine whether the assumption that plane sections must remain plane has been satisfied. If the ratio is greater than 100, classical shell theory is generally adequate. However, the elements

described by classical shell theory will probably not give sufficiently accurate results if the ratio has smaller values than 100. The $K_{\alpha\alpha}$ and $D_{(\alpha+3)(\alpha+3)}$ can be given through a data check analysis [79].

Consequently, the blades of various geometric and material specifications are represented with three-dimensional linear shell elements (S3R and S4R) of Abaqus. S3R is a 3-node, trilateral, stress/displacement, shell element. S4R is a 4-node, quadrilateral, stress/displacement, shell element. These elements are valid for both thin and thick shell problems and suitable for nonlinear geometrical analyses. They have three displacement and three rotational degrees of freedom (DOF), allow finite strain, arbitrarily large rotation, and transverse shear, and use reduced integration to form their element stiffness; their mass and force matrixes are integrated exactly [79].

3.1.2 Lagrangian Solid Elements

Though Lagrangian solid elements are more sensitive to distortion when compared with Eulerian elements, they are routinely used to define an impactor in simulations. An impactor such as a bird in this study is modeled with three-dimensional solid elements (C3D8R and C3D6) of Abaqus. C3D8R is an 8-node linear brick element, reduced integration with hourglass control, and C3D6 is a 6-node linear triangular prism element, reduced integration with hourglass control. These solid elements have three displacement DOFs. [79].

3.1.3 Eulerian Elements

Eulerian elements represent stationary rectangular grids and allow materials to flow through the elements and to interact with Lagrangian element structures. Eulerian elements overcome numerical difficulties associated with excessive element distortion since materials are assigned to them by means of an Eulerian volume fraction (EVF). EVF represents the ratio by which each Eulerian element is filled. The volume fraction of 0 indicates that the elements are not filled at all (*i.e.*, they constitute a void); on the contrary, the volume fraction of 1 states that the elements are completely filled with materials. Accordingly, the element geometry is not conformed to the boundary of Eulerian materials at any time during an analysis [81, 82]. Three-dimensional Eulerian elements (EC3D8R) of Abaqus/Explicit are adopted for the present study. EC3D8R is an 8-node linear brick which accommodates multi-material definition and reduced integration with hourglass control [79]. Note that the nodes of Eulerian elements are independent of Lagrangian elements.

3.2 Loading and Boundary Conditions

3.2.1 Boundary Conditions

The three rotations and three displacements are constrained at the blade root as shown in Figure 3.1.

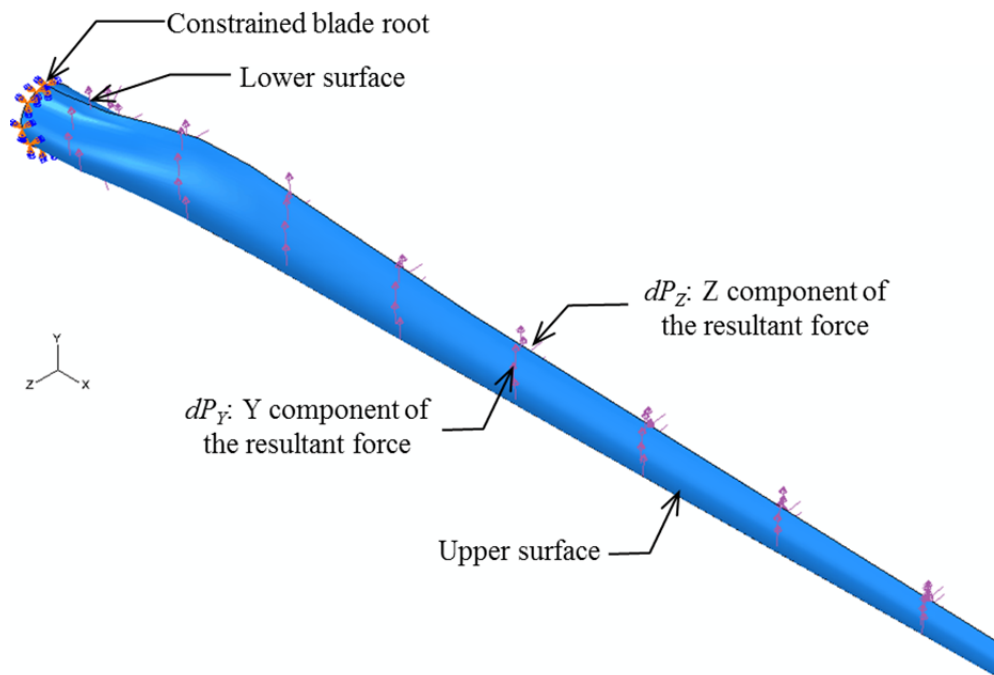


Figure 3.1. Boundary conditions for static analyses in the blade models.

3.2.2 Static Analyses

3.2.2.1 Lift and drag loads

The blade is subjected to aerodynamic, gravitational, inertial, and service loads in operation. Since mostly aerodynamic loads such as lift and drag forces contribute to the

deformation of the blade, they are selected as loading conditions for the static analyses as well as preloads in the impact simulations. The Z component of forces resulting from lift and drag forces (dP_z) is applied to the lower surface of the blade, and the Y component of the resultant forces (dP_y) is applied both to the lower and upper surfaces (Figure 3.1).

Air density is assigned as 1.208 kg/m^3 for 140 m tower (hub) height. The TSR of the blade is assumed to be constant at 7 [29]. The maximum lift and drag forces associated with $u_w = 12 \text{ m/s}$ are considered. Resultant relative wind speed along the local rotor radius can be found to calculate lift and drag forces. Lift and drag coefficients associated with the limit angle of attack (α_l) are selected to have the upper limit of C_l in a low-drag lift coefficient range [24]. Since tangential velocity of the blade is not constant along the rotor radius, lift and drag forces are evaluated at nine locations (Nodes), creating eight sections. Afterwards, lift and drag forces are decomposed into the Y - and Z -axis components, dP_y and dP_z , that are calculated in Equation (2.5) and presented in Table 3.1. In each section, the corresponding nodal forces are averaged to obtain the resultant forces that are distributed as step functions. Note that values of dP_y in Table 3.1 are one-half of dP_y values calculated in Equation (2.5b) since the dP_y is applied to two surfaces of the blade.

Table 3.1. Loads at nine nodes along the rotor radius

Node No.	r (m)	V_{rel} (m/s)	α_t (°)	C_l	C_d	dP_Y (Pa)	dP_Z (Pa)
1	4	12.7	6.5	0	0.3	14.6	3.32
2	5.6	13.4	6.5	0	0.3	16.1	3.66
3	20	24.2	6.5	1.2	0.012	-21.9	422
4	32	35.7	6.5	1.2	0.012	-47.6	918
5	46	49.8	7	1	0.008	-85.2	1,486
6	60	64.1	7	1	0.008	-142	2,468
7	70	74.5	5	0.9	0.007	-120	3,006
8	75	79.7	5	0.9	0.007	-137	3,439
9	80	84.9	5	0.9	0.007	-155	3,902

3.2.2.2 Flexural rigidity

Simple cantilever beam representation of the blade is used to estimate its flexural rigidity (EI) as shown in Equation (3.2) in conjunction with computational simulations. The primary assumptions in bending theory of a cantilever are that the traverse plane sections remain plane and normal to the longitudinal axis before and after bending [83]. Radius of curvature (R_c) is defined as a function of the blade length and out-of-plane displacement as shown in Equation (3.3). Substituting Equation (3.3) into Equation (3.2) and using $\theta_w = dw/dX$ obtains the beam flexural rigidity as presented in Equation (3.4).

$$\frac{1}{R_c} = \frac{M_b}{EI} \quad (3.2)$$

where E is the Young's modulus; I , the 2nd moment of inertia; M_b , the bending moment.

$$\frac{1}{R_c} = \frac{\frac{d^2 w}{d X^2}}{\left[1 + \left(\frac{d w}{d X}\right)^2\right]^{3/2}} \quad (3.3)$$

where w is the out-of-plane displacement; X , the axial distance.

$$EI = \frac{M_b(X)}{d\theta_w/dX} \left[1 + \theta_w^2\right]^{3/2} \quad (3.4)$$

3.2.3 Frequency Analyses

The natural frequencies and corresponding mode shapes are obtained for undamped and non-rotational blades. Linear perturbation scheme and Lanczos method are utilized to extend the eigenvalues.

It is very difficult to study the dynamic response of the blade since its aerodynamic environment is so complex and unsteady. It is useful to analyze the structural dynamics of wind turbines with discrete blade models representing a uniform hinged-beam. The hinge spring stiffness of the blade is estimated by treating the blade as an equivalent uniform-hinged beam [10]. The relationship between the hinge spring stiffness (K_s) and mass moment of inertia (I_b) is simply expressed in Equation (3.5).

$$K_s = I_b \omega_{NR}^2 \quad (3.5)$$

where ω_{NR} is the non-rotating natural frequency.

3.2.4 Impact Analyses

In all CEL impact problems, the 2kg-bird, which is commonly utilized in both bird strike experiments and simulations, is considered as a soft body impactor [46-51, 53]. The bird is represented inside an Eulerian meshed domain with a combination of fully and partially filled elements surrounded by void regions. The mass of the bird is expressed as below.

$$M_{bird} = \sum_{i=1}^n \rho EVF^{i-th} EV^{i-th} \quad (3.6)$$

where ρ is a density of a bird material, EVF^{i-th} , an element volume fraction on the i-th element; EV^{i-th} , an element volume on the i-th element.

Contact algorithms which handle calculation of reaction forces, penetration of a target structure, splitting of a projectile, sliding of materials over a target surface, and the creation of multiple contact interfaces are of important in impact simulations. A general contact algorithm, which automatically detects which surfaces and edges come into contact, with a penalty method and frictionless surface is employed in the bird impact analyses [47, 57].

3.3 Constitutive Properties

3.3.1 Mechanical Behavior of Materials

Materials with reversible behavior are described by generalized Hooke's law. Hashin damage initiation criteria and energy-based damage evolution law are utilized to track various damage modes and mechanisms of composite materials while von Mises yield criteria is selected for isotropic materials.

3.3.1.1 Progressive damage in composites

Many local failures such as fiber fracture and matrix cracking are exhibited in composite laminates prior to their final failures. The first local failure is referred to as damage initiation. Damage progression is described as the presence of additional local failures until the final failure. Therefore, Hashin's damage initiation criteria and energy-based damage evolution law are employed for fiber-reinforced composites, which follow linearly elastic behavior before the damage initiation occurs.

Hashin damage initiation criteria for the composites identify four different damage modes: fiber tension, fiber compression, matrix tension, and matrix compression as presented in APPENDIX B [84, 85]. In-plane stress components with respect to the local material coordinate system are used in the initiation criteria. Damage initiation is detected when the initiation criteria reaches the value of 1.

The post-damage initiation behavior is represented by progressive degradation of material stiffness. A characteristic length of an element (L^c) is introduced in equations for equivalent displacement (δ_{eq}) and stress (σ_{eq}) due to relaxation of element size

dependence during material softening. The equivalent displacements and stresses as defined in APPENDIX C are derived from nominal strains, nominal stresses, and the characteristic length. The constitutive law is described as the relationship between equivalent displacement and stress as depicted in Figure 3.2 [79].

The effective stress tensor is obtained from the nominal stress tensor and damage operator tensor which embodies three internal damage variables (d_f , d_m , d_s) to portray fiber, matrix, and shear damage. The damage variable activated in damage progression may vary to satisfy the equivalent stress-equivalent displacement relationship. After damage initiation occurs (*i.e.*, $\delta_{eq} \geq \delta_{eq}^0$), the damage variable for a particular mode (d) is given in Equation (3.7) and is graphically presented in Figure 3.3 [79].

$$d = \frac{\delta_{eq}^f (\delta_{eq} - \delta_{eq}^0)}{\delta_{eq} (\delta_{eq}^f - \delta_{eq}^0)} \quad (3.7)$$

where δ_{eq}^0 denotes the initial equivalent displacement where the initiation criteria is met; δ_{eq}^f , the equivalent displacement where a material is completely failure. The value of δ_{eq}^0 for each damage mode is dependent on the elastic property and strength of a material, and this value corresponds to the magnitude of stresses determined by the initiation criteria.

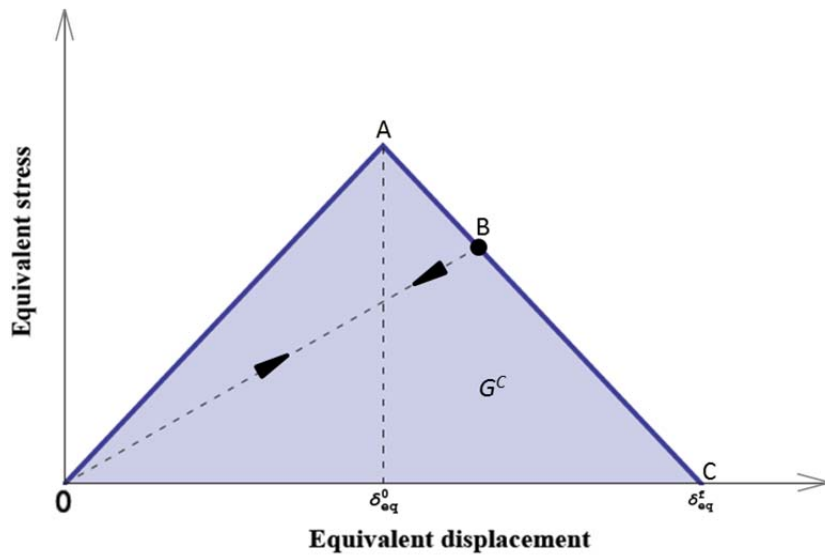


Figure 3.2. Linear damage progression based on the equivalent stress-equivalent displacement relationship.

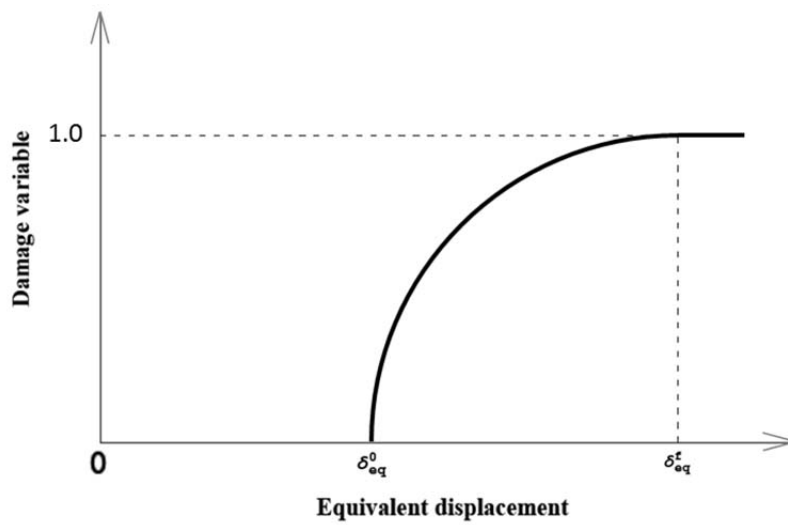


Figure 3.3. Progressive damage variable as a function of an equivalent displacement.

For the post-damage initiation behavior, the energy dissipation due to failure (G^C) is taken as the metric and calculated as expressed in the following equation [86]:

$$G^C = \varepsilon_{eq}^f \sigma_{eq}^0 L^c / 2 \quad (3.8)$$

where σ_{eq}^0 is the initial equivalent stress where the initiation criteria are met. The characteristic length of an element is simply computed as the square root of the area associated with the element. The energy dissipation corresponds to the area of the triangle OAC in Figure 3.2, and the value of the energy dissipation varies along an element size. For instance, Point B in Figure 3.2 indicates a partially damaged state, and unloading from this state travels along a linear path toward the origin in the plot of equivalent stress vs. equivalent displacement. On the other hand, the same path is followed back to Point B during reloading. Therefore, the response of a material is computed from Equation (3.9), and it is used to monitor the stiffness degradation of the composite layer enabling progressive damage tracking [79].

$$\{\sigma\} = [C_d] \{\varepsilon\} \quad (3.9)$$

where $[C_d]$ is the damaged stiffness matrix, which is expressed as follows:

$$[C_d] = \frac{1}{D} \begin{bmatrix} (1-d_f)E_1 & (1-d_f)(1-d_m)v_{21}E_1 & 0 \\ (1-d_f)(1-d_m)v_{12}E_2 & (1-d_m)E_2 & 0 \\ 0 & 0 & (1-d_s)GD \end{bmatrix} \quad (3.10)$$

$$D = 1 - (1-d_f)(1-d_m)v_{12}v_{21} \quad (3.11)$$

In the equations above, E_1 is the Young's modulus in the fiber direction; E_2 , the Young's modulus in the direction normal to the fiber direction; G , the shear modulus; ν_{12} , ν_{21} , Poisson's ratios.

3.3.1.2 Shear failure in isotropic materials

The shear failure is described with a simple failure criterion that is suitable for dynamic problems and is based on von Mises stress and equivalent plastic strain [79].

The von Mises stress for in-plane problems is expressed below.

$$\sigma_y = \sqrt{\hat{\sigma}_{11}^2 + \hat{\sigma}_{22}^2 - \hat{\sigma}_{11}\hat{\sigma}_{22} + 3\hat{\tau}_{12}^2} \quad (3.12)$$

where σ_y denotes von Mises stress and $\hat{\sigma}_{11}$, $\hat{\sigma}_{22}$, $\hat{\tau}_{12}$ the components of the in-plane effective stress tensor. The accumulated equivalent plastic strain is expressed below.

$$\bar{\varepsilon}^{pl} = \bar{\varepsilon}_0^{pl} + \int_0^t \sqrt{\frac{2}{3} \dot{\varepsilon}^{pl} : \dot{\varepsilon}^{pl}} dt \quad (3.13)$$

where $\bar{\varepsilon}_0^{pl}$ is the initial value of the equivalent plastic strain; $\dot{\varepsilon}^{pl}$, the equivalent plastic strain rate.

Material yielding starts when von Mises stress reaches the allowable strength of isotropic materials. Then, it is assumed that failure occurs when the equivalent plastic strain corresponds to the failure strain of isotropic materials.

3.3.1.3 Elastic properties and allowables

The materials used in the blade are balsa wood, Divinycell H160 foam core, UD-GF, GF fabric, and CF fabric. The balsa wood which follows elastic-perfectly plastic behavior in the simulations has the Young's modulus (E) of 4.1 GPa, Poisson's ratio (ν) of 0.3, yield strength (X_T) of 5.4 MPa, failure strain (ε^f) of 0.8, and density (ρ_m) of 155 kg/m³ [31, 87]. Divinycell H160 foam core has $E = 0.205$ GPa, $\nu = 0.404$, $X_T = 5.4$ MPa, $\varepsilon^f = 0.28$, and $\rho_m = 160$ kg/m³ [88]. The homogenized elastic properties of the composite materials are presented in Table 3.2, and their allowable strength and ultimate strain used to calculate energy dissipation of the composites are presented in Table 3.3 [89-91]. From Equation (3.8), the energy dissipation is obtained as a factor of the characteristic length and is presented in Table 3.3. Four damage modes (fiber tension, fiber compression, matrix tension, and matrix compression) are written as a subscript to the right of energy dissipation (G^c) in Table 3.3. While von Mises yield criterion is utilized for the balsa wood and foam core, Hashin damage model is utilized for the composite materials.

Table 3.2. Linear elastic properties of composite materials

	UD-GF	GF fabric [0/90] _s	CF fabric [0/90] _s
ρ_m (kg/m ³)	2,100	2,100	1,600
E_1 (GPa)	46	21	47
E_2 (GPa)	13	21	47
E_3 (GPa)	13	8.55	10
G_{12} (GPa)	5	3.7	3.78
G_{13} (GPa)	5	3.5	3.5
G_{23} (GPa)	4.6	3.5	3.5
ν_{12}	0.3	0.183	0.33
ν_{13}	0.3	0.0305	0.33
ν_{23}	0.42	0.075	0.07

Table 3.3. Allowable strength, strain, and energy dissipation ratio

	UD-GF	GF fabric [0/90] _s	CF fabric [0/90] _s
X_T/X_C (MPa)	1,080/620	367/549	627/572
Y_T/Y_C (MPa)	39/128	367/549	627/572
S_L/S_T (MPa)	89/64	97.1/274.5	80/286
$\epsilon_{1t}^f / \epsilon_{1c}^f$ (%)	2.8/0.5	2.5/2.5	1.5/1.5
$\epsilon_{2t}^f / \epsilon_{2c}^f$ (%)	2.8/0.5	2.5/2.5	1.5/1.5
G_{ft}^C / G_{fc}^C ($\times 10^6$ N/m)	(15.1/1.55) $\times L^c$	(4.59/6.86) $\times L^c$	(4.70/4.29) $\times L^c$
G_{mt}^C / G_{mc}^C ($\times 10^6$ N/m)	(0.546/0.320) $\times L^c$	(4.59/6.86) $\times L^c$	(4.70/4.29) $\times L^c$

3.3.2 Soft Body Impact Representation

3.3.2.1 Constitutive model

An equation of state (EOS) material model is adopted as an approximation for the constitutive model of a bird (soft body impactor). In this linear model, pressure (p) is

obtained from Equation (3.14) which represents the coupling of pressure and internal energy [79].

$$p = \frac{\rho_0 c_0^2 \eta}{(1-s\eta)^2} \left(1 - \frac{\Gamma_0 \eta}{2} \right) + \Gamma_0 \rho_0 E_m \quad (3.14)$$

where ρ_0 is the reference density; c_0 , the bulk speed of sound; $\eta=1-\rho_0/\rho$, the nominal volumetric compressive strain; ρ , the current density; s and Γ_0 , material constants; E_m , the specific energy. Note that $\rho_0 c_0^2$ is equivalent to the elastic bulk modulus at small nominal strains. The linear relationship between the shock velocity (U_s) and the particle velocity (U_p) is defined through s as expressed in Equation (3.15).

$$U_s = c_0 + sU_p \quad (3.15)$$

The total duration (t_d) of an impact event is estimated in Equation (3.16) where L refers to the length of an impactor [49].

$$t_d = L/U_0 \quad (3.16)$$

Since the EOS model describes only the hydrostatic behavior of an impactor, a deviatoric behavior uncoupled with volumetric response can be defined to take into account shear strength of an impactor. The deviatoric stress tensor (\mathbf{S}) for the Newtonian

viscous shear behavior is expressed in Equation (3.17) where η_v denotes the viscosity; $\dot{\mathbf{e}}$, the deviatoric part of a strain rate tensor [79].

$$\mathbf{S} = 2\eta_v \dot{\mathbf{e}} \quad (3.17)$$

3.3.2.2 Representative bird geometry/material

Since the irregular shape of a bird poses difficulties in impact problems, a cylinder composed of gelatin with hemispherical ends is selected for its representation [47, 49, 50, 55]. The aspect ratio of 2, defined as the length (0.238m) of the cylinder to its diameter (0.119m), is adopted to provide a realistic impact pressure profile [48, 54]. The density of gelatin (ρ_{gel}) is 911 kg/m³, resulting in a bird mass of 2.0 kg approximately. The properties of gelatin used in the simulations are as follows: $c_0 = 1.4829 \times 10^3$ m/s, $s = 2.0367$, $\Gamma_0 = 0$, $\eta_v = 4 \times 10^{-3}$ Ns/m² [55].

3.3.2.3 Bird model validation

There are many reports that have addressed the validation of an Eulerian bird impactor model by using experimental bird strike test data on instrumented plates and comparing the pressure-time history with the numerical results [46, 49-51, 92]. One of the validation examples is presented in Figure 3.4 where the pressure history caused by the Eulerian impactor was in good agreement with the experimental data [50]. Since accessible experimental bird impact test data was mostly generated in the late 1970's, the initial peak pressure of experimental data was limited due to the quality of the

equipment at that time. While most of experimental bird impact tests treat high velocity impact problems (higher than 100 m/s), the Eulerian bird impactor with the velocity of 64.4 m/s was validated [92].

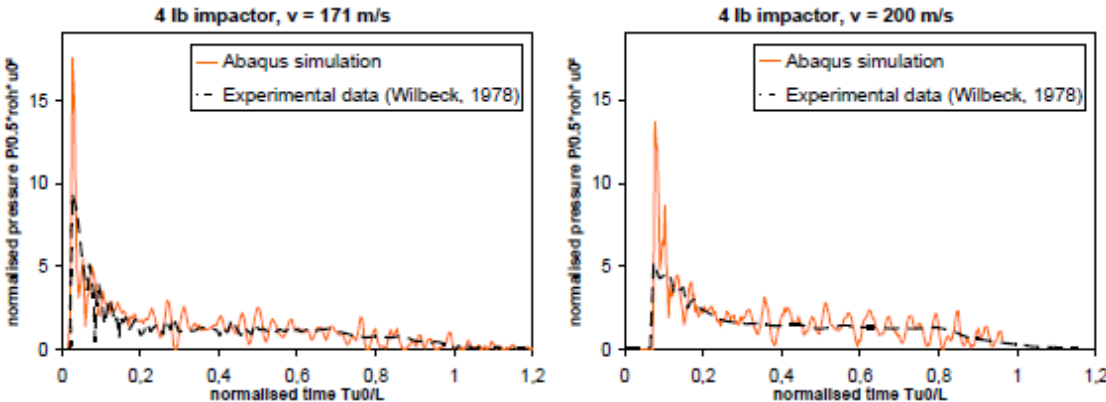


Figure 3.4. Eulerian bird impactor validation using impact test data on instrumented plates [50].

4. THE SINGLE BLADE ASSESSMENT

This chapter describes the details of computational models and results to assess structural performances of the single-continuous blade. The 80 m long blade is reinforced by hybrid CF/GF spar cap, and sandwich-structured shear web and skin. The general and computational descriptions of the 80 m blade are presented in Chapters 2 and 3, respectively.

As noted earlier, the blade is represented with Lagrangian S3R/S4R linear shell elements that follow the mid-plane shell formulation to take into account the influence of its torsional response [42-44]. The blade geometry is created in HyperMesh and is analyzed in Abaqus/Standard, herein referred as Case Study I. For Case Study I, the blade root is fully constrained, and the blade is subjected to the surface forces (dP_Z and dP_Y) resulting from lift and drag forces, which are considered as operational loads. Gravitational loads are excluded from the operational loads due to the blade analysis under gravitational loads (APPENDIX D). The mesh size of 0.15 m is employed generating 41,368 elements.

The bird impact problems are studied in Abaqus/Explicit, to be referred as Case Study II. In this case study, various impact models are considered to distinguish potential damage modes in the blade and to understand the influence of preloading, boundary conditions, and target structure sizes to the structural response of the blade. In all impact models, the 2kg-bird is considered as either a soft or deformable body, and the impact location is at $r = 77.5$ m, in the vicinity of the blade tip. The blade with balsa core is

considered as a target structure. The mesh sizes for Lagrangian and Eulerian elements are determined based on the convergence study for the optimal ratio of Lagrangian to Eulerian elements (APPENDIX E).

The 80 m blade model with the combined coarse and fine meshes is created in HyperMesh. The fine mesh size of 0.02 m is employed in the 5 m tip-sectional blade while the coarse mesh size of 0.15 m is assigned for the rest of the blade ($4 \text{ m} < r < 75 \text{ m}$). This leads to disengaged nodes at $r = 75 \text{ m}$. To overcome this disparity in the blade model, the coarse mesh region is tied to the fine mesh region at $r = 75 \text{ m}$ with the *TIE control. A total of 104,585 Lagrangian elements are generated for the blade model. Conversely, the Eulerian mesh size of 0.01 m is selected for a domain that contains a bird, and this leads to 1,200,000 Eulerian elements to define the domain.

4.1 Case Study Description

4.1.1 Core Material Comparison for Case Study I

The 80 m long blade is reinforced with hybrid CF/GF spar cap laminate, and sandwich-structured shear web and skin. Sandwich constructions consisting GF face and balsa wood core are employed in the skin and shear web of the original blade model (SW-45). In the subsequent efforts, the blade model is developed to assess changes introduced by replacing balsa wood (stiff material) cores with Divinycell H160 foam (soft material) cores. For static analyses, the blade root in both the models is fully constrained, and the surface forces (dP_Y and dP_Z), as described in Section 3.2.2, are applied along the Y-axis and Z-axis. For the purpose of comparison, the rest of all

geometry, material, and load details are maintained between the blade models with balsa wood and H160 foam cores. The total mass and moment of inertia about the blade X-, Y-, and Z-axis are presented in Table 4.1, and no significant change in inertial properties of the blade is confirmed.

Table 4.1. Inertial properties of the blade models

	SW-45	
	Balsa core	Foam core
Blade mass (tons)	45.8	46.0
Moment of inertia for torsion, I_{xx} (kgm ²)	1.61×10^5	1.61×10^5
Moment of inertia for edge, I_{yy} (kgm ²)	3.06×10^7	3.07×10^7
Moment of inertia for flapping, I_{zz} (kgm ²)	3.06×10^7	3.08×10^7

4.1.2 Direct/Oblique Impact for Case Study II

Direct and oblique impact scenarios are considered at impact location $r = 77.5$ m as seen in Figure 4.1. The Lagrangian target structure for the direct and oblique impacts is the 5 m tip section of the 80m blade ($75 \text{ m} < r < 80 \text{ m}$) while the 2kg gelatin bird is considered as a soft body impactor.

For the event of the direct impact, the 2kg-bird is assumed to have a translational velocity of 81.4 m/s, and the impact point is the leading edge. This initial velocity is prescribed along the Y-axis in the Eulerian domain and is representative of the rated velocity of the rotating blade at the impact point.

For the oblique impact, the bird is initially located at $r = 77.5$ m at an impact angle of 30° to the lower forward blade skin. The initial velocity along the Y- and Z-axis is assigned as 70.5 m/s and 40.7 m/s, respectively, leading to 81.4 m/s of resultant velocity.

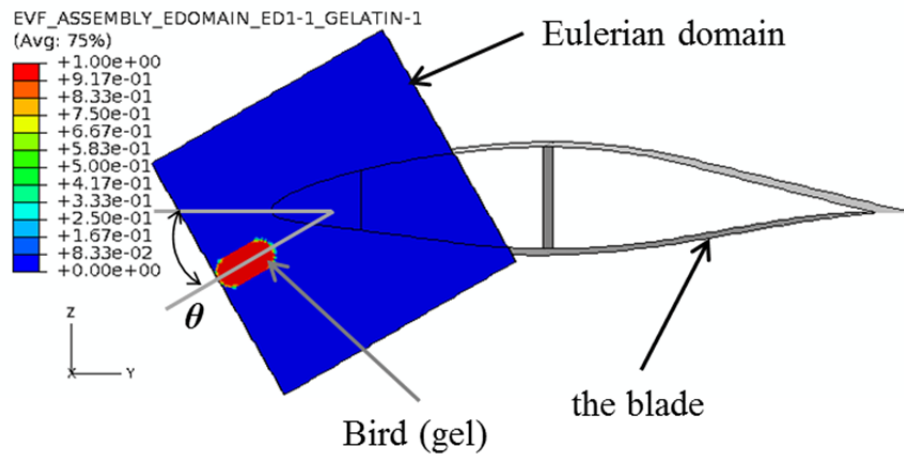


Figure 4.1. The bird described by EVF on the cross-sectional view at $r = 77.5$ m for the direct impact ($\theta = 0^\circ$) and oblique impact ($\theta = 30^\circ$) at $t = 0$ s.

4.1.3 The Blade with/without Preloads for Case Study II

In order to study the effects of impact on a loaded blade, the simulations herein consider that the blade is subjected to lift and drag forces produced at $u_w = 9.5$ m/s. Before the impact analysis, the blade undergoing these forces is analyzed in Abaqus/Standard (implicit) where the three rotations and three displacements are constrained at the blade root.

The deformed blade that contains the values of stress, strains, displacements, etc. obtained at $u_w = 9.5\text{m/s}$ as presented in Figure 4.2(a) is imported into a new analysis (explicit) with the *IMPORT option. Then, the angular velocity (ω_z) of 0.824 rad/s about the Z-axis, generated by $u_w = 9.5\text{ m/s}$, is assigned to account for centrifugal forces as presented in Figure 4.2(b). At this stage, the bird has a translational velocity of 24.5 m/s along the Z-axis, which consists of the bird velocity of 15 m/s and a wind speed of 9.5 m/s.

The benchmark case for comparison is taken to be the condition without aerodynamic loads (*i.e.*, $u_w = 0\text{ m/s}$) and thus it is not deformed and remains straight (Figure 4.3). The blade is assigned $\omega_z = 0.824\text{ rad/s}$ about the Z-axis while the initial velocity of the bird is 15 m/s along the Z-axis.

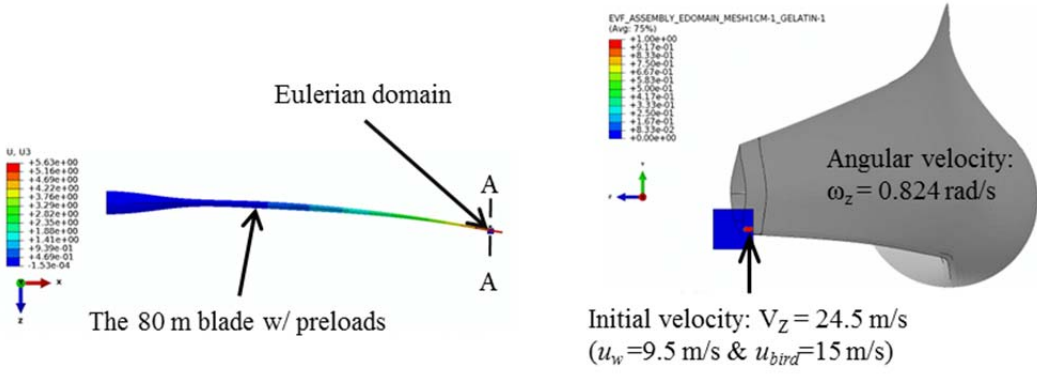


Figure 4.2. The blade with preloads before bird impact: (a) deformed shape of the blade, and (b) A-A sectional view at X = 77.5 m.

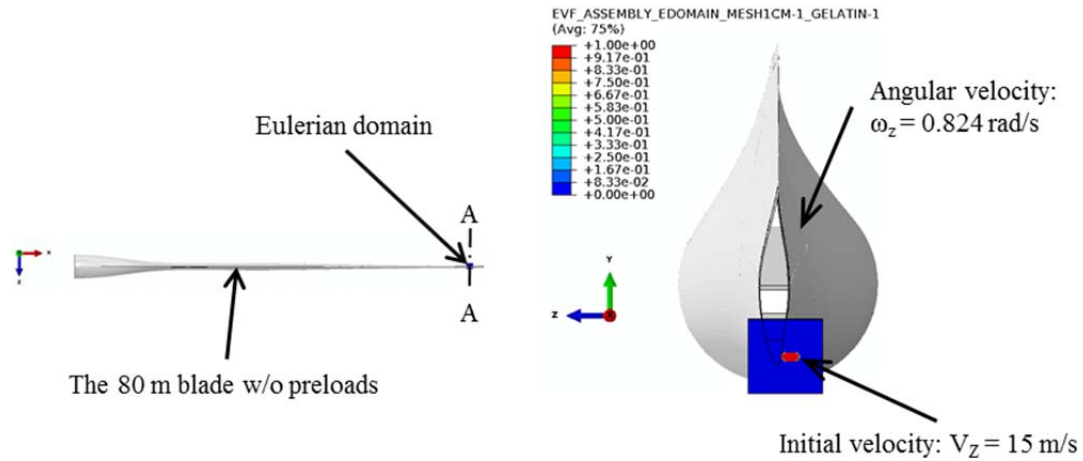


Figure 4.3. The blade without preloads before bird impact: (a) virgin state of the blade, and (b) A-A sectional view at X = 77.5 m.

4.1.4 Low Velocity Impactor Representation for Case Study II

An Eulerian bird impactor in the problem for the blade without preloads before bird impact is replaced by a Lagrangian bird impactor that follows elasto-plastic material behavior with $E = 10$ GPa, $\nu = 0.3$, $\sigma_y = 1 \times 10^6$ Pa, and $\epsilon_{fail} = 1.25$ [93]. The geometrical shape of a Lagrangian impactor is a cylinder with hemispherical ends, and the impactor consists of 43, 575 Lagrangian C3D8R/C3D6 solid elements. Note that the rest of all geometries, materials, and loading conditions are maintained.

4.1.5 The Target Structure Selections for Case Study II

Oblique impact scenarios are considered, and the impact location is at $r = 77.5$ m. The bird is initially located at an impact angle of 30° to the lower forward blade skin. The initial velocity along the Y- and the Z-axis is assigned as 70.5 m/s and 40.7 m/s, respectively.

First, the Lagrangian target structure for the bird is the 5 m tip-section of the 80 m blade modeled with S4R shell elements and the mesh size of 0.02 m. The edges of the blade at $r = 75$ m are fully constrained. No initial displacements and stresses are applied to the target structure. Secondly, the 80 m blade model is employed as the Lagrangian target. The three rotational and three displacement DOFs are constrained at the blade root. The blade is not subjected to any aerodynamic loads.

4.2 Deformed Shape

4.2.1 Displacements Due to Operational Loads

The global U_2 and U_3 displacement contours for the single blade (SB) models with balsa wood (stiff) and H160 foam (soft) cores are presented in Figures 4.4 and 4.5, respectively.

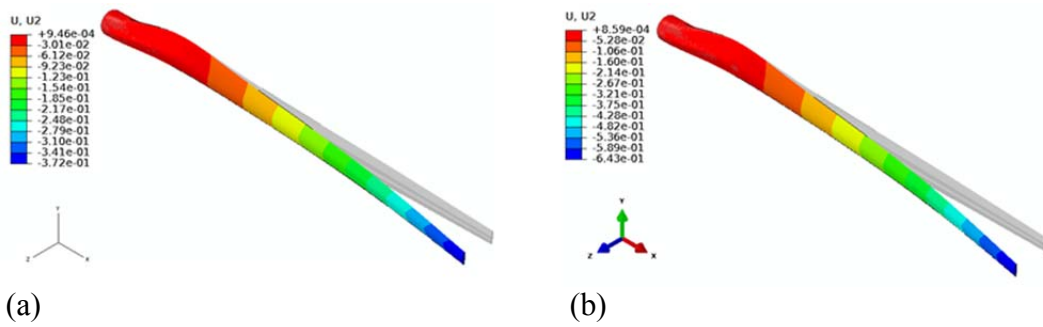


Figure 4.4. Global U_2 displacement contour of the SB model at $u_w=8.9$ m/s: (a) balsa core, and (b) foam core.

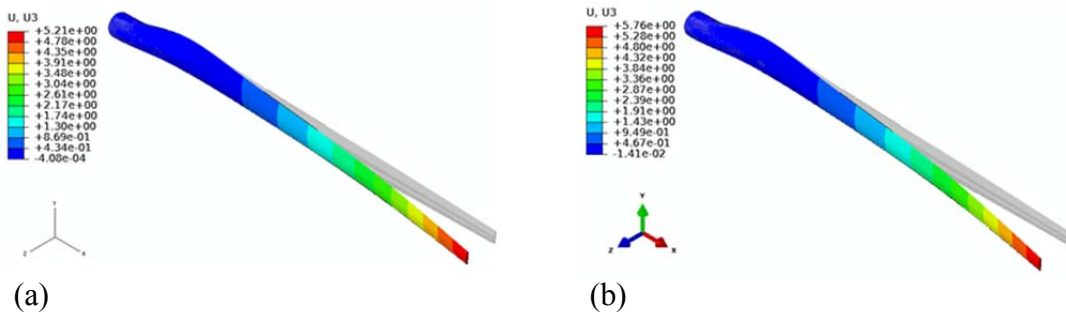


Figure 4.5. Global U_3 displacement contour of the SB model at $u_w=8.9$ m/s: (a) balsa core, and (b) foam core.

Note that the displacement contours are obtained at the loads corresponding to $u_w = 8.9$ m/s where either the core or composite layer of the blade is damaged. The blade is mainly deformed along the Z-axis, where the dominant pressure load is applied. For both models, the U_3 displacements (up to 5.76 m) are much larger than the other displacement components (less than 0.64 m).

The next parameter of interest is the flapping (the Z-axis) bending rigidities along the local rotor radius (the X-axis) since the Z-component forces dominate in the loading conditions. The bending rigidity of the blade is dependent on the flapping bending moment distribution, which is evaluated as a function of U_3 displacements at the nodes of the trailing edge. The flapping bending rigidities along the local rotor radius are approximated at eight locations in conjunction with Figure 4.5 and Equation (3.4), and they are presented in Figure 4.6. The root section and the transition section from the cylinder to airfoil are much stiffer than the airfoil section. For both models, the bending rigidity near the root is about 10^4 times higher than that it is in the vicinity of the tip. The rapid decline is seen immediately at the transition zone. It is obvious that core materials in sandwich constructions do not carry flapping bending moments. As a result, the change in elastic properties between balsa and foam cores does not exacerbate the flapping bending rigidity.

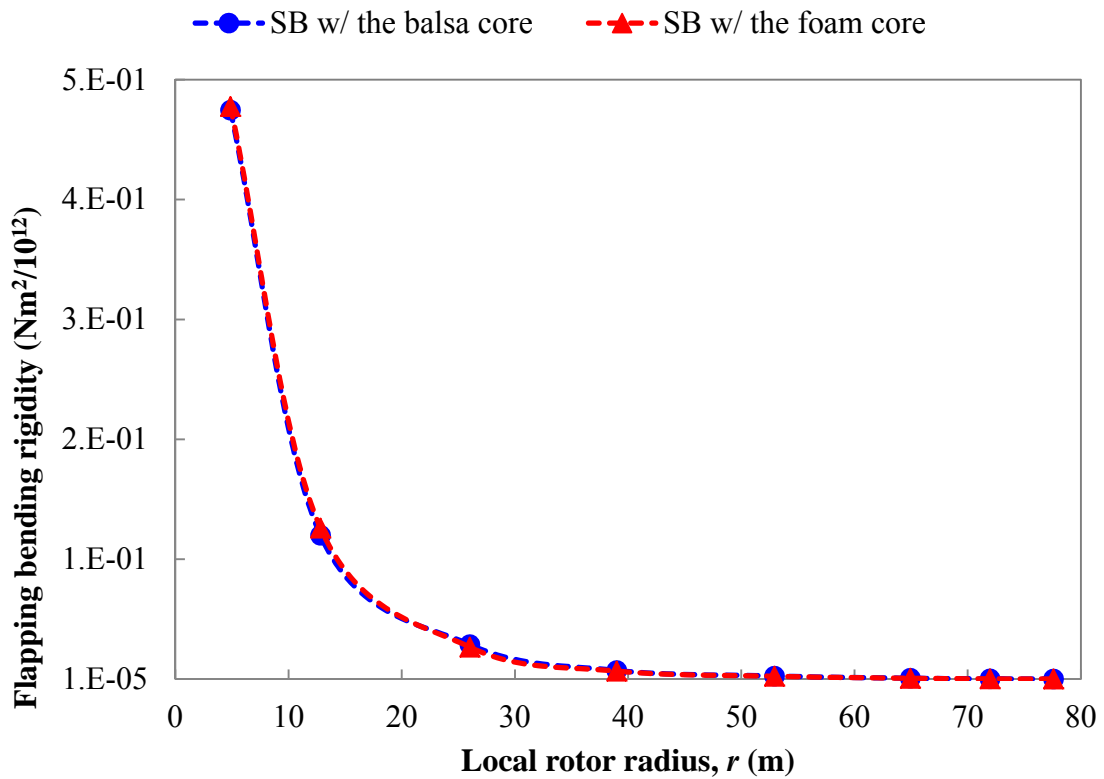
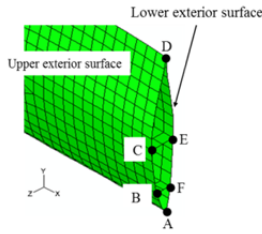


Figure 4.6. Flapping bending rigidity distribution for the SB models w/ balsa and foam cores.

Further examination of tip displacements is undertaken for the selected nodes, and the corresponding tip displacements about the three global axes are displayed in Table 4.2. The deformed cross-section maintains its original shape under loading conditions. In general, the upper surface is under compression, and the lower surface is stretched under tension.

Table 4.2. Tip displacements of the SB models w/ balsa and foam cores at 8.9 m/s

Node	SB w/ balsa core (m)			SB w/ foam core (m)		
	UX	UY	UZ	UX	UY	UZ
						
A	-0.284	-0.362	5.13	-0.362	-0.630	5.65
B	-0.307	-0.368	5.14	-0.386	-0.638	5.67
C	-0.318	-0.372	5.16	-0.396	-0.643	5.70
D	-0.280	-0.364	5.21	-0.347	-0.633	5.76
E	-0.265	-0.358	5.17	-0.336	-0.626	5.71
F	-0.275	-0.360	5.14	-0.349	-0.628	5.67

As depicted, the SB model with balsa core shows the largest U_3 displacement of 5.21 m that corresponds to 6.9% of the blade length while the U_3 tip displacement of 5.76 m is seen in the SB model with foam core corresponding to 7.6% of the blade length. Thus, there are not significant differences in the U_3 displacements between two models.

The differences in elastic properties between balsa and foam cores make an impact on the U_2 displacements since the blade does not contain any reinforcements to increase stiffness in the edge direction. Though the ratio of balsa wood to the foam in elastic modulus is 20, the maximum value of U_2 displacements for the SB models with balsa and foam cores are 0.372 m and 0.643 m, respectively. Thus, the U_2 tip

displacements of the SB model with foam core increases by 73%. Note that area moments of inertia do not change between two models due to constraining geometries and mass for the purpose of comparison.

4.2.2 Deformation Due to Impact

4.2.2.1 Deformed shape: Direct/oblique impacts

The U_2 displacement of the blade at 0.0025s and 0.01s during direct impact is presented in Figure 4.7 where the maximum values at the impact site are 6.61×10^{-4} m and 2.50×10^{-4} m, respectively. These displacements are rather small and remain localized at the impact site. As the impact forces are released, the blade starts fluctuating locally and elastic deformation recovery causes the decrease in U_2 displacements from 0.0025s to 0.01s.

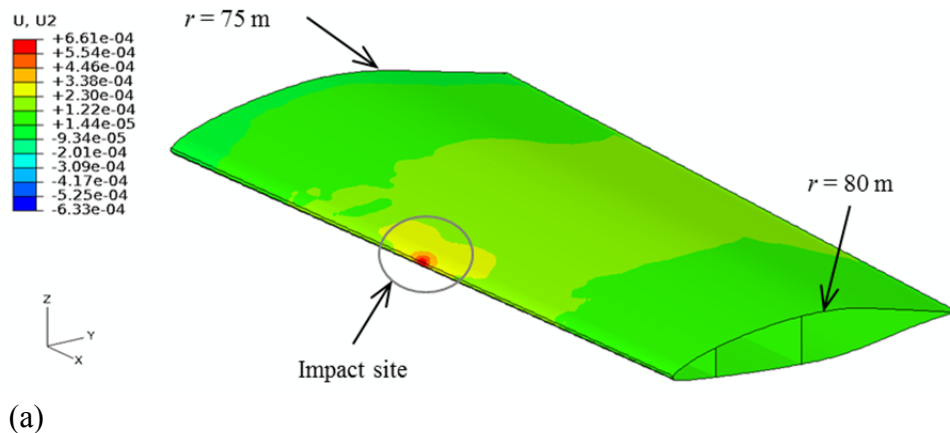


Figure 4.7. Global U_2 displacement of the 5 m tip sectional blade: (a) 0.0025s, and (b) 0.01s.

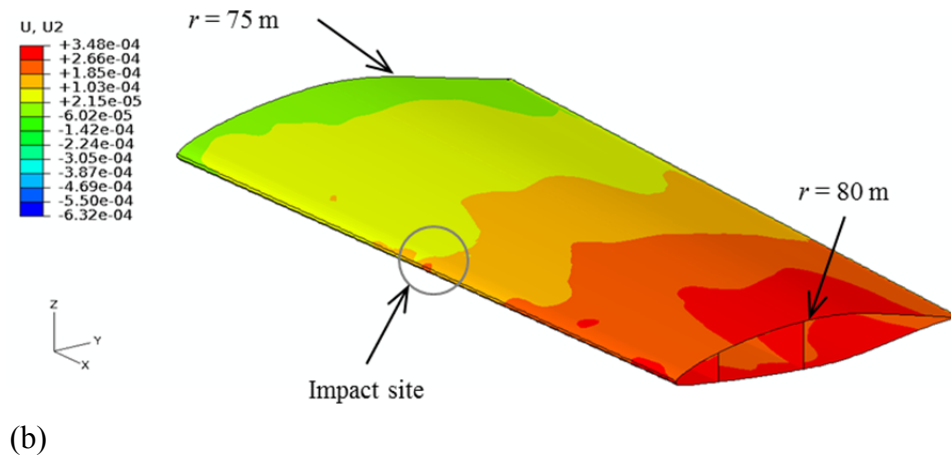


Figure 4.7. Continued.

To understand the deformation mechanism of the blade due to direct impact, the motional state of a bird (gel flow) described by Eulerian Volume Fraction is examined, and the EVF contour of the Eulerian domain is presented in Figure 4.8. Note that the unfilled elements (*i.e.*, the EVF value of zero) are deleted in the Eulerian domain of Figure 4.8 for better visualization. First, the gel contacts the leading edge of the blade and starts flowing in two directions (*i.e.*, over the upper and lower blade skin) forming a parabola with increasing time. The contact area between the blade and the gel is rather small around the leading edge, and the gel is split by the sharp form of the airfoil. This configuration helps to reduce the impact forces and thus diminishes the blade deformation.

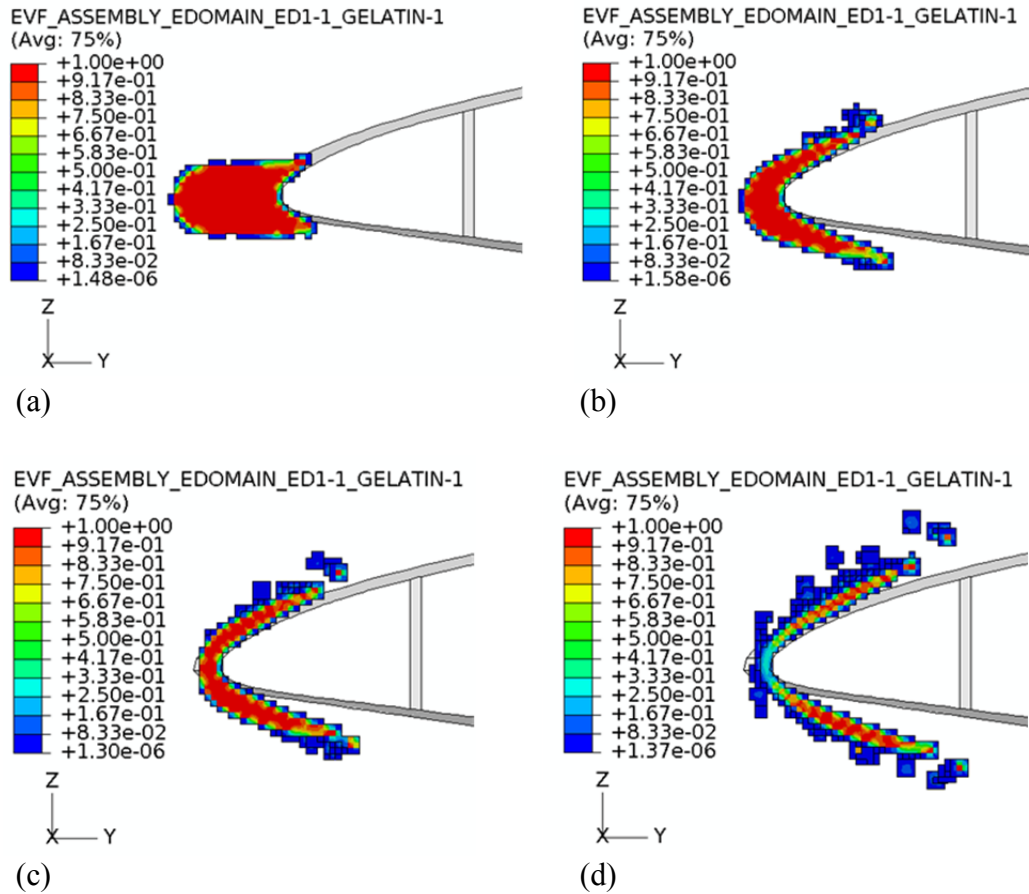


Figure 4.8. Motion states of the gel's EVF on the cross-sectional view at $r = 77.5$ m: (a) 0.001s, (b) 0.0025s, (c) 0.003s, and (d) 0.004s.

As shown in Figure 4.9(a), the event of the oblique impact starts at 0.002s when the lower forward blade skin (FB-skin) locally deflects inward. The deformed shape of the lower FB-skin on the cutaway view at $r = 77.5$ m is changed from an arc to a triangle. As shown in Figure 4.9(b), the maximum magnitude of the displacements is 0.053 m at 0.006s. The oblique impact does not cause any contact between the upper and lower FB-skins. Since the lower FB-skin toward the skin/spar cap (Point B) is adjacent to the stiff spar cap and shear web, the displacement at Point B is lower than at Point A.

After 0.006 s, local fluctuation and elastic deformation recovery lead to a decrease in the magnitude of the displacements.

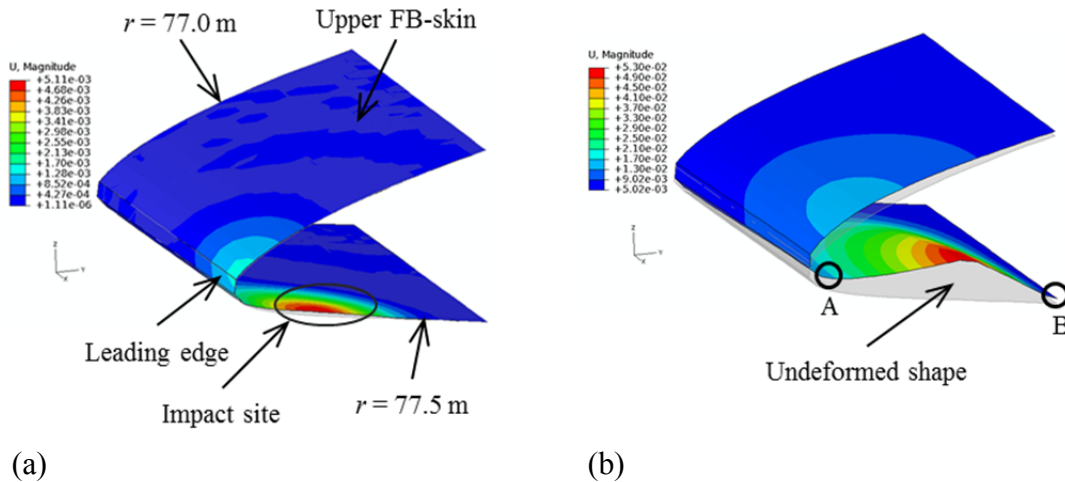


Figure 4.9. The magnitudes of the global displacements of the FB-skin ($77 \text{ m} < r < 77.5 \text{ m}$) in the 5 m tip sectional blade: (a) 0.002s, and (b) 0.006s.

4.2.2.2 Deformed shape: Preloading conditions

Since the bird is traveling along the Z-axis, U_3 displacements are critical in the impact problem. Global U_3 displacement contour in the lower blade skin of the preloaded blade is presented in Figure 4.10. The displacement of 4.72 m is generated at $r = 75 \text{ m}$ due to preloading associated with $u_w = 9.5 \text{ m/s}$, and its magnitude increases to 5.63 m toward the tip at $t = 0\text{s}$. After the impact occurs, the magnitude of U_3 displacements does not change at $t = 0.010\text{s}$ signaling that the displacements produced by impact are much smaller than those due to preloading.

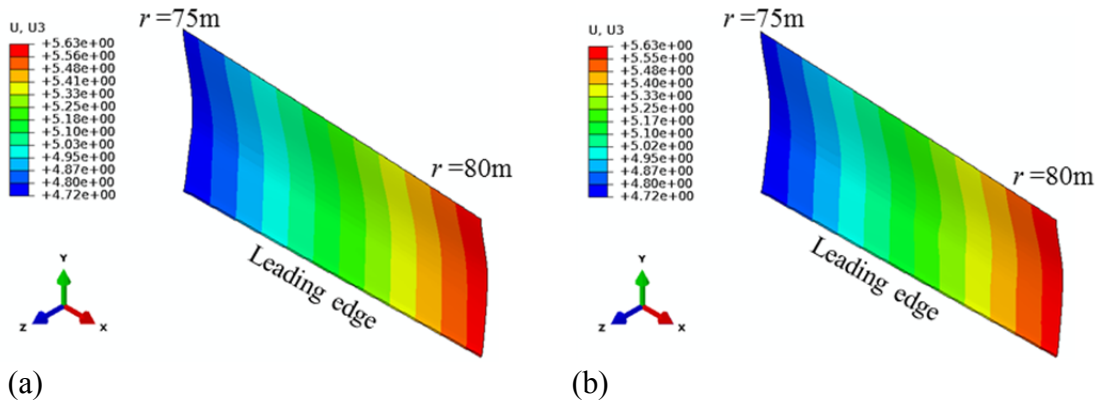


Figure 4.10. Global U_3 displacement in the lower blade skin of the preloaded blade ($75 \text{ m} < r < 80 \text{ m}$): (a) 0s , and (b) 0.010s .

For the blade without any preloads, it is seen in Figure 4.11(a) that the maximum value for global U_3 displacements in the impact site is $2.51 \times 10^{-3} \text{ m}$ and is located in the lower forward blade skin at $t = 0.001\text{s}$. Since impact site varies with time due to the blade rotation and flying bird, the greatest U_3 displacement ($9.07 \times 10^{-3} \text{ m}$) is in the skin/spar cap at $t = 0.01\text{s}$, as seen in Figure 4.11(b). The negative values of the displacements are distributed in the aft blade skin. At $t = 0.0125\text{s}$, the greatest displacement of $6.61 \times 10^{-3} \text{ m}$ is generated in the skin/spar cap while the negative displacement of $4.03 \times 10^{-3} \text{ m}$ is seen in the aft skin as illustrated in Figure 4.11(c). This displacement development arises from wave propagation and local fluctuations produced by the impact.

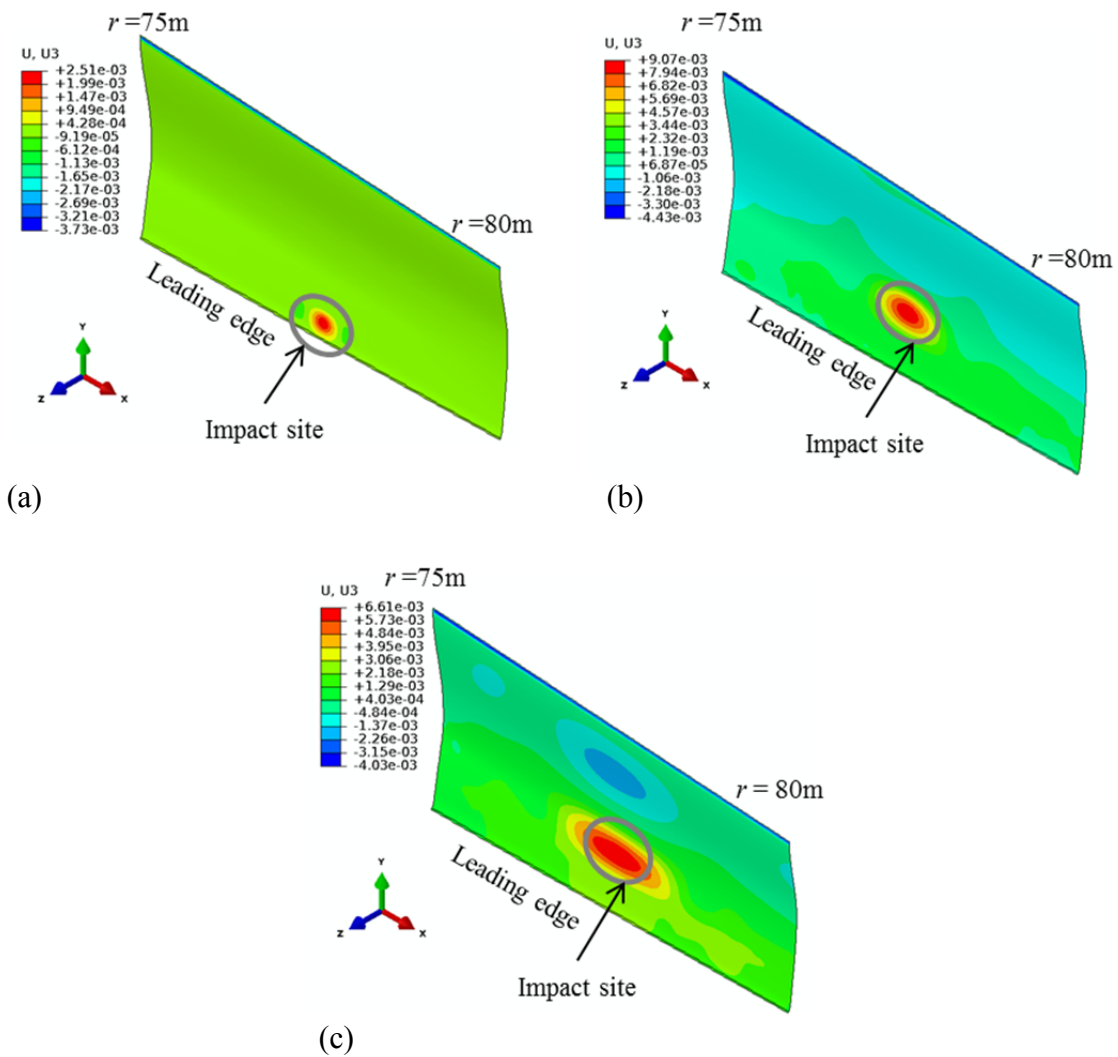


Figure 4.11. Global U_3 displacements in the lower blade skin of the blade without preloads ($75\text{ m} < r < 80\text{ m}$): (a) 0.001s , (b) 0.010s , and (c) 0.0125s .

4.2.2.3 Deformed shape: Lagrangian bird impact

Again, the Lagrangian bird impactor travels at 15 m/s along the Z -axis when the blade without preloads is rotating about the Z -axis. The global U_3 displacement of the lower blade skin is presented in Figure 4.12. Locally small deformation is seen in Figure

4.12(a), and the maximum value of the U_3 displacement at 0.002s is 1.06×10^{-2} m. Then, the greater displacements at the impact site decrease to 3.31×10^{-3} m at 0.005s due to local fluctuation and elastic deformation recovery. The impact event of the Lagrangian bird is performed during the initial 0.005s. On the other hand, the Eulerian bird impact lasts until 0.0125s by reference to Figure 4.11 that is the result of the Eulerian bird impacting on the blade without preloads. Consequently, the displacement results of the Lagrangian impact are not in agreement with those of the Eulerian impact..

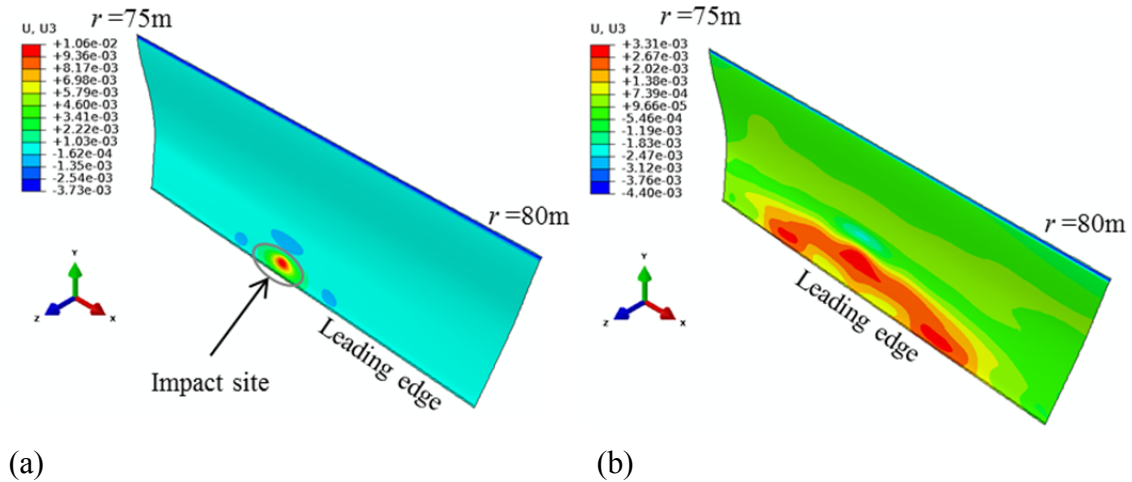


Figure 4.12. Global U_3 displacements in the lower blade skin of the blade ($75 \text{ m} < r < 80 \text{ m}$) for the case of a Lagrangian impactor: (a) 0.002s, and (b) 0.005s.

To investigate how the Lagrangian bird impactor representing a cylinder with hemispherical ends reacts on the impact event, its deformed shape is presented in Figure 4.13. It is observed that the hemispherical end on the impact side is crushed to form a

flat face at 0.002s. The impactor is shrunk by 2.77×10^{-2} m in the Z-axis while its undeformed length is 0.238 m. The rest of the impactor (*i.e.*, a cylinder and the other hemispherical end) does not deform extensively. The volume of the impactor is maintained to be the original value of 2.20×10^{-3} m³. The impactor is further compressed and the area of the flat face expands with increasing time. At 0.005s, the compressed amount of the impactor in length along the Z-axis is 4.45×10^{-2} m, and the deformed shape of the impactor on the impact side is slightly inclined to the negative Y-axis, as seen in Figure 4.13(b). The total element volume of the impactor calculated in Abaqus is 56.0022 m³ at 0.005s. However, 56 Lagrangian elements which occupy 0.13% of the total number of the elements in the impactor have an element volume of 1 m³. However, the 56 elements do not show the actual value of their volume considering the range in the initial element volume from 4.93×10^{-9} m³ to 1.13×10^{-7} m³. Additionally, it is not observed in Figure 4.13(b) that the 56 elements expand largely to have an element volume of 1 m³. Therefore, it is reasonable and realistic that the volume of 56 m³ for the 56 elements provided by Abaqus is regarded as an error value. Note that further explanations regarding this will be performed when the kinetic energy balance of the Lagrangian impactor is discussed later.

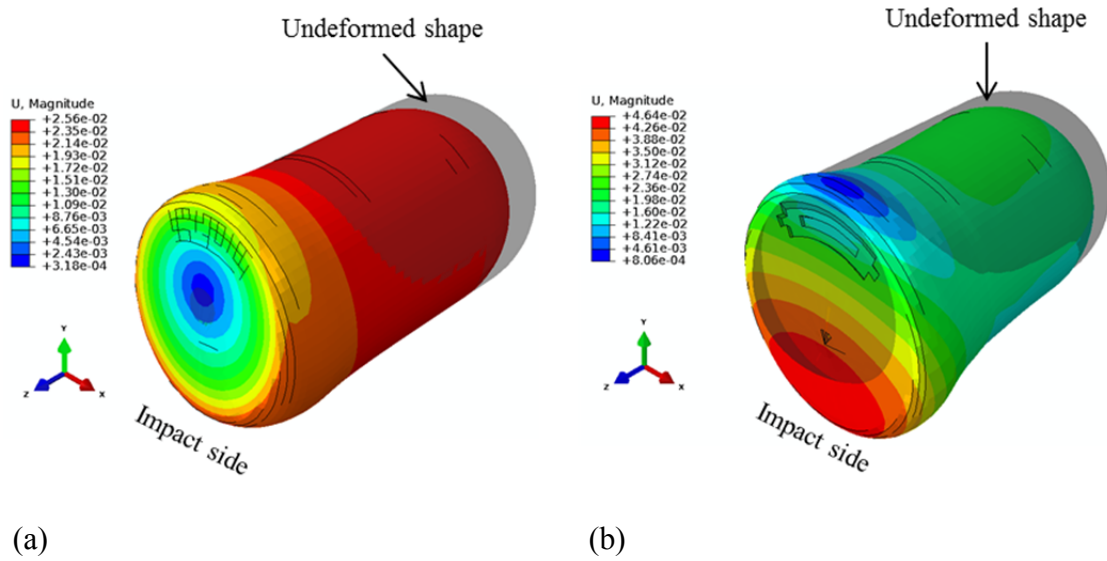


Figure 4.13. The magnitudes of global displacements of the Lagrangian impactor: (a) 0.002s, and (b) 0.005s.

4.3 Stresses, Strains, and Damage Mechanisms

The examination of stresses and strains to identify potential damage modes of the blade due to operational and impact loads are considered next. Von Mises stresses and equivalent plastic strains of core materials are compared with their allowable strength and failure strain, respectively while Hashin damage model is utilized for the composite materials.

4.3.1 Operational Loads

4.3.1.1 The SB model with balsa core

It is important to affirm that the distance to the outer layer of the skin from the centroid of the blade cross-section is greater than that of the inner layer. Also, the thickness of the skin layers is much smaller in comparison to the distance from the centroid creating higher section modulus in the outer layer than the inner layer. Thus, higher stresses appear in the outermost skin layer.

S_{11} stresses in the outermost GF fabric layer of the upper blade skin ($46 \text{ m} < r < 80 \text{ m}$) at $u_w = 12 \text{ m/s}$ are presented in Figure 4.14(a). The highest compressive stress is 94.5 MPa in the skin/spar cap region around $r = 70 \text{ m}$ as seen in Figure 4.14(a). However, this value is significantly less than the allowable strength ($X_C = 549 \text{ MPa}$). Note that S_{11} stress changes sign in the skin/spar cap area located at $60 \text{ m} < r < 75 \text{ m}$ as seen in Figure 4.14(a) indicating presence of warping. Thus, the tensile stresses are seen inside the warp, and the compressive stresses are experienced in the skin/spar cap region

outside the warp. This is attributed to the absence of balsa core, as well as insufficient reinforcement by the spar cap in this configuration.

Overall the stresses in the GF and CF layers are very small in comparison to their respective allowable strength values. The maximum value of Hashin damage initiation criteria in all composite layers at $u_w = 12$ m/s is below the damage initiated state value of 1. Therefore, no damage modes in the GF and CF layers in the root, skin, spar cap, and shear web are observed.

The balsa core of the aft blade skin defined as $60 \text{ m} < r < 70 \text{ m}$ experiences the highest compressive S_{11} stress of 5.99 MPa as illustrated in Figure 4.14(b).

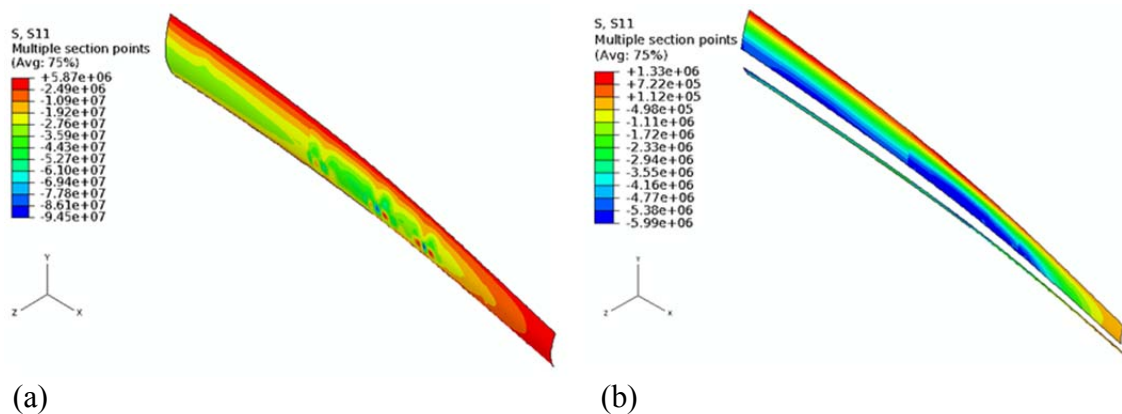


Figure 4.14. S_{11} stress contour of the upper blade skin ($46 \text{ m} < r < 80 \text{ m}$) at $u_w = 12$ m/s: (a) in the outermost GF fabric layer, and (b) in the balsa core.

Though balsa cores are used to prevent local buckling mode, yielding of the core starts at $u_w = 8.72$ m/s. The von Mises stresses in the core of the skin and web at $u_w = 12$

m/s are presented in Figure 4.15. The highest von Mises stresses spread from the boundary between the skin/spar cap, and the skin and/or web. The yielding of the balsa wood is seen in the forward skin ($20 \text{ m} < r < 32 \text{ m}$ and $60 \text{ m} < r < 70 \text{ m}$), aft skin ($20 \text{ m} < r < 32 \text{ m}$ and $46 \text{ m} < r < 75 \text{ m}$), forward web ($20 \text{ m} < r < 32 \text{ m}$), and aft web ($20 \text{ m} < r < 32 \text{ m}$ and $46 \text{ m} < r < 70 \text{ m}$) at $u_w = 12 \text{ m/s}$. The elemental areas where yielding takes place are normalized with respect to the surface area of the skin or web in that region. For example, the upper and lower aft skin experience 22.7%-33% in the region defined as $60 \text{ m} < r < 70 \text{ m}$. Furthermore, the taper blade and the different cross-sectional shape also contribute to this failure mode.

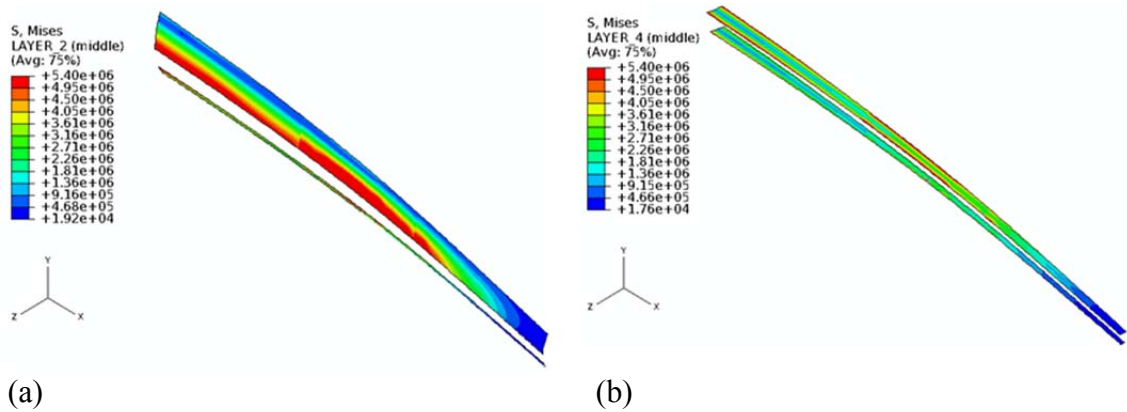


Figure 4.15. Von Mises stress contour in the balsa core ($46 \text{ m} < r < 80 \text{ m}$) at $u_w = 12 \text{ m/s}$: (a) the upper blade skin, and (b) the web.

4.3.1.2 The SB model with H160 foam core

In the blade model with foam core, damage initiation for +45°/-45° UD-GF layers of shear webs is presented at $u_w = 8.9$ m/s since their Hashin criteria reach the damage state value of 1. Results presented in this section are associated with at $u_w = 8.9$ m/s.

First, S_{11} stress contour in the outermost GF fabric layer of the upper blade skin is presented in Figure 4.16. Note that overall the upper skin experiences compressive stresses while the lower skin is in tension. The higher compressive S_{11} stress in the outermost layer occurs around $r = 20$ m and its value is 76.7 MPa. The highest compressive and tensile S_{11} stress is 11.1 MPa and 24.8 MPa, respectively, and occur in the skin/spar cap around $r = 70$ m as seen in Figure 4.16(a). These values are much smaller as compared with the allowable strength. The localized stress concentration in the skin/spar cap is observed in the SB model with foam core as well.

The stresses in the foam core that is behind the outermost layer are discussed next. S_{11} stress contours in the foam core of the upper blade skin are presented in Figure 4.17. Even though S_{11} stress is the highest, all stress components have the same order of magnitude. The highest S_{11} stress is 0.559 MPa in compression and appears at the boundary between the skin/spar cap and the skin. The maximum value of tensile S_{11} stress (0.293 MPa) is found at the trailing edge. Since the core of a typical sandwich construction tested under three or four point bending is mainly subjected to a shear, a shear generally dominates in failure modes of the core. The magnitude of the maximum S_{12} stress in the foam core is much below than its shear strength (2.6 MPa). Due to the

choice of elements, S_{13} and S_{23} stresses are not evaluated though these parameters are important. Crack initiation and propagation along the thickness's direction may occur due to S_{13} stresses. S_{23} stresses serve as important driving forces in debonding between the core and face.

Damage initiation in the shear web is also detected. The corresponding stresses and criteria in $45^\circ/-45^\circ$ UD-GF layers in shear webs ($60 \text{ m} < r < 70 \text{ m}$) are presented in Figure 4.18. The surface attached to the lower skin is designated as L.S. and similarly, U.S. designates the surface adjacent to the upper skin. As observed in Figure 4.18, tensile matrix damage in the -45° UD-GF layer is located toward the upper side of the forward shear web whereas the 45° UD-GF layer experiences the same damage mode in the region on the upper side of the forward and aft shear webs. This is attributed to the sensitivity of UD-GF layers to matrix tensile modes.

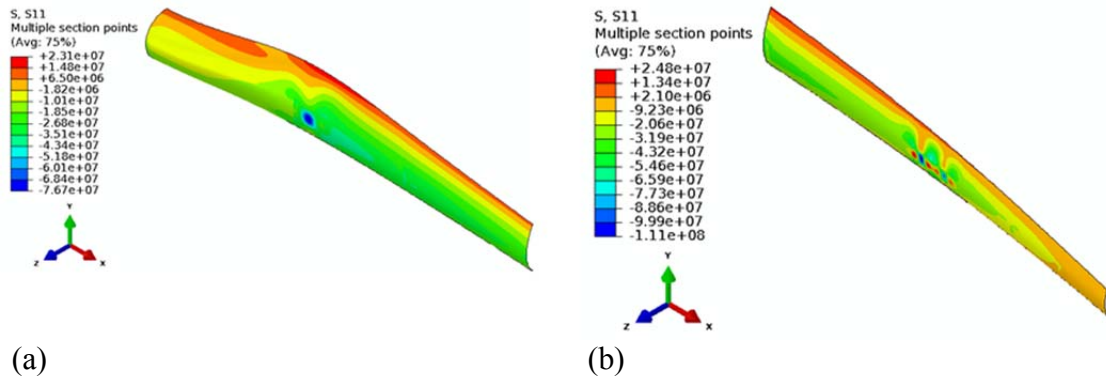


Figure 4.16. S_{11} stress contour in the outermost GF fabric layer of the upper blade skin at $u_w = 8.9 \text{ m/s}$: (a) $5.6 \text{ m} < r < 46 \text{ m}$, and (b) $46 \text{ m} < r < 80 \text{ m}$.

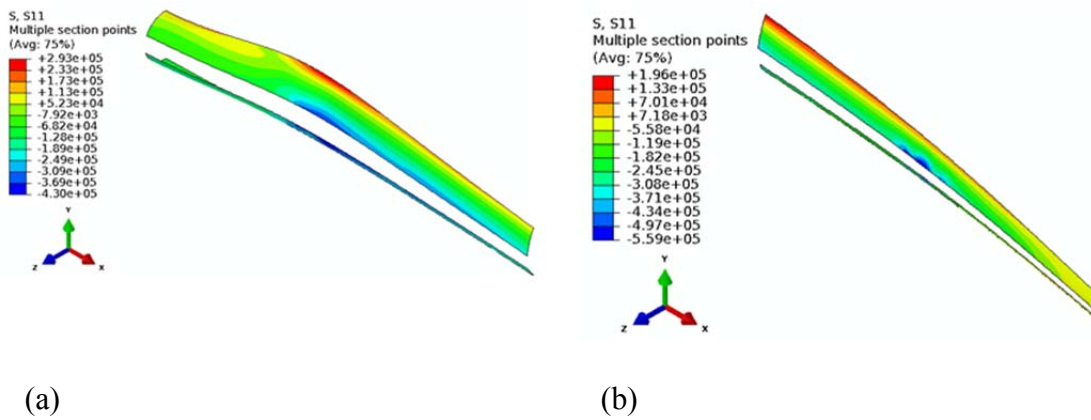


Figure 4.17. S_{11} stress contour in the foam core of the upper blade skin at $u_w = 8.9$ m/s: (a) $5.6 \text{ m} < r < 46 \text{ m}$, and (b) $46 \text{ m} < r < 80 \text{ m}$.

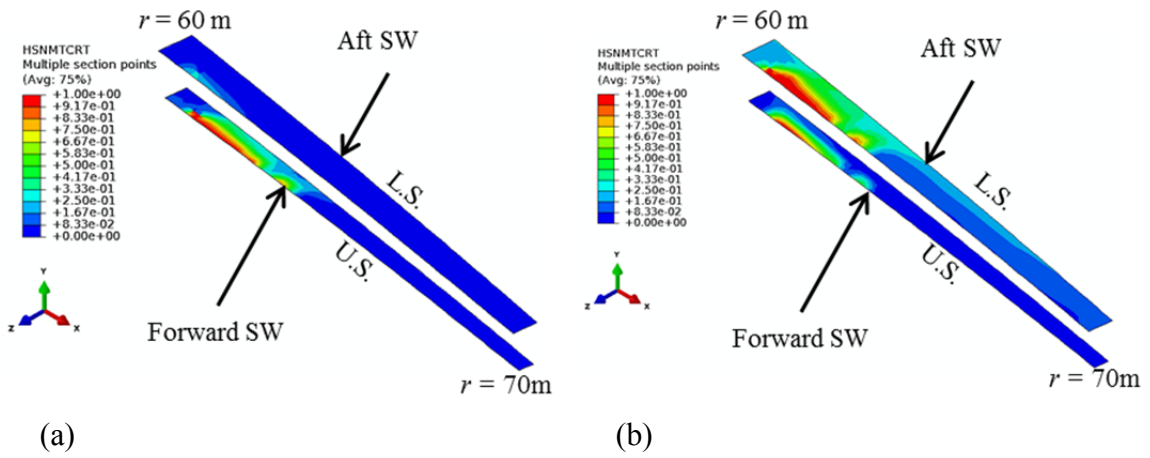


Figure 4.18. Hashin matrix tensile mode in the webs ($60 \text{ m} < r < 70 \text{ m}$) at $u_w = 8.9$ m/s: (a) -45° UD-GF layer, and (b) $+45^\circ$ UD-GF layer.

4.3.1.3 Structural integrity subsequent to local core damage

This section is dedicated to stress fields that develop after damage is initiated within the core of the sandwich blade at $u_w = 8.9$ m/s. Six elements in the upper blade skin are arbitrarily selected to determine the S_{11} stress ratio of the face to the core in the sandwich construction as presented in Table 4.3. Note that the top face of the sandwich construction corresponds to the outermost GF fabric layer of the blade skin. While the ratio for the SB model with balsa core is within 5.2 - 5.8, the ratio for the model with foam core ranges from 94 to 102. Therefore, soft materials such as Divinycell H160 foam are preferred for core materials of sandwich constructions.

For further examination, S_{11} stress distribution through shell thickness is queried at one element of the upper aft skin located at $r = 40$ m and is presented in Figure 4.19. The normalized shell thicknesses of 1 and -1 in Figure 4.19 indicate the top and bottom surface of the skin laminate, respectively. Note that there is not a strain mismatch at the interface between the layers. The S_{11} stress distribution is thus based on the continuous strains at the interface. The SB model with foam core in Figure 4.19 carries compressive stresses (-5.9 MPa for the bottom layer and - 7.2 MPa for the top layer) in its GF fabric layers while the core does not carry any axial stress. However, a similar S_{11} stress distribution is not observed for the SB model with balsa core. Thus, the bottom and top GF fabric layers are subjected to compressive stresses of 8.6 MPa and 10 MPa, respectively. In this case, the balsa core experiences compressive stresses of 1.9 MPa leading to potential core failure. Therefore, the difference in elastic properties between

the face and core of the sandwich construction is rather important to avoid core damage or failure.

Table 4.3. S_{11} stress ratio in sandwich aft blade skin at $u_w = 8.9$ m/s

r (m)	SB w/ balsa core			SB w/ foam core		
	Core (MPa)	Top face (MPa)	Ratio	Core (MPa)	Top face (MPa)	Ratio
25	-3.46	-20.0	5.8	-0.208	-21.3	102
35	-2.61	-13.5	5.2	-0.117	-11.2	96
45	-3.18	-17.0	5.4	-0.138	-14.1	102
55	-3.85	-20.5	5.3	-0.209	-20.5	98
65	-2.24	-12.5	5.6	-0.145	-14.3	99
75	-0.915	-4.95	5.4	-0.057	-5.4	94

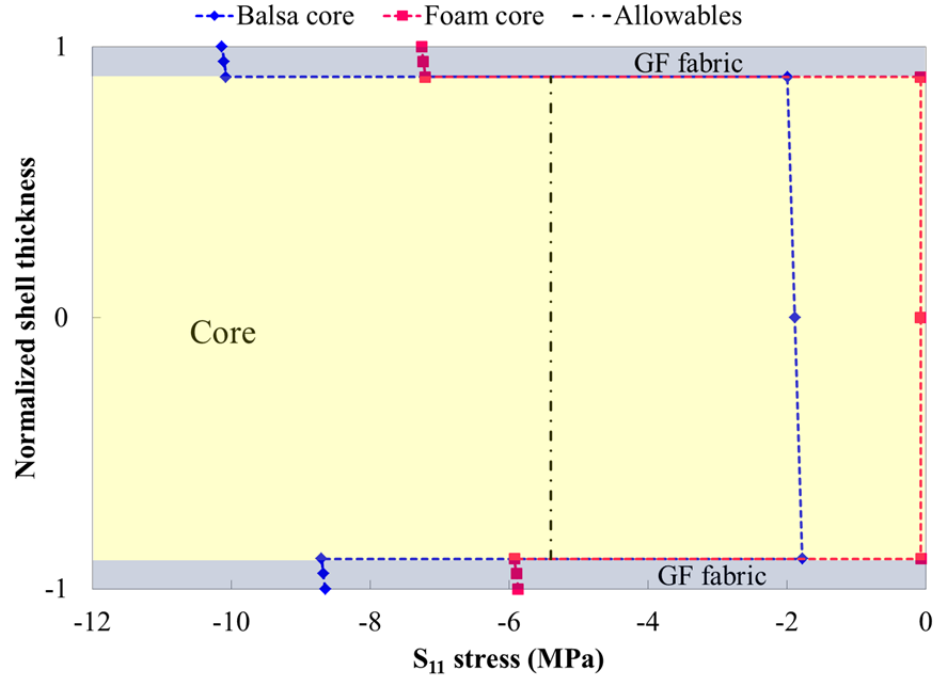


Figure 4.19. S_{11} stress distribution through shell thickness in the aft skin at $r = 40$ m at $u_w = 8.9$ m/s.

4.3.2 Impact Loads

4.3.2.1 Damage due to direct impact

The structural components of the hybrid blade (sandwich skin, shear web, and spar cap) of the 5 m blade are much more rigid than the soft body of the bird. Even though overall small deformations are observed at the time of impact, von Mises stress in the balsa core of the forward blade skin reaches its allowable strength of 5.4 MPa at the impact site. Thus, yielding of the balsa wood occurs at 0.0005s, generating an equivalent plastic strain of 0.01 at 0.006s as shown in Figure 4.20. Afterward, the plastic strain does not increase since the impact energy has already been dissipated at the leading edge. Throughout the event, the balsa core in the shear web remains below its allowable. Furthermore, no damage initiation and progression caused by the direct impact are observed in any of the composite layers.

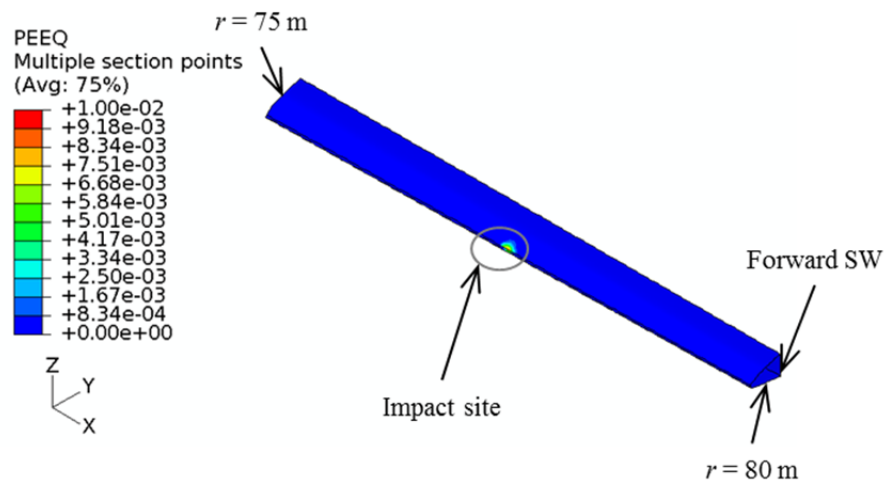


Figure 4.20. Equivalent plastic strain in the balsa core of the FB-skin and shear web (SW) at 0.006s.

4.3.2.2 Damage due to oblique impact

In the event of the oblique impact, the bird, initially located at $r = 77.5$ m, contacts the lower FB-skin. The lower FB-skin bulges out in the positive Z -axis, creating the highest compressive S_{22} stress (300 MPa) in the outermost GF fabric layer at 0.004s as shown in Figure 4.21. The highest tensile stress in the outermost layer near the shared edge is 247 MPa at 0.004s. Matrix tensile damage is observed over a region of the outermost layer that is 0.42 m in length with a surface area of $7.9 \times 10^{-3} \text{ m}^2$ as depicted in Figure 4.21(a). Note that the tensile stress that occurs at the center of the impact site at 0.005s causes matrix tension damage at 0.006s as seen in Figure 4.21(b). Consequently, the fabric layer located in this failure region is much weaker and softer than UD-GF layer and susceptible to extremely high strains in the 2-direction.

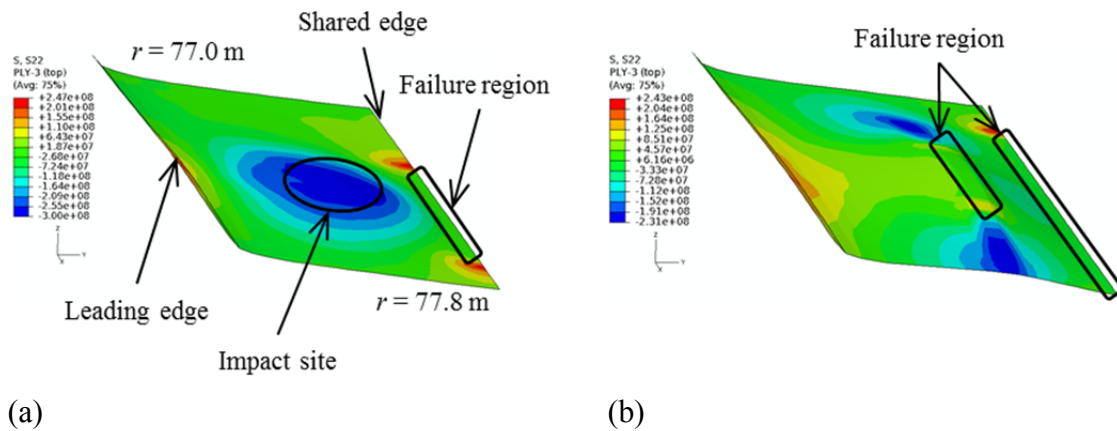


Figure 4.21. S_{22} stress in the outermost GF fabric of the lower FB-skin ($77 \text{ m} < r < 77.8 \text{ m}$): (a) 0.004s, and (b) 0.006s.

At 0.004s, the highest tensile S_{22} stress (346 MPa) is generated in the innermost GF fabric layer as displayed in Figure 4.22(a). Simultaneously, the highest compressive S_{22} stress (210 MPa) occurs in the vicinity of the shared edge. Only a single element with its area of $3.6 \times 10^{-4} \text{ m}^2$ in the high stress region of Figure 4.22(a) reaches the Hashin initiation criteria of 1. Note that the value for S_{22} stress in the failure region of Figure 4.22(b) is zero at 0.0045s since the fabric layer is degraded to reflect its matrix tensile damage mode. This region is described as 0.37 m long by $1.9 \times 10^{-2} \text{ m}$ wide at 0.0045s. Despite its growth to 0.64 m in length at 0.006s, it did not experience any additional damage modes.

Comparison of the contours in Figures 4.21 and 4.22, leads to the conclusion that the failure region near the shared edge occurs in the outermost layer only. As noted, the innermost layer at the impact site is damaged earlier and deformed severely after 0.0045s causing the increase in the S_{22} tensile stress in the outermost layer.

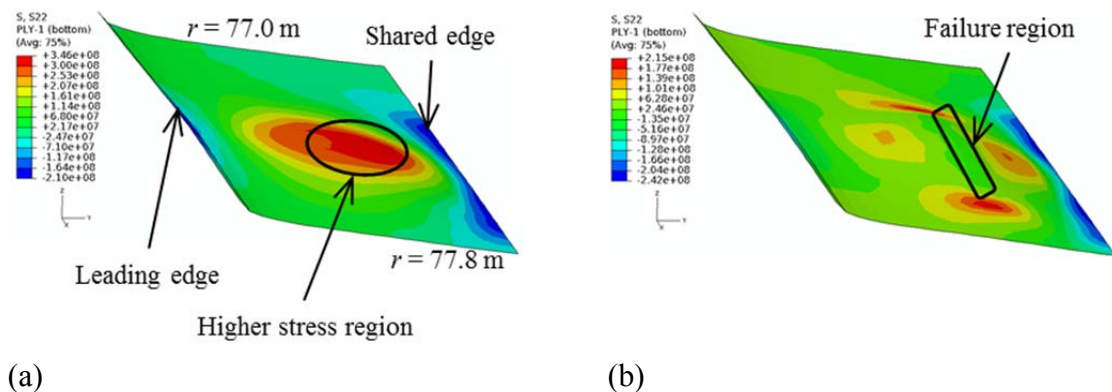


Figure 4.22. S_{22} stress in the innermost GF fabric of the lower FB-skin ($77 \text{ m} < r < 77.8 \text{ m}$): (a) 0.004s, and (b) 0.0045s.

The von Mises stress in the core of the lower FB-skin is presented in Figure 4.23. It is reported at the mid-plane of the shell elements corresponding to the neutral plane of the balsa core. After the bird strikes against the lower FB-skin, the von Mises stress in the core within the vicinity of the leading edge reaches its allowable strength at 0.002s, as seen in Figure 4.23(a). Yielding occurs at 5.4 MPa at this location where the congruence of geometric complexities of large curvature and leading edge contribute to stress concentrations. As the deformation is larger in the impact site, the yielding region is expanded along the Y-axis as seen in Figure 4.23(b) at 0.005s.

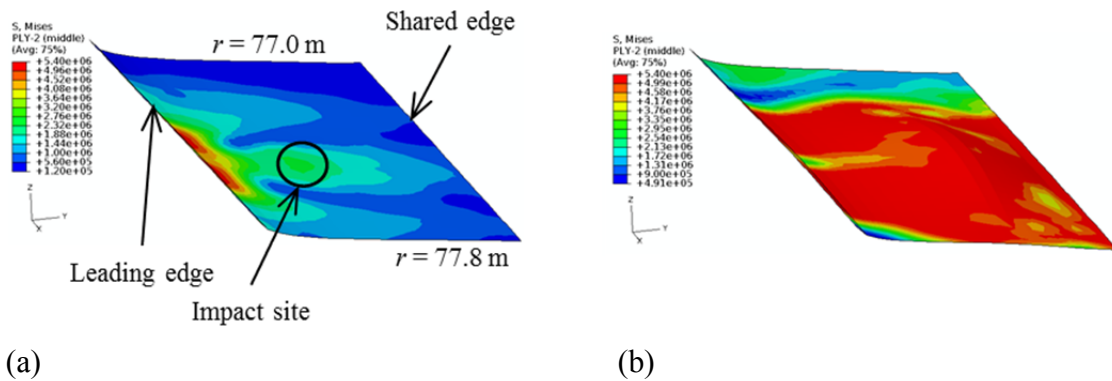


Figure 4.23. Von Mises stress in the balsa core of the lower FB-skin ($77 \text{ m} < r < 77.8 \text{ m}$): (a) 0.002s, and (b) 0.005s.

4.3.2.3 Impact response with preloading conditions

The outermost GF fabric layer of the lower blade skin in the preloaded blade ($75 \text{ m} < r < 80 \text{ m}$) experiences S_{22} stress in a range of - 6.50 MPa and 8.49 MPa at $t = 0\text{s}$ as presented in Figure 4.24(a).

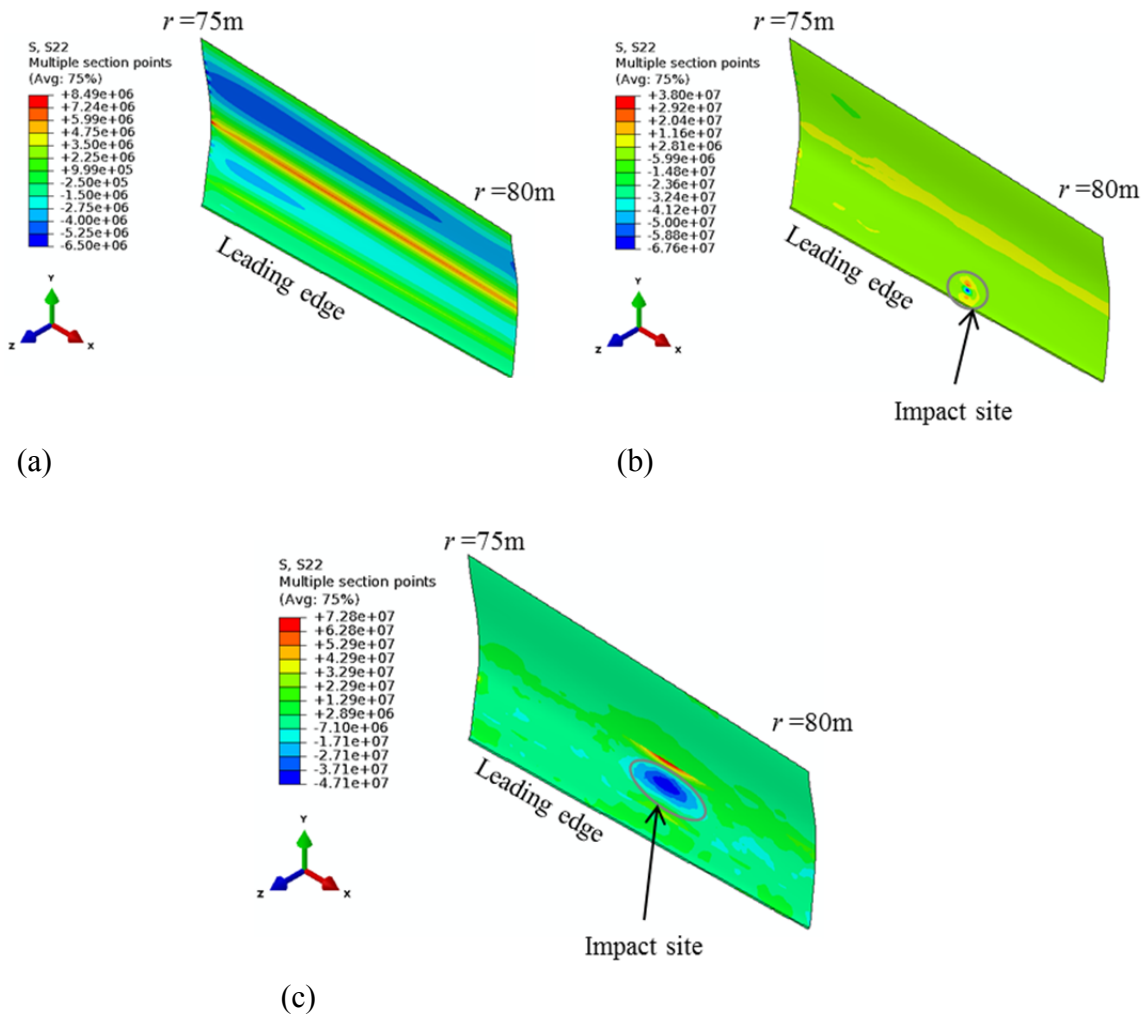


Figure 4.24. S_{22} stress in the outermost GF fabric of the lower skin of the blade w/ preloads ($75 \text{ m} < r < 80 \text{ m}$): (a) 0s , (b) 0.001s , and (c) 0.010s .

Then, the stress increases to -67.6 MPa at the impact site at $t = 0.001$ s. The compressive S_{22} stress drops when the impact site expands from the skin to the skin/spar cap. Its maximum value is 47.1 MPa in the skin/spar cap at $t = 0.010$ s as seen in Figure 4.24(c). Also, the tensile S_{22} stress of 72.8 MPa is present around the boundary between the aft skin and skin/spar cap. This high tensile stress around the boundary is attributed to the stiffness discontinuity of the laminates between the aft skin and skin/spar cap. Compressive S_{22} stresses are seen throughout the region surrounding the impact site.

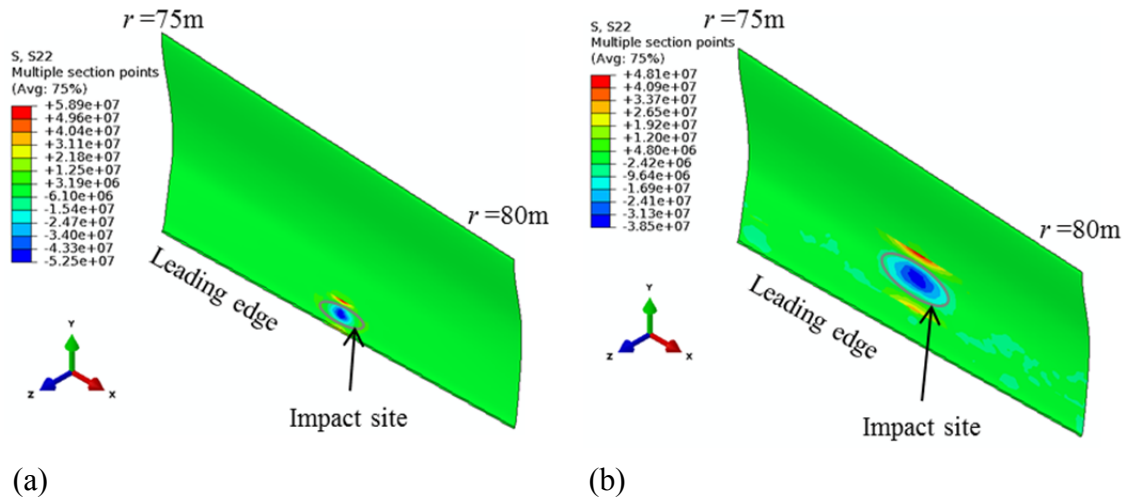


Figure 4.25. S_{22} stress in the outermost GF fabric of the lower skin of the blade w/o preloads ($75 \text{ m} < r < 80 \text{ m}$): (a) 0.001s, and (b) 0.010s.

The blade without preloads undergoes the same magnitude of centrifugal forces during impact. Its S_{22} stress field in the outermost GF fabric of the lower skin at $t = 0.001$ s is presented in Figure 4.25(a) where the lowest S_{22} stress of -52.5 MPa is seen at

the impact site, and the highest S_{22} stress (58.9 MPa) appears around the boundary between the forward skin and skin/spar cap. At $t = 0.010$ s, the maximum value for the compressive and tensile S_{22} stress are 38.5 MPa and 48.1 MPa, respectively, as presented in Figure 4.25(b).

Note that both cases (with and without preloads) exhibit the same order of magnitude in S_{22} stresses which are considerably lower than material allowables of the composite layers and the balsa core. Also note that the impact site remains localized. However, the preloaded blade showed stronger influence of impact wave propagation since the initial velocity of the impactor for the preloaded blade is higher than that for the non-preloaded blade. When a soft body impactor hits a target, a shock wave with the bulk speed of sound ($c_0 = 1.4829 \times 10^3$ m/s) is generated and propagates in the rest of the Eulerian impactor. Release waves are formed by the propagation and reflection of shock waves and cause a significant decrease in the pressure at the impact site.

4.3.2.4 Lagrangian impactor representation

When the blade without preloads rotates about the Z-axis, the Lagrangian bird impactor hits the lower forward blade skin. Since S_{22} stresses are the most interesting parameter, S_{22} stress contours in the outermost GF fabric of the lower skin ($75 \text{ m} < r < 80 \text{ m}$) at two different time points are presented in Figure 4.26. The highest compressive and tensile S_{22} stresses during the bird impact are, respectively, found in the impact site and around the boundary between the forward skin and skin/spar cap at 0.002s. The corresponding values are 201 MPa in compression and 315 MPa in tension as seen in

Figure 4.26(a). The impact site is moved upward in the Y-axis with rotating the blade. At 0.005s, the outermost layer experiences S_{22} stress in a range of -27.4 MPa and 32.1 MPa as presented in Figure 4.26(b). The highest compressive and tensile S_{22} stresses occur around the boundary between the skin/spar cap and aft skin and in the skin/spar cap, respectively. This reduction in S_{22} stresses results from the dissipation of the impact force, and S_{22} stresses do not trigger the Hashin criteria. Similarly, damaged composite layers are not observed in the Lagrangian bird impact simulation. Additionally, the von Mises stress in the balsa core of the lower blade skin at 0.002s remains below its yield strength, as presented in Figure 4.27. Therefore, the balsa core deforms elastically during the event of the bird impact.

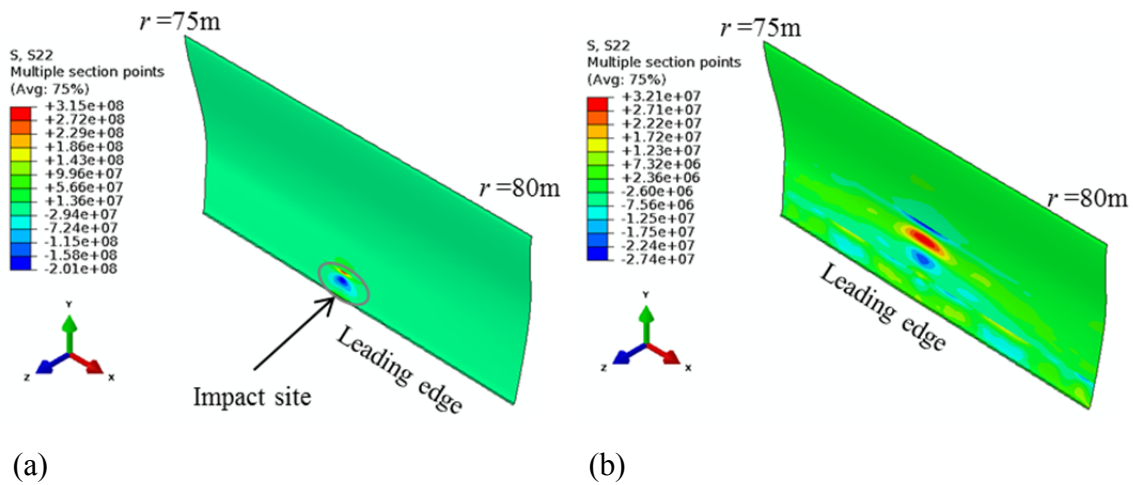


Figure 4.26. S_{22} stress in the outermost GF fabric of the lower skin of the blade w/o preloads ($75 \text{ m} < r < 80 \text{ m}$) for the case of the Lagrangian impact: (a) 0.002s, and (b) 0.005s.

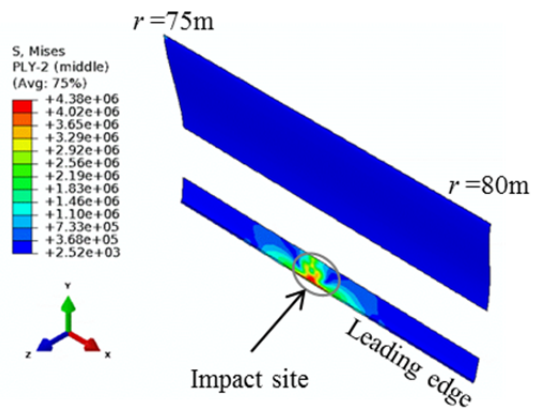


Figure 4.27. Von Mises stress in the balsa core of the lower skin of the blade w/o preloads ($75\text{ m} < r < 80\text{ m}$) for the case of the Lagrangian impactor at 0.002s.

4.4 Energy Dissipation

4.4.1 Energy Balance of Direct Impact

The direct bird impact problem that the 2kg-bird hits the leading edge of the stationary 5 m tip-sectional blade is analyzed in terms of energy balance. The kinetic and internal energy balance of the whole system containing the blade and Eulerian domain is presented in Figure 4.28. Note that the internal energy is defined here as both unrecoverable and recoverable energy stored by a system undergoing deformation. The direct impact causes the kinetic energy loss of 597 J during 0.006s while the internal energy of 20.5 J is generated. Most of the kinetic energy loss is dissipated during the impact. Kinetic energy balance of the whole system dwindles by 0.008s. After 0.008s, the kinetic energy rapidly decreases due to leaking Eulerian elements from the domain.

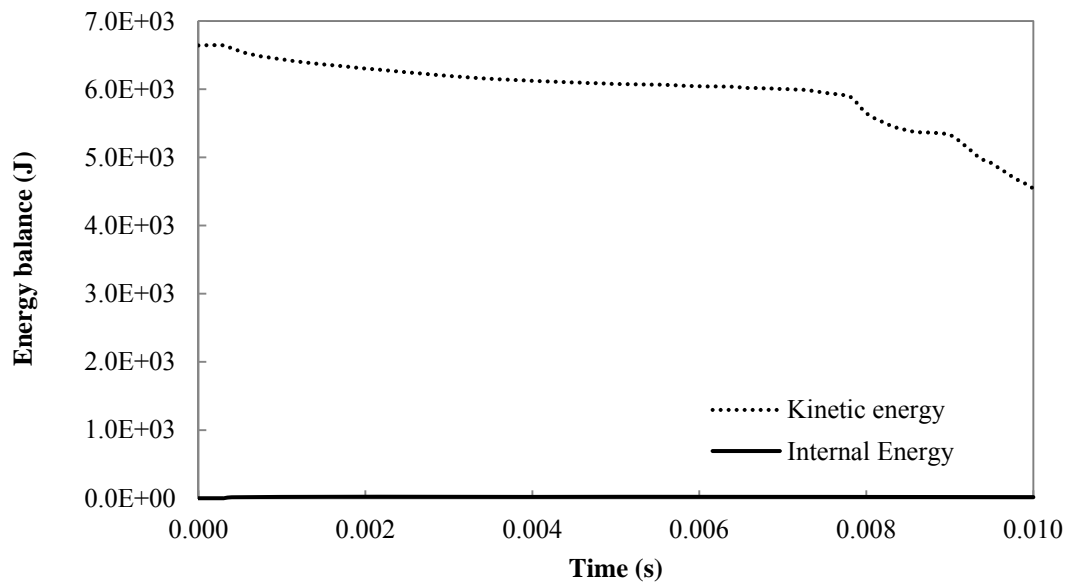


Figure 4.28. Kinetic and Internal energy balance of the whole system for the direct impact.

4.4.2 Energy Balance in Lagrangian Bird Impact

The 2kg-bird with an initial velocity of 15 m/s impacts the rotating blade. Kinetic energy balance of the Lagrangian bird impactor is plotted in Figure 4.29. The initial kinetic energy of 226 J decreases to 40.5 J at 0.003s. The energy of 185 J is converted to the elastic energy and kinetic energy of the blade and energy dissipation during the impact. The kinetic energy of the impactor increases to approach the constant value of 126 J at 0.008s. The rotating blade pushes the impactor back, transferring its kinetic energy to the impactor.

If the total element volume of the impactor (56.0022 m^3) at 0.005s is correct, the average value of its velocities can be calculated to be $6.29 \times 10^{-2} \text{ m/s}$. Note that the density of the bird's material is 911 kg/m^3 . However, the magnitude of its velocities at 0.005s is in a range from 8.18 m/s to 12.1 m/s as presented in Figure 4.30. The volumes of the 56 Lagrangian elements that Abaqus outputs are not correct values, and the 56 elements do not alter kinetic energy balance of the impactor. Therefore, the total element volume of the impactor at 0.005s could be 0.0022 m^3 .

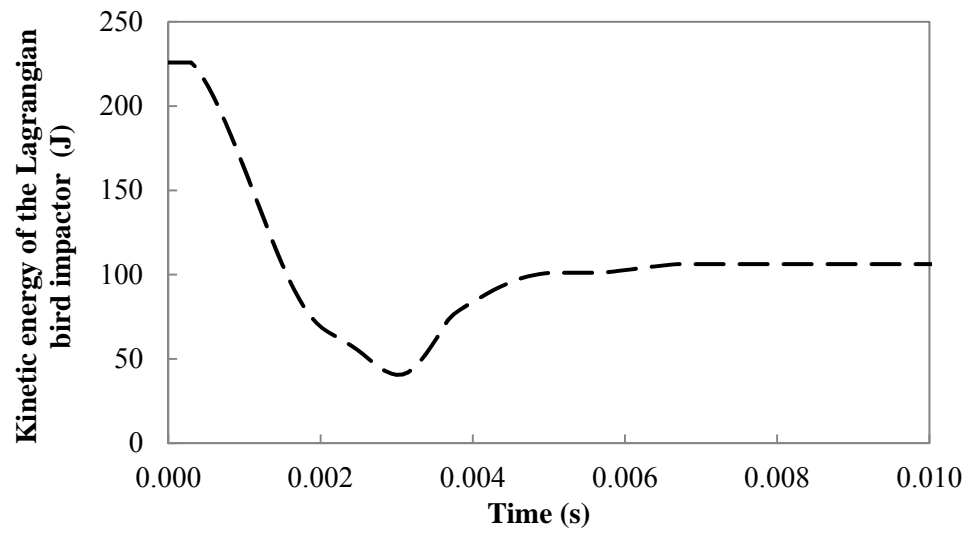


Figure 4.29. Kinetic energy balance of the Lagrangian bird impactor.

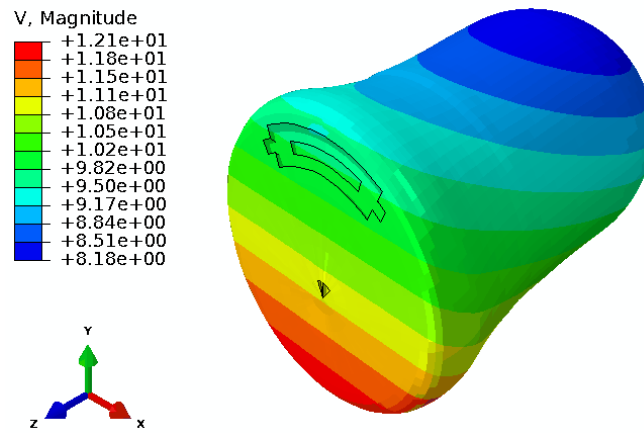


Figure 4.30. The magnitude of the impactor's velocities at 0.005s.

4.4.3 Energy Balance of Bird Impact on the 5 m vs. 80 m Blade

Herein we consider the 2kg-bird with two translational velocity components as it impacts the stationary target of a) the 5 m tip-sectional blade and b) the single 80 m blade. Neither blade is preloaded in these simulations. This comparison is performed for understanding the influence of target sizes and boundary conditions on the results.

Kinetic energy balance of two impact models with the 5 m and 80 m blades is presented in Figure 4.31. The kinetic energy balance for both models agrees well as a function of time. The initial kinetic energy of 6.64 kJ produced by the flying bird decreases to 5.25 kJ at 0.006s. This energy loss (1.39 kJ) represents both deformation of the blade and energy dissipation during the impact. Although the contact between the bird (gel) and the blade is terminated at 0.0085s, mostly the interaction between the gel and the blade takes place between 0.0015s and 0.006s. The leakage of the gel transpires after 0.008s causing a decrease in kinetic energy. However, this decrease is not significantly important since the gel moving out from the domain does not interact with the blade.

The internal energy balance of both impact models is presented in Figure 4.32. This energy consists of the recoverable strain energy of the blade and Eulerian domain, and the energy dissipated by yielding and damage. Initially, the internal energy increases to 1.02 kJ due to the impact, and then it approaches 0.95 kJ due to elastic recovery. The discontinuous path of the energy balance occurs around 0.004s when the first failure region is observed in the blade. In spite of different size and boundary conditions, the internal energy balance is quite consisted between these models. It is noted that the size

of the bird is much smaller in comparison to the global dimensions of the blade such as the blade tip radius and chord length.

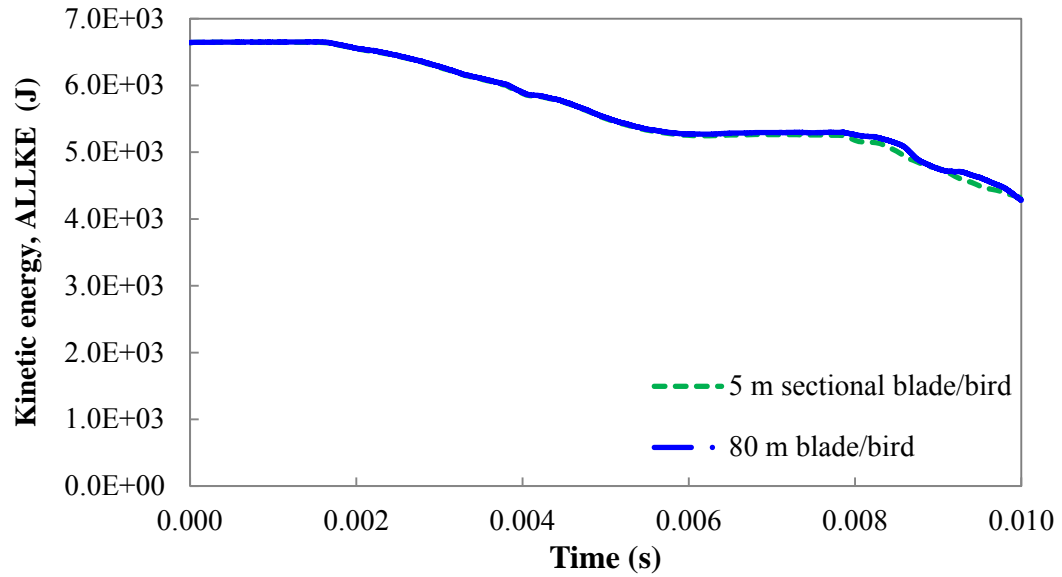


Figure 4.31. Kinetic energy balance of the impact models with the 5m and 80 m blades.

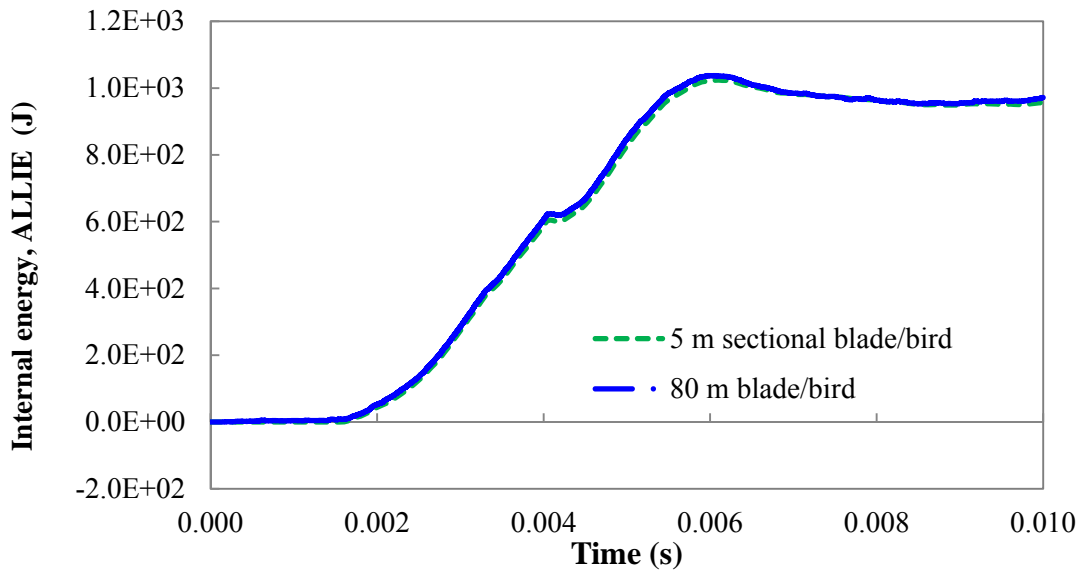


Figure 4.32. Internal energy balance of the impact models with the 5m and 80 m blades.

4.5 Frequency

The undamped natural frequencies of the non-rotating blade, lowest to the seventh, are categorized into three modes such as flapping, edge, and torsion as presented in Figure 4.33. As discussed in the previous study [70], both SB models show pure mode shapes in the lower natural frequency. The SB model with foam core is compared with the SB model with balsa core, which is treated as a baseline.

The differences in natural frequencies between two models are at most 6.8%, 33.9%, and 9.5% for flapping, edge, and torsional modes, respectively. The change in core materials causes all mode natural frequencies to be lower than the baseline model. Due to constraining geometries and mass in the comparison, the inertial properties of the SB model do not affect natural frequencies; however, the change is induced by material stiffness. While foam cores contribute to decreasing edge natural frequency, the most critical mode is still the first flapping mode. The SB model with foam core shows smaller different frequencies between the flapping and edge modes than the other model. Therefore, the replacement of core materials in the SB model does not exert a mighty influence on natural frequencies.

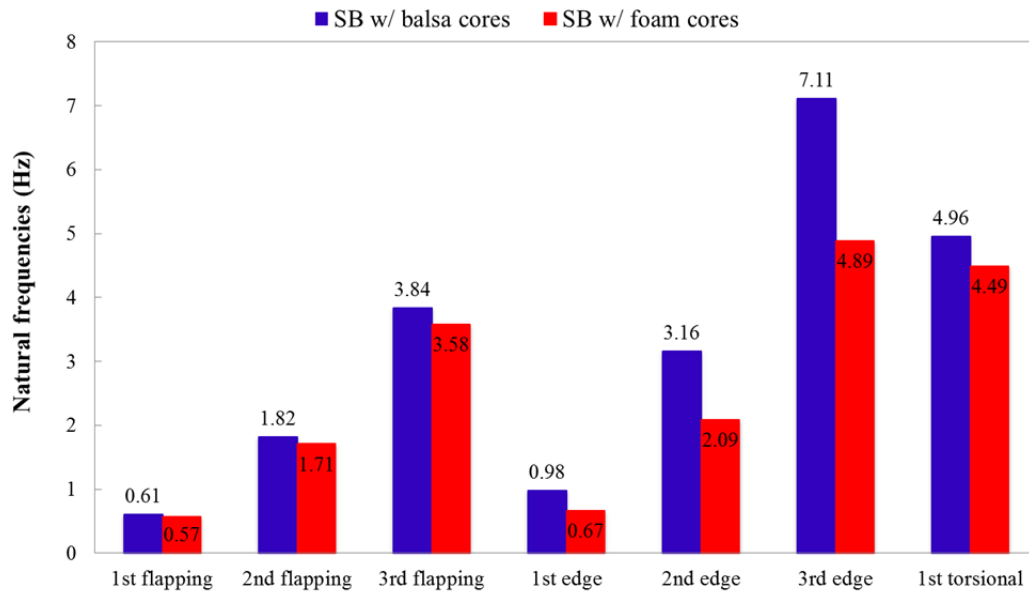


Figure 4.33. Comparison in frequencies between the SB models with balsa and foam cores.

The hinge spring stiffness of each mode of two blades is calculated by Equation (3.5), using the results of the computational frequency analyses. The estimated values of the stiffness are presented in Table 4.4. Note that there is not significantly different in inertial properties between two blades though the stiffness is dependent on mass moment of inertia.

A spar cap functions resisting of flapping bending moments and provides sufficient stiffness in the flapping direction. However, there are not any reinforcements to increase stiffness in the edge direction. Due to this configuration, the change of elastic properties induced a significant reduction in the edge stiffness.

Table 4.4. Hinge spring stiffness in Nm

Mode	SB w/ balsa core	SB w/ foam core
1st flapping	4.45×10^8	3.95×10^8
1st edge	1.15×10^9	5.45×10^8
1st torsional	1.56×10^8	1.28×10^8

4.6 Discussion

4.6.1 Core Material Comparison for Case Study I

In the single blade (SB) model with balsa core, the largest U_3 tip displacement was 6.9% of the blade length at the loads associated with $u_w = 8.9$ m/s when yielding in the balsa core was presented. Since Hashin damage initiation criteria in all composite layers were below the damage state value of 1, the GF and CF layers of the blade root, skin, shear web, and spar cap were not damaged.

In the SB model with foam core, the U_3 displacement corresponded to 7.6% of the blade length at $u_w = 8.9$ m/s where damage initiation was observed in the $+45^\circ/-45^\circ$ UD-GF layers of shear webs. The other composite layers and foam cores in the blade were not damaged since their stress ranges were below material allowables. Additionally, replacing balsa core by foam core in the SB model led to 73% increase in U_2 tip displacements though U_2 displacements were not critical.

Furthermore, it was observed that S_{11} stress changed sign in the upper skin/spar cap ($60 \text{ m} < r < 75 \text{ m}$) of both models. The phenomena indicated the formation of a warp which potentially could lead to wrinkling. The S_{11} stress ratio of the GF fabric face to the core in the sandwich skin of the SB model with foam core was much higher. The foam core was subjected to less S_{11} stress than the balsa core. The SB model with foam core experienced lower natural frequencies in all modes. The differences in natural frequencies between two models were at most 6.8%, 33.9%, and 9.5% for flapping, edge, and torsional modes, respectively. However, there was not significantly different in the first flapping natural frequency that was considered as the most critical mode

between two models. Consequently, the replacement of core materials may be acceptable.

4.6.2 Direct/Oblique Impacts for Case Study II

The 2kg-bird upon the direct impact with the 5m tip section of the 80 m blade caused a small U_2 displacement (up to 6.61×10^{-4} m). This impact scenario created minor and localized deformation in the blade since the contact area between the blade and bird remained small due to the sharp airfoil shape at the leading edge to reduce the transfer of impact forces to the blade effectively. However, the balsa core in the forward blade skin exceeded its yield strength. Stresses in composite layers were much smaller than their allowable strength. Thus, no damage initiation in the composite layers was found during direct impact.

In the oblique impact scenario, the balsa core exceeded its yield near the leading edge at 0.002s. Matrix tensile damage initiation and progression in the GF fabric layer was observed at the following locations: at outermost layer at the shared edge with shear web and skin/spar at 0.004s, at the innermost layer at the impact location at 0.0045s, and at the outermost layer at the impact location at 0.006s. However, the bird did not penetrate the lower forward blade skin. While the direct impact configuration effectively reduced the transfer of impact forces to the blade, the oblique impact forces were dissipated on the impact site where tensile damage/failure mode was observed.

4.6.3 The Blades with/without Preloads for Case Study II

The blade with preloads did not experience the displacements produced by the 2kg-bird impact since the U_3 displacements of the blade did not change between before and after the impact. On the other hand, the maximum value of the U_3 displacements in the blade without preloads caused by the 2kg-bird impact was 9.07×10^{-3} m in the skin/spar cap at $t = 0.01$ s. Wave propagation and local fluctuations produced by the impact were observed at $t = 0.0125$ s. Consequently, the blades with and without preloads survived the bird impact event without incurring any damage in the composite layers and the balsa core. The effect of preloading on the blade-bird impact response was not observed.

4.6.4 Low Velocity Impactor Representation for Case Study II

Eulerian and Lagrangian bird impactors hit the 80m blade without preloads. The results of the Eulerian bird impact simulation were summarized in Section 4.6.3. The Lagrangian impactor generated the localized small deformation in the impact site and the maximum value of the U_3 displacement at 0.002s was 1.06×10^{-2} m. During the impact event, the hemispherical end of the impactor on the impact side was crushed to form a flat face while the rest of the impactor did not deform extensively. It was not reasonable to compare the results of displacements at any time points obtained from Eulerian and Lagrangian bird impact simulations since Eulerian and Lagrangian impactors did not follow similar behaviors (*i.e.*, duration of an impact event and gradient of decreasing kinetic energy). Furthermore, the Lagrangian impactor did not caused any damages in

the composite layers and balsa cores since their stresses remained below their allowables. Therefore, two different modeling schemes for impactors did not represent identical impact problems. However, Eulerian impactors in low velocity impact problems were admissible to check if damage occurs.

4.6.5 The Target Structure Selections for Case Study II

Oblique impact scenarios with two different sizes of a stationary target (the 5 m blade and the 80 m blade) were considered. Both kinetic and internal energy balances for two impact models agreed well as a function of time in spite of different size and boundary conditions. The size of the bird was much smaller in comparison to the global dimensions of the blade such as the blade tip radius and chord length. The differences in the boundary conditions and target structure sizes did not alter the computational impact response.

5. MODULAR COMPOSITE WIND TURBINE BLADE STUDY

Herein, a modular blade design is introduced to facilitate simpler manufacturing and assembly processes without handicapping the integrity and structural response of a full single blade. Conceptual assembly mechanisms for multi-section configuration of the blade (MB Model) are addressed to assure that the displacements, stresses, strains, and vibration modes within design and safety limits. Thus, the single-continuous blade with balsa core (SB Model) is taken as the baseline in this chapter.

5.1 Introduction to the Cable Joint Concept

Power output from a wind turbine is dependent on the blade length, wind speed, and mechanical efficiency. The easiest way to match the higher power demand is to extend the blade tip radius. A multi-section modular blade concept utilizing hybrid CF/GF reinforced polymers is introduced while maintaining structural integrity and stability requirements. We will focus on the computational simulations of the blade to identify rational regions where modular segments may be introduced with appropriate joining techniques. Through computational simulations, the static and dynamic responses of the modular blade are compared with single 80 m blade responses to demonstrate both feasibility and advantages of the present joint concept.

In case of connecting two tubular modules without a change in mass, the tubular joint concept, as presented in Figure 5.1, has been proposed in discussion with Dr. W. Schneider at Texas A&M University.

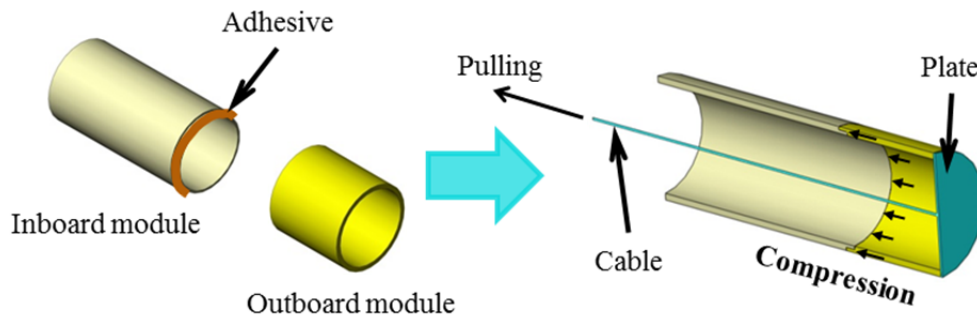


Figure 5.1. Tubular joint concept in discussion with Dr. W. Schneider.

In this concept, an inboard module is connected to an outboard module via a cable and plate. Compressive forces caused by pulling the cable through the plate are applied at the contact surfaces between the inboard and outboard module. Thus, two modules are rigidly connected due to compression. Adhesives may be used to enforce the connection. A multi-section modular blade concept is demonstrated based on the tubular joint concept. Joint segments in the modular blade are represented with an increase in laminate stiffness in the analytical simulations.

In Figure 5.1, a plate is used to apply axial compressive forces to a joint region so that two modules are connected rigidly. However, a shock absorber, like a rubber and spring/damper, may be inserted between a plate and an outboard module to avoid crush/damage at the contact face. The alternative approach to introduce compression to a joint region is tensile cable mechanisms employed for architectural and structural purposes such as cable-stayed, suspended cable, and turnbuckle cable systems. Also, cable mechanisms in a joint region are dependent on the magnitude of the required compressive force.

The schematic of a cantilever with one joint based on the tubular joint concept is depicted in Figure 5.2. The left end of the cantilever is fixed while the right end is free. The cantilever is subjected to bending and centrifugal forces. The free body diagram of the inboard module at the joint region is presented in Figure 5.3 where M is a moment generated by bending; Q , a shear force generated by bending; F_c , a centrifugal force; F , an axial force due to cable mechanisms.

The axial force sustained by cable mechanisms has to follow the following condition:

$$A\sigma_{11} - F \leq 0 \quad (5.1)$$

where A is a cross-sectional area, σ_{11} : a stress due to bending/centrifugal forces. The stress can be calculated in the equation shown below.

$$\sigma_{11} = \frac{Mc}{I} + \frac{F_c}{A} \quad (5.2)$$

where c is the perpendicular distance to the neutral axis; I , an area moment of inertia. Thus, the applied axial force of cable mechanisms has to be greater than the summation of stresses along the 1-direction over a cross-sectional area. The worst case scenario of stress states in a joint region has to be considered to determine the magnitude of an axial force for cable mechanisms. Thus, the maximum magnitude of σ_{11} in a joint region is taken, and this value multiplied by the area of a cross-section yields to the required value of an axial force for cable mechanisms.

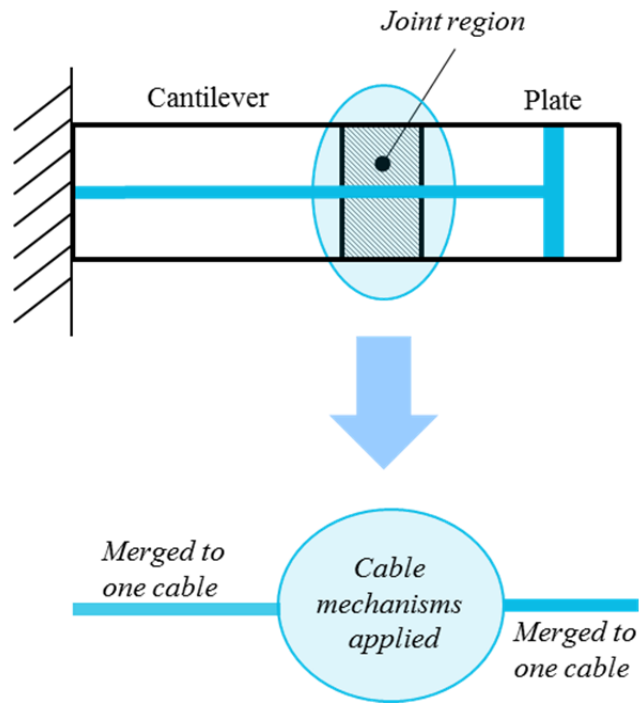


Figure 5.2. Schematic of the tubular joint concept applied for a cantilever.

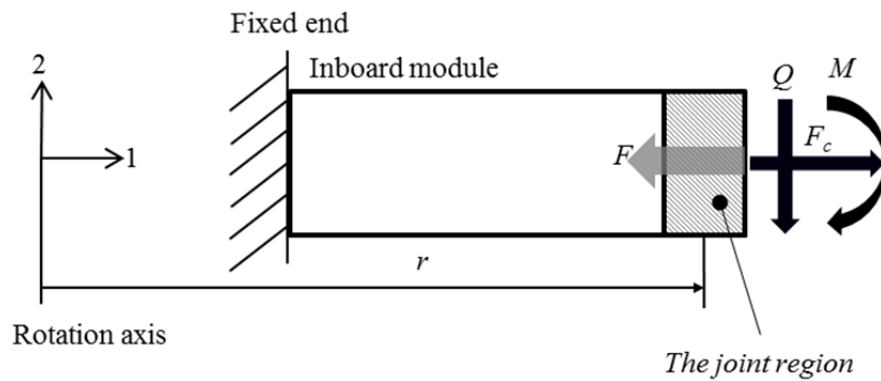
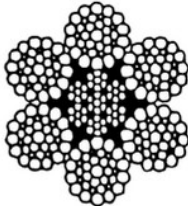
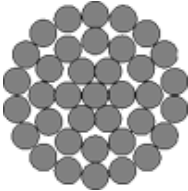


Figure 5.3. Free body diagram of the inboard module at the joint region.

Candidate cables for cable mechanism are special-purpose steel wires that are primarily employed in aircrafts and bridge construction [94-96]. The steel wires are able to provide high load capacity, high strength, excellent corrosion and temperature resistance, and non-magnetic characteristic. Additionally, carbon fiber composite cables (CFCCs) are potentially adopted as a substitute for the steel wires since CFCCs provide higher specific strength/stiffness, better corrosion resistance, and better fatigue performance in comparison with the steel cables [97, 98]. These cables can be supplied from commercial vendors, and the specifications of the cables are presented in Table 5.1. When the required axial force for cable mechanisms is greater than the breaking strength of a single cable, using multiple cables or increasing a diameter of a single cable may be necessary to sustain the required axial force.

Table 5.1. Specifications of stainless cables and CFCCs

	Diameter (m)	Construction	Cross-section	Breaking strength (N)	Unit mass (kg/m)
Stainless cables [95]	0.04	IWRC 6×WS(36)		9.11×10^5	6.46
	0.06			1.92×10^6	14.5
CFCCs [97]	0.04	1×37		1.2×10^6	1.53

5.2 Modular Blade Representation

This concept is illustrated by considering the 80 m blade to be manufactured in two modules and then joined together as depicted schematically in Figure 5.4. Physical geometries of the inboard and outboard modules seen in Figure 5.4(a) are considered. Thus, the inboard module extends from $r = 4$ m to $r = 40.05$ m, and the outboard module is defined as 37.95 m $< r < 80$ m. The projection of the inboard module is inserted inside the outboard module; thus, the projection is overlapped with the outboard module, creating a joint region of the blade with a length of 2.1 m.

To create the FE modular blade model, the joint-transition-region is placed at 32 m $< r < 46$ m as presented in Figure 5.4(b). For clarity of visualization, the upper blade skin in Figure 5.4(b) and (c) is hidden, and FBS, BS/SC, ABS, and SW denote the forward blade skin, the blade skin/spar cap, the aft blade skin, and the shear web, respectively. It is assumed that the reinforcement region between the inboard module and outboard module are perfectly bonded at $r = 37.95$ m in this study. Furthermore, this region is computationally described as a single surface. Therefore, the joint-reinforcement section marked by gray solid lines in Figure 5.4(b) is defined as 36.9 m $< r < 41.10$ m. As seen in Figure 5.4(c), the overlapping region surrounded with red solid lines is depicted as Joint-SW and Joint-BS/SC, occupying 37.95 m $< r < 40.05$ m. The reinforced laminates are employed for the regions such as Reinf.-FBS, Reinf.-ABS, Reinf.-SW, and Reinf.-BS/SC surrounding the overlapping region. Reinf.-FBS and Reinf.-ABS are located between 36.9 m $< r < 41.1$ m (4.2 m in length), whereas Reinf.-SW and Reinf.-BS/SC are located at 36.9 m $< r < 37.95$ m (1.05 m in length), and at

$40.05 \text{ m} < r < 41.10 \text{ m}$ (1.05 m in length). The FE models are created in Hypermesh, and then analyzed in Abaqus/Standard for both static and natural frequency simulations with S3R/S4R linear shell elements. The mesh size of 0.15 m is employed generating 41,368 elements. The three rotations and displacements are fully constrained at the blade root, and the blade is subjected to both aerodynamic and centrifugal forces as operational loads.

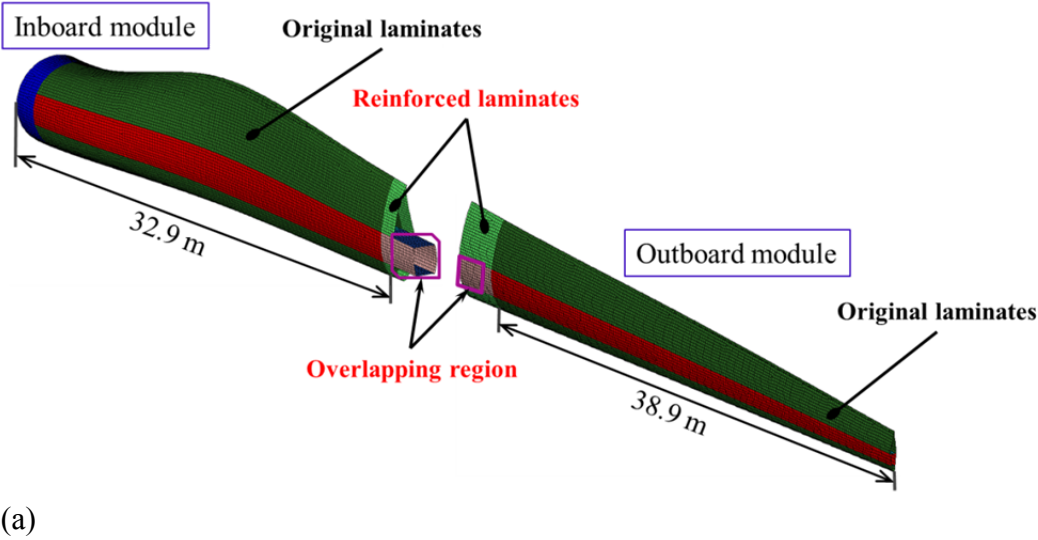
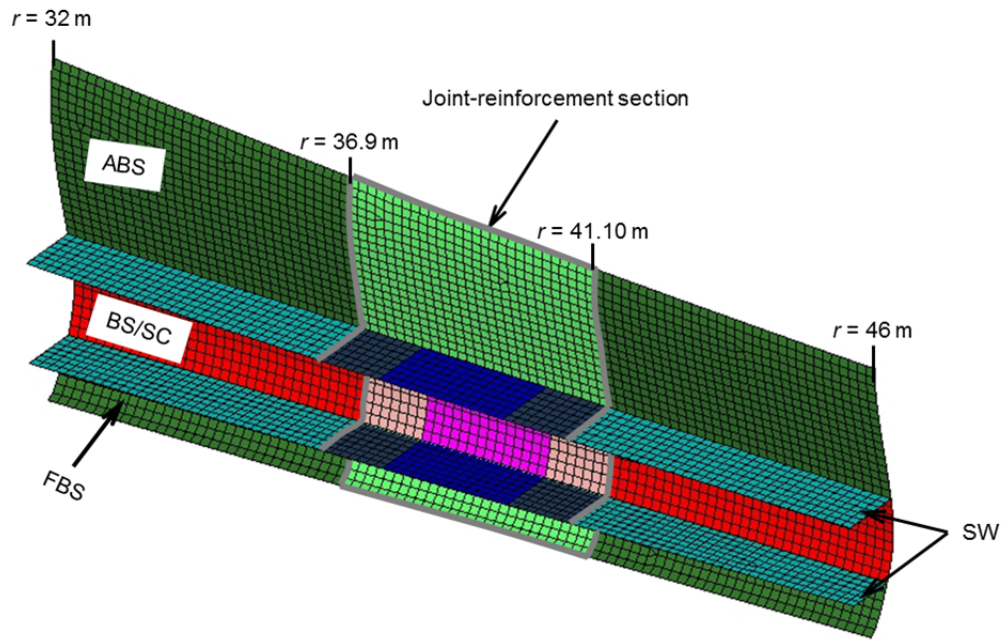
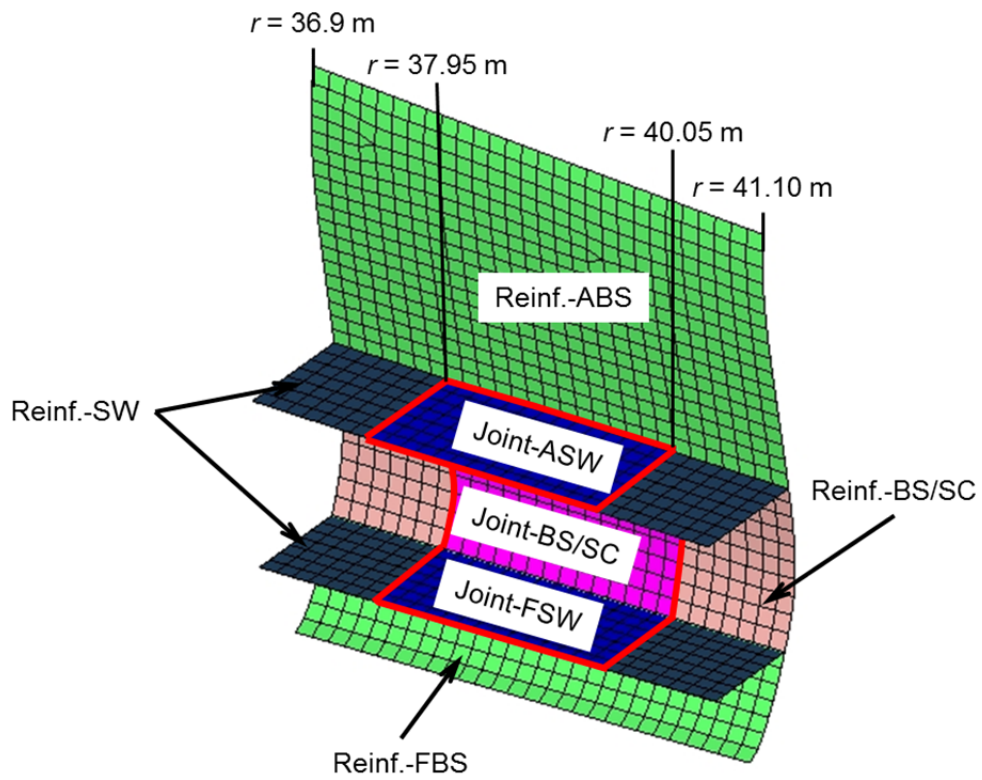


Figure 5.4. The conceptual schematic of the modular blade: (a) inboard and outboard modules, (b) joint-transition-region ($32 \text{ m} < r < 46 \text{ m}$), and (c) joint-reinforcement section ($36.9 \text{ m} < r < 41.1 \text{ m}$).



(b)



(c)

Figure 5.4. Continued.

For the MB Model, elastic moduli and shear moduli of UD-GF, GF fabric, CF fabric, and balsa wood in the joint and reinforcement regions are amplified by 3X and 1.5X of their typical values utilized in the SB Model. These values are presented in Table 5.2 with the following nomenclature: E_{FBS} , the stiffness of the forward blade skin laminate; $E_{BS/SC}$, the stiffness of the blade skin/spar cap laminate; E_{ABS} , the stiffness of the aft blade skin laminate; E_{SW} , the stiffness of the shear web laminate. The rest of all geometry and material details in the MB Model are maintained to the SB Model.

To assess the effect of increased mass in the joint-reinforcement section to natural frequencies, two types of modular blade models are considered; MB Model and MB-IW Model. It is assumed that the mass change of the joint-reinforcement section is not presented in the MB model. In the MB-IW Model, the density of materials used in the joint and reinforcement are considered to increase by 20% and 10%, respectively as presented in Table 5.3.

Table 5.2. Laminate stiffness in the joint-transition-region

Range of r (m)	Length (m)	Stiffness of laminates			
		Forward blade skin	Blade skin/spar cap	Aft blade skin	Shear web
32-36.9	4.9	E_{FBS}	$E_{BS/SC}$	E_{ABS}	E_{SW}
36.9-37.95	1.05		$1.5 \times E_{BS/SC}$		$1.5 \times E_{SW}$
37.95-40.05	2.1	$1.5 \times E_{FBS}$	$3 \times E_{BS/SC}$	$1.5 \times E_{ABS}$	$3 \times E_{SW}$
40.05-41.10	1.05		$1.5 \times E_{BS/SC}$		$1.5 \times E_{SW}$
41.10-46	4.9	E_{FBS}	$E_{BS/SC}$	E_{ABS}	E_{SW}

Table 5.3. Density of the materials used for frequency analysis in kg/m³

	UD-GF	GF fabric [0/90]_s	CF fabric [0/90]_s	Balsa
Original	2,100	2,100	1,600	155
Reinforced	2,310	2,310	1,760	170.5
Joint	2,520	2,520	1,920	186

5.3 Structural Responses Analyses

5.3.1 Analysis Description

The single-continuous blade (SB Model) and the modular blade with one joint (MB Model) are analyzed in Abaqus/Standard for both static and natural frequency simulations. The three rotations and displacements are fully constrained at the blade root, and the blade is subjected to both aerodynamic and centrifugal forces as operational loads described in Section 3.2. All results presented below are obtained at the loads corresponding to $u_w = 9.3$ m/s where the von Mises stress of the core in both models exceeds its allowable.

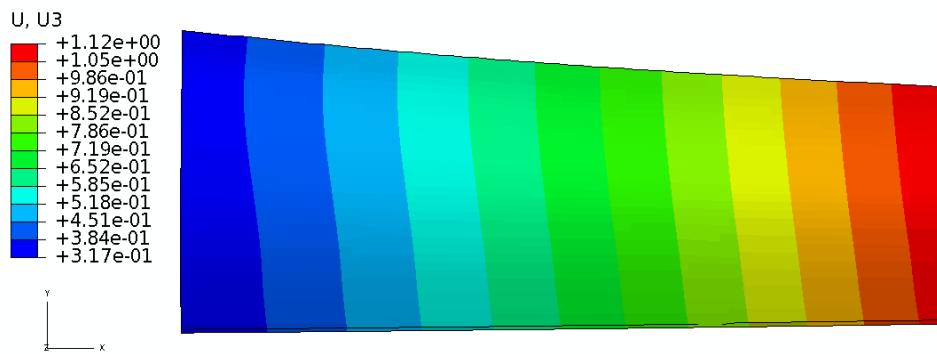
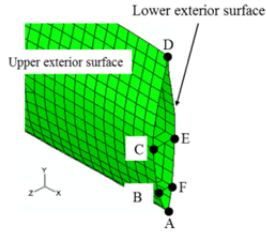
5.3.2 Displacement Results

The selected nodes and the corresponding tip displacements are shown in Table 5.4. U_1 and U_2 displacements of the MB Model are reduced by 6% and 3%, respectively from the SB Model. However, the U_3 displacement is the greatest component for both models. The joint-reinforcement section of the MB Model displays only 3% reduction in the U_3 displacement in comparison to the SB Model.

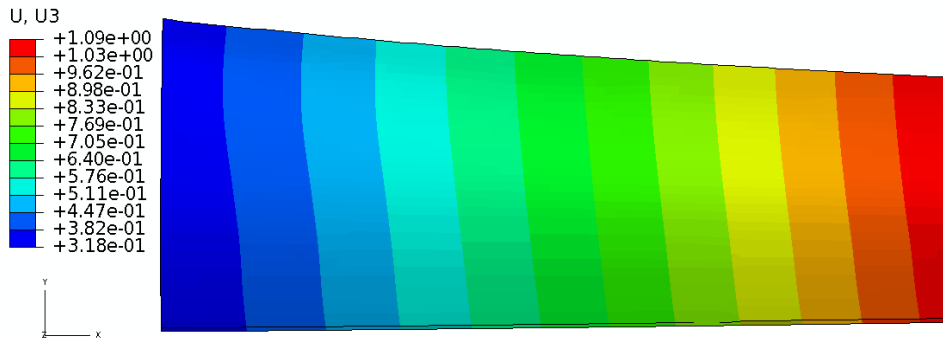
The global U_3 displacement contours of the upper blade skin in the region ($32 \text{ m} < r < 46 \text{ m}$), which has the joint-reinforcement section in the MB Model, are presented in Figure 5.5 to further illustrate that the modular blade as designed remains unchanged from the SB Model response.

Table 5.4. Tip displacements of the SB Models and MB Model

Node	SB Model (m)			MB Model (m)		
	UX	UY	UZ	UX	UY	UZ
A	-0.276	-0.360	5.09	-0.260	-0.349	4.94
B	-0.298	-0.367	5.10	-0.282	-0.356	4.95
C	-0.309	-0.371	5.12	-0.293	-0.359	4.98
D	-0.272	-0.362	5.18	-0.256	-0.351	5.03
E	-0.257	-0.356	5.13	-0.242	-0.345	4.98
F	-0.266	-0.358	5.10	-0.251	-0.347	4.95



(a)



(b)

Figure 5.5. Global U_3 displacement contours of the upper blade skin, $32 \text{ m} < r < 46 \text{ m}$: (a) SB Model, and (b) MB Model.

5.3.3 Stress Results

The stresses in the GF and CF layers are very small in comparison to their allowable strength in the SB Model and MB Model. The following observations are made on S_{11} stress contour which is the largest component in the stress field. The asymmetric airfoil cross-section leads to higher S_{11} stresses in the upper blade skin than the lower blade skin. The highest compressive stress in the outermost GF fabric layer of the upper skin for the SB Model and MB Model is 44.1 MPa and 44.3 MPa, respectively, as shown in Figure 5.6.

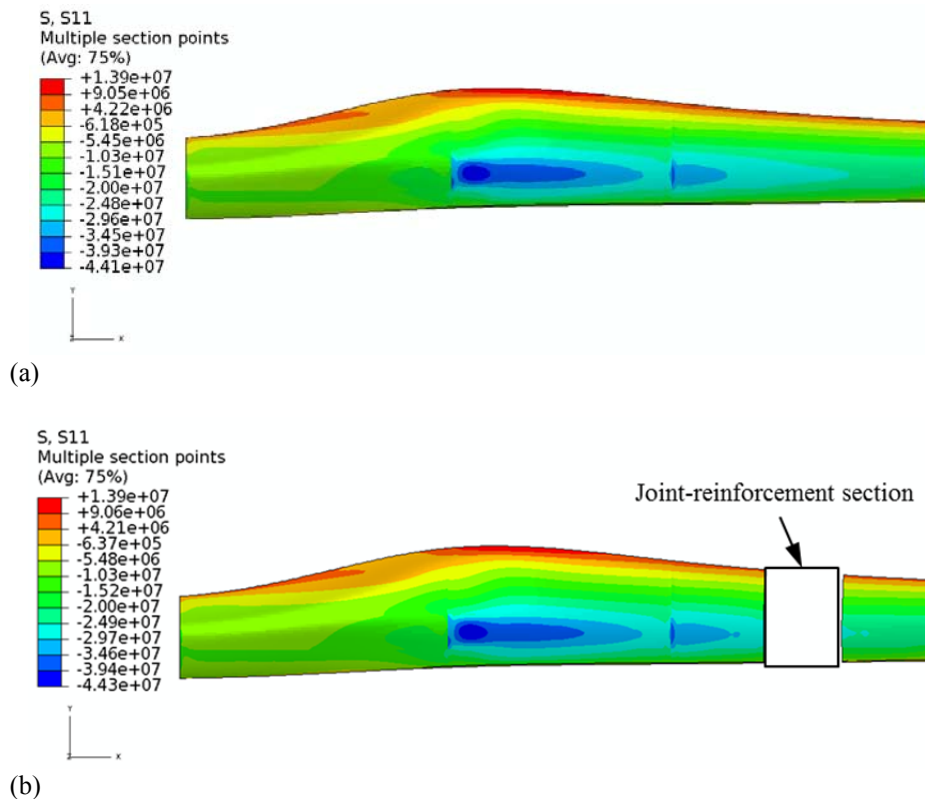


Figure 5.6. S_{11} stress in the outermost GF fabric layer in the upper blade skin ($5.6 \text{ m} < r < 46 \text{ m}$): (a) SB Model, and (b) MB Model.

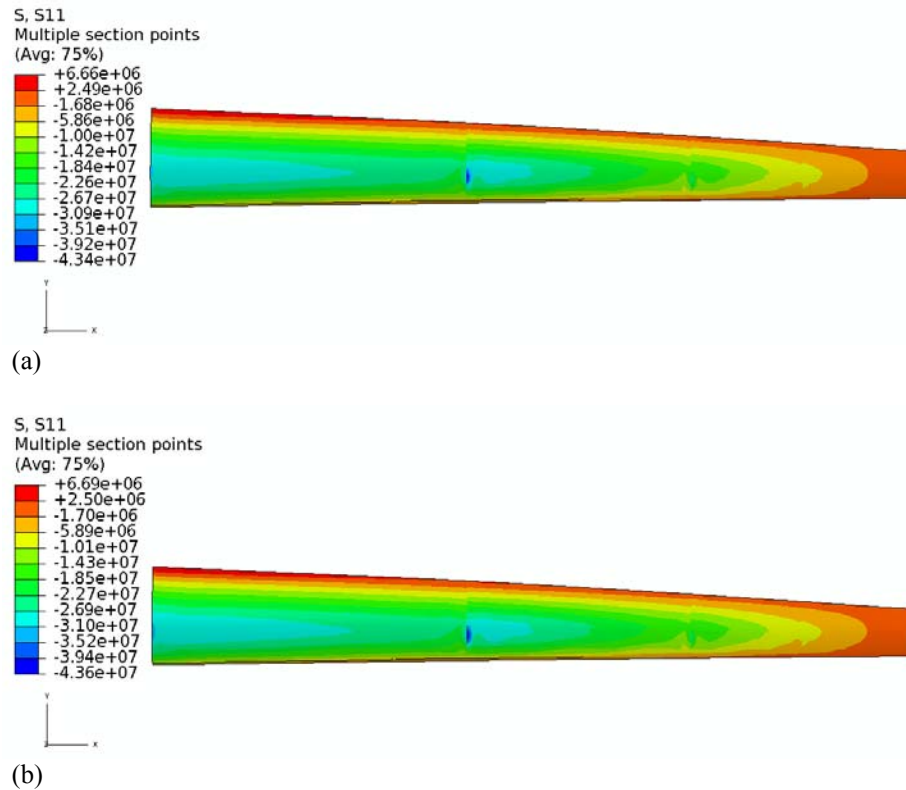


Figure 5.7. S₁₁ stress in the outermost GF fabric layer in the upper blade skin ($46 \text{ m} < r < 80 \text{ m}$): (a) SB Model, and (b) MB Model.

These values occur at the blade skin/spar cap ($20 \text{ m} < r < 32 \text{ m}$) where the corresponding reaction moment is higher, but the section modulus is lower. In both models, the stresses are much lower for the rest of the airfoil section. At any given cross-section, lower stresses are seen at the leading or trailing edges. The compressive stresses decrease along the local rotor radius toward the tip though tensile stresses are observed in the vicinity of the tip due to asymmetric blade geometry, as depicted in Figure 5.7. All the other layers experience very similar contours. Thus, it is inferred that the global stress field remains almost identical between the single blade and modular blade.

To better understand the influence of the joint-transition region on the stress distribution, S_{11} stress contours in the outermost GF fabric layer of the upper blade skin ($32 \text{ m} < r < 46$) are presented in Figure 5.8. It is noted that the reinforcement region does not induce any significant changes due to its higher stiffness of 1.5x the SB Model. On the other hand, the joint region in the MB Model undergoes compressive stresses in the range of 12.4-14.8 MPa whereas in the SB Model, this region experiences 22.2-27.1 MPa in compression. This almost 45% difference is attributed to the 3x higher stiffness of this local region in the MB model.

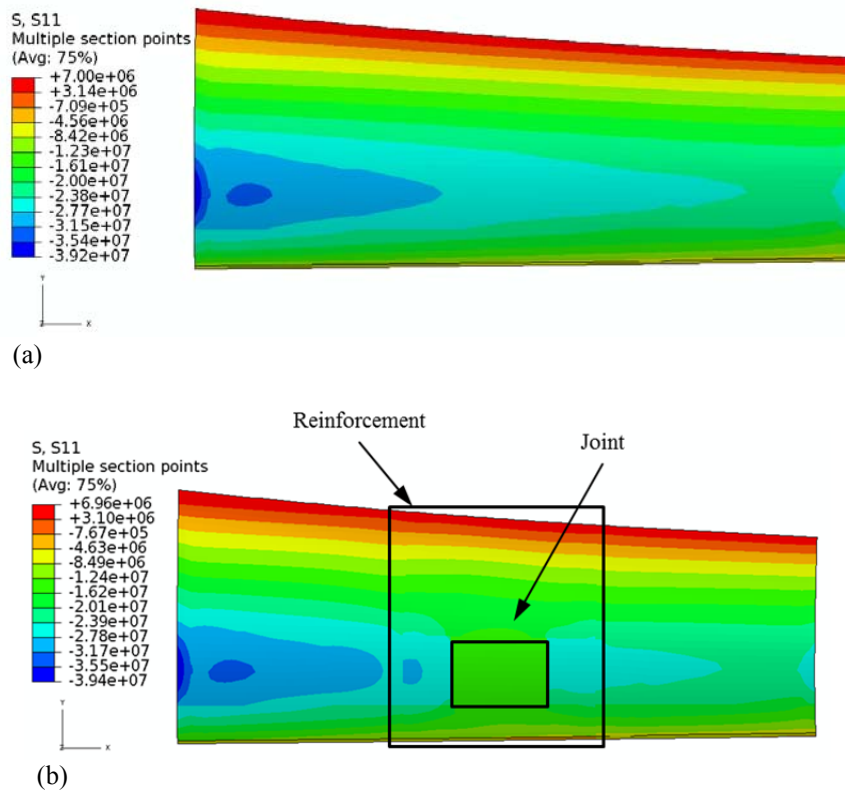


Figure 5.8. S_{11} stress in the outermost GF fabric layer in the upper blade skin ($32 \text{ m} < r < 46 \text{ m}$): (a) SB Model, and (b) MB Model.

While no damage modes are observed in GF and CF layers, the balsa core of the skin in both the SB Model and MB Model exceeds the allowable strength based on von Mises stress criteria, as seen in Figure 5.9.

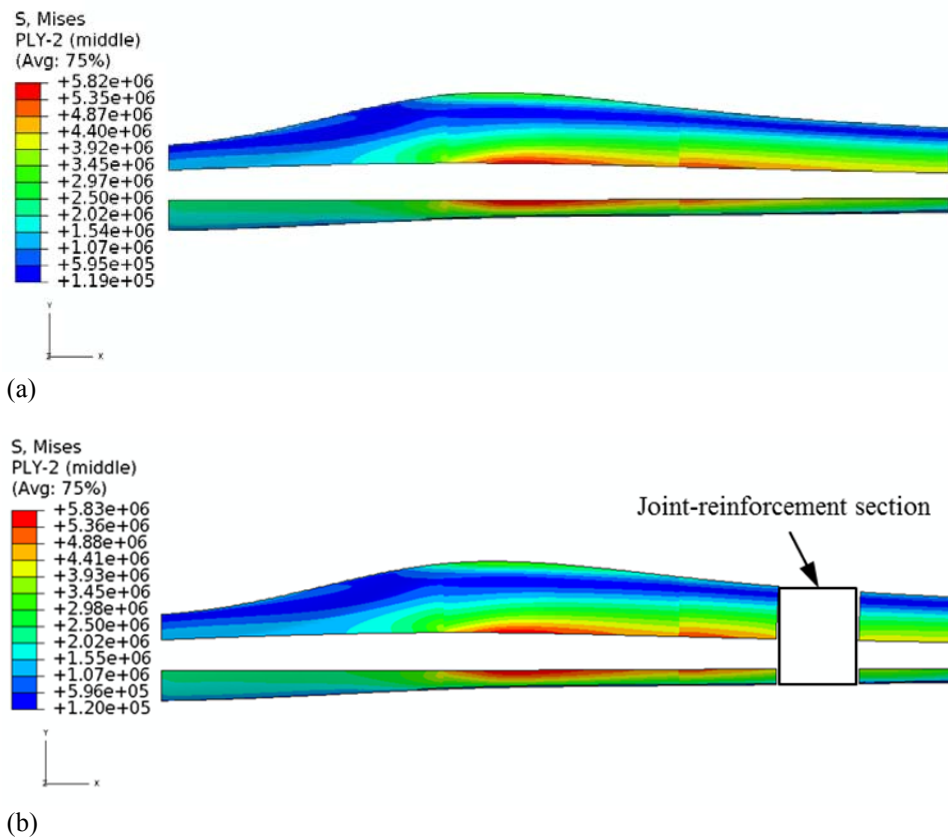


Figure 5.9. Von Mises stress in the balsa core of the upper blade skin ($5.6 \text{ m} < r < 46 \text{ m}$): (a) SB Model, and (b) MB Model.

In the SB Model, higher von Mises stresses are located at the boundary between the blade skin and the blade skin/spar cap ($20 \text{ m} < r < 32 \text{ m}$). This blade skin region has the thicker airfoil, and these dimensions affect the inertia leading to the higher stresses. The

maximum von Mises stress experienced by the balsa core of the skin is about 5.82 MPa in compression, which is above its allowable strength of 5.4 MPa. Similarly, this damage mode is also observed in the MB Model, and it is not located at all near the joint-reinforcement section but at the boundary between the blade skin and the blade skin/spar cap ($20 \text{ m} < r < 32 \text{ m}$).

5.3.4 Forces Generated by Cable Mechanisms

Since the cable mechanisms are not physically represented in the simulations, the axial loads that the simulation results will infer are calculated by utilizing the stress fields of MB Model. The axial forces are then evaluated by Equation (5.1). It is seen in Figure 5.10 that the upper and lower Joint-BS/SC regions are in compression and tension, respectively. There coexist both compressive and tensile S_{11} stresses in Joint-FSW and Joint-ASW regions. Since multiple layers are stacked for the joint region in this simulation, we look into S_{11} stress distribution through shell thickness. As an example to find the maximum S_{11} stresses, S_{11} stress distribution through shell thickness in the Joint-BS/SC region is presented in Figure 5.11. As a result, the maximum values of S_{11} stress in the lower and upper Joint-BS/SC regions are 7.16×10^7 and -6.68×10^7 N, respectively.

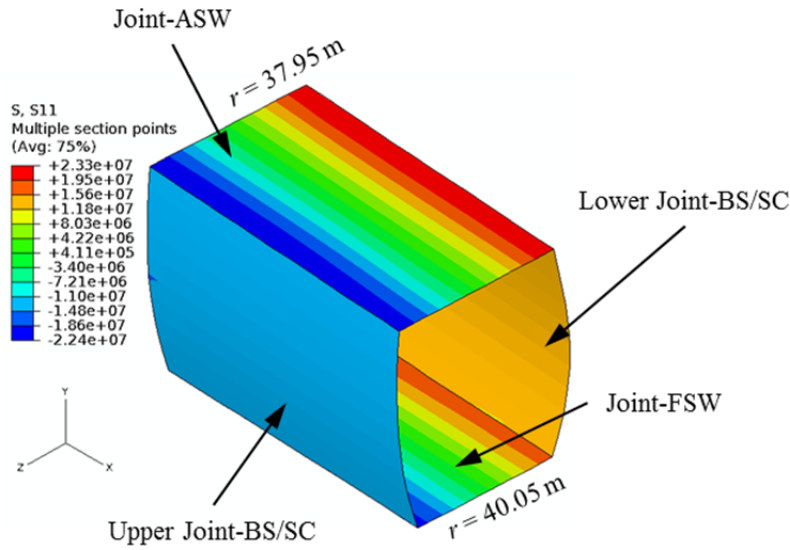


Figure 5.10. S_{11} stress contour in the outermost layer of the joint region in the MB Model.

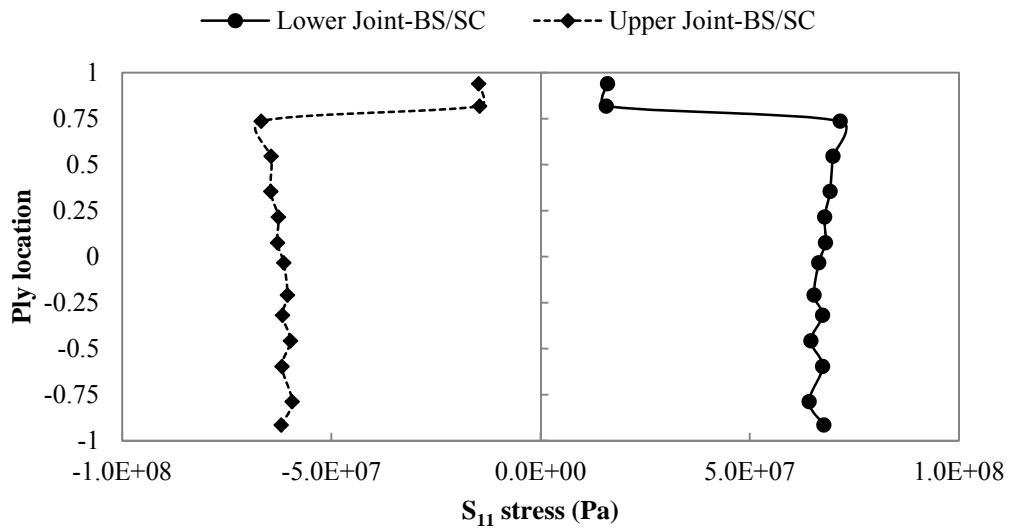


Figure 5.11. S_{11} stress distribution through shell thickness in the Joint-BS/SC region.

Table 5.5. Loads generated by cable mechanisms

Location	Max. S_{11} stress (MPa)	Cross sectional area (m^2)	Axial forces (N)
Lower Joint-BS/SC	7.16×10^7	4.87×10^{-2}	3.49×10^6
Upper Joint-BS/SC	-6.68×10^7	4.83×10^{-2}	3.23×10^6
Joint-FSW	4.00×10^7	5.55×10^{-2}	2.22×10^6
Joint-ASW	5.98×10^7	6.42×10^{-2}	3.84×10^6

The maximum S_{11} stresses, cross-sectional areas, and axial forces in the joint region are summarized in Table 5.5. Since there is an asymmetry in the blade geometries and applied loads, axial forces for cable mechanisms are imbalanced in the joint region. Since the upper Joint-BS/SC region experiences compression due to the operational loads, an additional axial force in the upper Joint-BS/SC region is not necessary to produce compression and to create a joint. The absence of the additional compressive force in the upper Joint-BS/SC region leads to non-smooth connection of two modules in the joint region. Therefore, the axial force in the upper Joint-BS/SC region should be taken into account in order to find the axial force for cable mechanisms.

The total axial force for cable mechanisms is given by the sum of four axial forces in the lower Joint-BS/SC, upper Joint-BS/SC, Joint-FSW, and Joint-ASW regions. The total axial force is 12.8×10^6 N, which is greater than the breaking strength of a commercial cable. Therefore, a single cable with larger diameter or multiple cables are required. Further detailed analysis of introducing axial cable loads to the MB Model for prior to its rotation can be followed in the APPENDIX F. It will be confirmed that

the total axial force for cable mechanisms produces enough compressive forces in the overlapping region to create the joint region in the MB Model.

5.3.5 Natural Frequency Results

The undamped natural frequencies of the non-rotating blade, lowest to the sixth, are presented in Table 5.6. The difference in natural frequencies among the SB Model, MB Model, and MB-IW is at most 1.6%. Since the SB Model shows pure mode shapes in the lower natural frequency, there is no coupling mode of bending and twist together. Similarly, pure mode shapes of the MB Model and MB-IW Model are obtained in this lower frequency range. Therefore, locally increasing stiffness and/or density in the blade does not lead to notable changes in natural frequencies and mode shapes.

Table 5.6. Undamped natural frequencies in Hz

Mode	SB Model	MB Model	MB-IW Model
1st flapping	0.607	0.617	0.616
2nd flapping	1.82	1.83	1.82
3rd flapping	3.84	3.90	3.88
1st edge	0.975	0.983	0.980
2nd edge	3.16	3.21	3.19
1st torsional	4.96	5.01	4.98

5.4 Discussion

The introduction of the joint concept to create a modular blade did not adversely affect the mechanical and frequency response in comparison to the single length blade performance. The joint and reinforcement section corresponded to 5.5% of the blade length where both stiffness and density variations were examined to assess the sensitivity to displacement, stress, and frequency responses. Cable mechanisms experienced the axial force of $12.8 \times 10^6 \text{ N}$ to form the joint region of the modular blade. Since this magnitude was much greater than the breaking strength of a commercial cable ($1.2 \times 10^6 \text{ N}$ - $1.9 \times 10^6 \text{ N}$), a single cable with larger diameter or multiple cables could be integrated into cable mechanisms.

Furthermore, the total mass contribution of the cables was calculated assuming a safety factor of 1 for the commercial cables in Table 5.1 and that they extended from the blade root to the tip. The number of cables was simply settled by rounding up the required axial force over breaking strength of a cable. The unit mass for all cables was found from unit mass of a cable multiplied by the number of cables. The total mass of all cables that extended from the blade root to the tip was defined by unit mass for all cables times the blade length. These are summarized in Table 5.7 illustrating that the additional mass of the stainless cables is in the range of 7.36 - 7.71 tons. On the other hand, the mass of eleven CFCCs was 1.28 tons that corresponded to almost one-sixth of the total mass for the stainless cables. However, these values were still considered relatively heavy in comparison with the mass of the 80 m blade. Certainly at the detailed design

phase considerations, the cable length and locations can be optimized to replace the present simple calculations.

Table 5.7. Additional mass to the blade due to stainless cables and CFCCs

	Diameter (m)	# of cables	Unit mass for all cables (kg/m)	Total mass (tons)
Stainless cables [95]	0.04	15	96.9	7.36
	0.06	7	102	7.71
CFCCs [97]	0.04	11	16.8	1.28

6. CONCLUSIONS

The 80 m single continuous blade was studied to understand potential damage mechanisms when subjected to aerodynamic as well as impact loads. The blade geometry, material selection, and layup were carefully designed to reduce total weight. In order to simplify manufacturing, transportation, and assembly requirements, a conceptual joint was proposed to create a modular two section blade that performed as well as the single blade. The overall results indicated that such a design is feasible and will sustain operating loads just as well. Herein we highlight the salient knowledge gained from the computational assessments undertaken.

Single blade studies revealed that balsa core vs. foam core led to different damage initiation modes. Specifically at $u_w = 8.9$ m/s, balsa core exceeded its allowable whereas the blade with foam core experienced damage to $+45^\circ/-45^\circ$ UD-GF layer of its shear web. Additionally, warping was observed in the upper skin/spar cap ($60 \text{ m} < r < 75 \text{ m}$) of both blades with balsa and foam cores. This phenomenon depicted the dependence on the taper blade with non-uniform airfoil cross-sectional shapes, as well as laminate hybridization. The S_{11} stress ratio of the face to the core in the sandwich skin of the blade with foam core was much higher than the other model. Consequently, the single continuous blade provided sufficient damage tolerance below the loads associated with $u_w = 8.9$ m/s. The replacement of a core material is recommended to improve its structural response. Thus, a soft material with relatively low elastic properties should be taken as a core material.

The 2kg-bird direct and oblique impact study on a blade with and without preloads clearly demonstrated that the more realistic condition of preloads offered the better impact resistance. In the cases without preloads, balsa core was damaged at the impact site. While the direct impact configuration effectively reduced the transfer of impact forces to the blade, the oblique impact forces were dissipated on the impact site where tensile damage/failure mode was observed. The blade with preloads survived the realistic bird impact event without incurring any damage in the composite layers and the balsa core.

The proposed joint concept for two modular blades to create a full length blade by introducing a joint-transition region did not adversely affect the mechanical and frequency response in comparison to the structural performance of the single continuous blade. The joint-reinforcement section corresponded to 5.5% of the blade length where both stiffness and density variations were examined to assess the sensitivity to displacement, stress, and frequency responses. It is concluded that the proposed modular composite blade configuration with the cable mechanism is a feasible concept and can be easily adopted in future modular blade designs.

REFERENCES

- [1] U.S. Energy Information Administration. International energy outlook 2011. [http://www.eia.gov/forecasts/ieo/pdf/0484\(2011\).pdf](http://www.eia.gov/forecasts/ieo/pdf/0484(2011).pdf). Accessed 9 October 2011.
- [2] Energy Efficiency and Renewable. 20% wind energy by 2030: increasing wind energy's contribution to U.S. electricity supply. Washington, DC: U.S. Department of Energy, 2008:DOE/GO-102008-2567.
- [3] Burton T, Jenkins N, Sharpe D, Bossanyi E. Wind energy handbook. New York, NY: Wiley, 2011.
- [4] Archer CL, Jacobson MZ. Evaluation of global wind power. Journal of Geophysical Research;110(D12):D12110.
- [5] Investigation Committee on the Accident at the Fukushima Nuclear Power Stations of Tokyo Electric Power Company. Final report on the accident at the Fukushima Nuclear Power Stations of Tokyo Electric Power Company. Tokyo: Japan Atomic Energy Agency, 2012.
- [6] Djairam D. The electrostatic wind energy converter: electrical performance of a high voltage prototype, Doctoral dissertation. Delft: Delft University of Technology, 2008.
- [7] Djairam D, Hubacz AN, Morshuis PHF, Marijnisen JCM, Smit JJ. The development of an electrostatic wind energy converter (EWICON). In: Proceedings of 2005 International Conference on Future Power Systems, Amsterdam, 16-18 November 2005. p. 474-477.
- [8] Djairam D, Morshuis PHF, Smit JJ. Optimising electrode design and positioning for EHDA produced particles in a EWICON. In: Proceedings of Conference on Electrical Insulation and Dielectric Phenomena, Vancouver, 14-17 October 2007. p. 478-481.
- [9] Betz A. Introduction to the theory of flow machines. New York, NY: Pergamon Press, 1966.
- [10] Eggleston DM, Stoddard FS. Wind turbine engineering design. New York, NY: Van Nostrand Reinhold Company, 1987.
- [11] Enercon GmbH. Windblatt Enercon magazine for wind energy, Issue 01/2010. Aurich: Enercon GmbH, 2010.

- [12] Gamesa Corporación Tecnológica. Gamesa 4.5 MW platform catalogue. <http://www.gamesacorp.com/recursos/doc/productos-servicios/aerogeneradores/catalogo-g10x-45mw-eng.pdf>. Accessed 28 May 2013.
- [13] Siemens AG. Technical specification on wind turbine SWT-4.0-130. <http://www.energy.siemens.com/us/en/renewable-energy/wind-power/platforms/g4-platform/wind-turbine-swt-4-0-130.htm#content=Technical%20Specification>. Accessed 12 March 2014.
- [14] GE Energy. GE's 2.75-120 wind turbine. http://www.ge-energy.com/products_and_services/products/wind_turbines/ge_2.75_120_wind_turbine.jsp. Accessed 12 March 2014.
- [15] Vestas Wind Systems A/S. A joint venture for global leadership in offshore wind. http://vestas.com/en/products_and_services/offshore#!. Accessed 22 April 2014.
- [16] Ashwill TD, Laird DL. Concepts to facilitate very large blades. In: Proceedings of 2007 ASME/AIAA Wind Energy Symposium, Reno, 8-11 January 2007. p. AIAA 2007-2817.
- [17] Brondsted P, Lilholt H, Lystrup A. Composite materials for wind power turbine blades. *Annual Review of Materials Research*;35:505-538.
- [18] Griffin DA. WindPACT turbine design scaling studies technical area 1: composite blades for 80-to 120-meter rotor. Golden, CO: National Renewable Energy Laboratory, 2001:NREL/SR-500-29492.
- [19] Eyb E. Modular rotor blade for a wind turbine and method for assembling same. Washington, DC: U.S. Patent and Trademark Office, 2010:US 7,654,799 B2.
- [20] Glenn B, Dehlsen JGP, Keller W, Rohm A, Mehrle W, Stuckert M. A modular rotor blade for a power-generating turbine and a method for assembling a power-generating turbine with modular rotor blades. Geneva: World Intellectual Property Organization, 2009:WO 2009/090537 A2.
- [21] Stam R, Starke A, Veldkamp B, Meyer J. Blade modular, a modular rotor blade and a method for assembling a modular rotor blade. Washington, DC: U.S. Patent and Trademark Office, 2010:US 2010/0158694 A1.
- [22] Berry DS, Berg D. Blade system design studies phase II: final project report. Albuquerque, NM: Sandia National Laboratories, 2008:SAND2008-4648.
- [23] Fuglsang P, Bak C. Development of the Risø wind turbine airfoils. *Wind Energy*;7(2):145-162.

- [24] Somers D. The S816, S817, and S818 airfoils. Golden, CO: National Renewable Energy Laboratory, 2004:NREL/SR-500-36333.
- [25] Tangler JL, Somers DM. NREL airfoil families for HAWTs. In: Proceedings of AWEA Windpower '95 Conference, Washington, 27-30 March 1995. p. 117-123.
- [26] Timmer WA, van Rooij R. Summary of the Delft university wind turbine dedicated airfoils. *Journal of Solar Energy Engineering*;125(4):488-496.
- [27] Bak C, Fuglsang P, Sørensen NN, Madsen HA, Shen WZ, Sørensen JN. Airfoil characteristics for wind turbines. Roskilde: Riso National Laboratory, 1999:Riso-R-1065(EN).
- [28] Thomsen OT. Sandwich materials for wind turbine blades - present and future. *Journal of Sandwich Structures and Materials*;11(1):7-26.
- [29] Hau E. Wind turbines: fundamentals, technologies, application, economics. 2nd ed. New York, NY: Springer-Verlag, 2006.
- [30] De Goeij WC, Van Tooren MJL, Beukers A. Implementation of bending-torsion coupling in the design of a wind-turbine rotor-blade. *Applied Energy*;63(3):191-207.
- [31] Todoroki A, Kawakami Y. Optimal design of wind turbine blade of CF/GF hybrid composites. *Transactions of the Japan Society for Computational Engineering and Science*;2008(2008):20080012 [in Japanese].
- [32] Mohamed MH, Wetzel KK. 3D woven carbon/glass hybrid spar cap for wind turbine rotor blade. *Journal of Solar Energy Engineering*;128(4):562-573.
- [33] Griffin DA. Blade system design studies volume I: composite technologies for large wind turbine blades. Albuquerque, NM: Sandia National Laboratories, 2002:SAND2002-1879.
- [34] Griffin DA. Blade system design studies volume II: preliminary blade designs and recommended test matrix. Albuquerque, NM: Sandia National Laboratories, 2004:SAND2004-0073.
- [35] Cairns DS, Riddle T, Nelson J. Wind turbine composite blade manufacturing: The need for understanding defect origins, prevalence, implications and reliability. Albuquerque, NM: Sandia National Laboratories, 2011:SAND2011-1004.
- [36] Brøndsted P, Nijssen R. Advances in wind turbine blade design and materials. Philadelphia, PA: Woodhead Publishing, 2013.

- [37] Li L. Structural design of composite rotor blades with consideration of manufacturability, durability, and manufacturing uncertainties, Doctoral dissertation. Atlanta, GA: Georgia Institute of Technology, 2008.
- [38] Bechly ME, Clausen PD. Structural design of a composite wind turbine blade using finite element analysis. *Computers & Structures*;63(3):639-646.
- [39] Park J-K, Park J-S, Lee H-G, Lee S-H. Numerical simulation on fatigue test of composite rotor blade for multi-megawatt wind turbine. In: Proceedings of the 18th international conference on composite materials (ICCM18), Jeju, 21-26 August 2011. p. P2-39-IK1348.
- [40] Epps BP, Kimball RW. Unified rotor lifting line theory. *Journal of Ship Research*;57(4):181-201.
- [41] Hansen MH. Aeroelastic instability problems for wind turbines. *Wind Energy*;10(6):551-577.
- [42] Berring P, Branner K, Berggreen C, Knudsen HW. Torsional performance of wind turbine blades-part I: experimental investigation. In: Proceedings of the 16th International Conference on Composite Materials (ICCM16), Kyoto, 8-13 July 2007. p. 1118.
- [43] Berring P, Branner K, Berggreen C, Knudsen HW. Torsional performance of wind turbine blades-part II: numerical validation. In: Proceedings of the 16th International Conference on Composite Materials (ICCM16), Kyoto, 8-13 July 2007. p. 1432.
- [44] Laird DL, Montoya FC, Malcolm DJ. Finite element modeling of wind turbine blades. In: Proceedings of AIAA/ASME Wind Energy Symposium, Reno, 10-13 January 2005. p. 9-15.
- [45] Jureczko M, Pawlak M, Mezyk A. Optimisation of wind turbine blades. *Journal of Materials Processing Technology*;167(2-3):463-471.
- [46] Georgiadis S, Gunnion AJ, Thomson RS, Cartwright BK. Bird-strike simulation for certification of the Boeing 787 composite moveable trailing edge. *Composite Structures*;86(1-3):258-268.
- [47] Shmotin Y, Chupin P, Gabov D, Ryabov A, Romanov V, Kukanov S, et al. Bird strike analysis of aircraft engine fan. In: Proceedings of the 7th European LS-DYNA Conference, Salzburg, 14-15 May 2009. p. H-I-03.
- [48] Johnson AF, Holzapfel M. Modelling soft body impact on composite structures. *Composite Structures*;61(1-2):103-113.

- [49] Heimbs S. Computational methods for bird strike simulations: a review. *Computers & Structures*;89(23-24):2093-2112.
- [50] Heimbs S. Bird strike simulations on composite aircraft structures. In: *Proceedings of 2011 SIMULIA Customer Conference, Barcelona, 16-19 May 2011*. p. 73-86.
- [51] Smojver I, Ivancevic D. Bird strike damage analysis in aircraft structures using Abaqus/Explicit and coupled Eulerian Lagrangian approach. *Composite Science and Technology*;71(4):489-498.
- [52] Dahlroth D. Load cases for medium-sized wind power plants. In: *Proceedings of Structural Design Criteria for LS WECS, Greenford, 7-8 March 1983*. p. 121-193.
- [53] Wilbeck JS. Impact behavior of low strength projectiles, Doctoral dissertation. College Station, TX: Texas A&M University, 1977.
- [54] Airoidi A, Cacchione B. Modelling of impact forces and pressures in Lagrangian bird strike analyses. *International Journal of Impact Engineering*;32(10):1651-1677.
- [55] McCallum S, Constantinou C. The influence of bird-shape in bird-strike analysis. In: *Proceedings of the 5th European LS-DYNA Users Conference, Birmingham, 25-26 May 2005*. p. 2c-77.
- [56] Castelletti LML, Anghileri M. Multiple birdstrike analysis - a survey of feasible techniques. In: *Proceedings of the 30th European Rotorcraft Forum, Marseilles, 14-16 September 2003*. p. 495-505.
- [57] Lammen W, Van Houten R. Predictive simulation of impact phenomena for innovations in aircraft component design. In: *Proceedings of the 6th EUROMECH Nonlinear Dynamics Conference, Saint-Petersburg, 30 June - 4 July 2008*.
- [58] Roth - Johnson P, Wirz RE. Aero - structural investigation of biplane wind turbine blades. *Wind Energy*;17(3):397-411.
- [59] Berggreen C, Jensen C, Hayman B. Buckling strength of square composite plates with geometrical imperfections: Preliminary results. In: *Proceedings of the 1st MARSTRUCT International Conference, Glasgow, 12-14 March 2007*. p. 413-420.
- [60] Berggreen C, Tsouvalis N, Hayman B, Branner K. Buckling strength of thick composite panels in wind turbine blades-part I: effect of geometrical imperfections. In: *Proceedings of the 4th International Conference on Composites Testing and Model Identification, Dayton, 20-24 October 2008*.

- [61] Branner K, Berring P, Berggreen C. Buckling strength of thick composite panels in wind turbine blades-part II: effect of delaminations. In: Proceedings of the 4th International Conference on Composites Testing and Model Identification, Dayton, 20-24 October 2008.
- [62] Jensen FM, Falzon BG, Ankersen J, Stang H. Structural testing and numerical simulation of a 34m composite wind turbine blade. *Composite Structures*;76(1):52-61.
- [63] Chortis DI, Chrysochoidis NA, Saravanos DA. Damped structural dynamics models of large wind-turbine blades including material and structural damping. *Journal of Physics*;75(1):012076.
- [64] Kim DH, Kim YH, Kim SH. Performance analyses of 10MW composite wind turbine blade considering aeroelastic effects. In: Proceedings of the 18th international conference on composite materials (ICCM18), Jeju, 21-26 August 2011. p. W21-23-IK1756.
- [65] Kim T, Branner K, Hansen AM. Developing anisotropic beam element for design of composite wind turbine blades. In: Proceedings of the 18th International Conference on Composite Materials (ICCM18), Jeju, 21-26 August 2011. p. P3-73-IF1500.
- [66] Chou J-S, Chiu C-K, Huang I-K, Chi K-N. Failure analysis of wind turbine blade under critical wind loads. *Engineering Failure Analysis*;27:99-118.
- [67] Hua Y, Kasavajhala ARM, Gu L. Elastic-plastic analysis and strength evaluation of adhesive joints in wind turbine blades. *Composites Part B*;44(1):650-656.
- [68] Griffith DT, Ashwill TD. The sandia 100-meter all-glass baseline wind turbine blade: SNL100-00. Albuquerque, NM: Sandia National Laboratories, 2011:SAND2011-3779.
- [69] Griffith DT, Resor BR. Description of model data for SNL13.2-00-Land: A 13.2 MW land-based turbine model with SNL100-00 Blades. Albuquerque, NM: Sandia National Laboratories, 2011:SAND2011-9310P.
- [70] Nanami N. Vibration and structural response of hybrid wind turbine blades, Master's thesis. College Station, TX: Texas A&M University, 2010.
- [71] Nanami N, Ochoa OO. Assessment of a modular composite wind turbine blade. In: Proceedings of the American Society for Composites 26th Annual Technical Conference, Montreal, 26-28 September 2011. p. 1133.
- [72] Nanami N, Ochoa OO. Vibration and dynamic response of hybrid wind turbine blades. In: Liu D, editor. *Dynamic effects in composites materials*, Vol. 1. Lancaster: DEStech Publications; 2012. p. 289-301.

- [73] Nanami N, Ochoa OO. Computational assessment of bird strike on hybrid composite wind turbine blade. In: Proceedings of the American Society for Composites 27th Annual Technical Conference, Arlington, 1-3 October 2012. p. 245.
- [74] National Research Council. Environmental impacts of wind-energy projects. Washington, DC: The National Academies Press, 2007.
- [75] Marris E, Fairless D. Wind farms' deadly reputation hard to shift. *Nature*;447(7141):126.
- [76] Sovacool BK. The avian benefits of wind energy: a 2009 update. *Renewable Energy*;49:19-24.
- [77] Dolbeer RA, Wright SE, Weller J, Begier MJ. Wildlife strikes to civil aircraft in the United States 1990–2011. Washington, DC: U.S. Department of Transportation, Federal Aviation Administration, Office of Airport Safety and Standards, 2012:Serial report No. 17.
- [78] Hughes TJ. The finite element method: linear static and dynamic finite element analysis. New Jersey, NJ: Prentice-Hall, 1987.
- [79] Abaqus Inc. ABAQUS documentation collection, Version 6.12. Pawtucket, RI: Abaqus Inc., 2012.
- [80] Reddy JN. An introduction to the finite element method. 3rd ed. New York, NY: McGraw-Hill, 2006.
- [81] Benson DJ. Computational methods in Lagrangian and Eulerian hydrocodes. *Computer Methods in Applied Mechanics and Engineering*;99(2-3):235-394.
- [82] Benson DJ, Okazawa S. Contact in a multi-material Eulerian finite element formulation. *Computer Methods in Applied Mechanics and Engineering*;193(39-41):4277-4298.
- [83] Hibbeler RC. Mechanics of materials. 3rd ed. New Jersey, NJ: Prentice-Hall, 1997.
- [84] Hashin Z. Failure criteria for unidirectional fiber composites. *Journal of Applied Mechanics*;47(2):329-334.
- [85] Hashin Z, Rotem A. A fatigue failure criterion for fiber reinforced materials. *Journal of Composite Materials*;7(4):448-464.
- [86] Lapczyk I, Hurtado JA. Progressive damage modeling in fiber-reinforced materials. *Composites Part A*;38(11):2333-2341.

- [87] Vural M, Ravichandran G. Microstructural aspects and modeling of failure in naturally occurring porous composites. *Mechanics of Materials*;35(3-6):523-536.
- [88] DIAB. Divinycell H technical data.
<http://www.diabgroup.com/~media/Files/Products/Core-material-pdf/H%20July%202013%20rev10%20SI.pdf>. Accessed 9 January 2014.
- [89] Kyriazoglou C, Guild FJ. Finite element prediction of damping of composite GFRP and CFRP laminates: a hybrid formulation-vibration damping experiments and Rayleigh damping. *Composite Science and Technology*;66(3-4):487-498.
- [90] MatWeb. Greene tweed orthetek WF polyketone, continuous woven carbon fiber, Database of material properties.
<http://www.matweb.com/search/QuickText.aspx?SearchText=woven%20carbon>. Accessed 12 January 2010.
- [91] Daniel MD, Ishai O. *Engineering mechanics of composite materials*. New York, NY: Oxford University Press, 1994.
- [92] Liu J, Li YL, Xu F. The numerical simulation of a bird-impact on an aircraft windshield by using the SPH method. *Advanced Materials Research*;33:851-856.
- [93] Zhang YK, Li YL. Analysis of the anti-bird impact performance of typical beam-edge structure based on ANSYS/LS-DYNA. *Advanced Materials Research*;33-37:395-400.
- [94] Worldwide Enterprises Inc. Galvanized and stainless aircraft cable.
<http://www.wwirerope.com/aircraftcable/>. Accessed 13 May 2013.
- [95] Tokyo Rope MFG. TSK stainless ropes.
http://saas.startialab.com/acti_books/1045176105/5240/SWF_Window.html. Accessed 17 April 2014.
- [96] eMaterialHandling.com. Stainless steel cable.
http://www.ematerialhandling.com/materialhandling/stainless_steel/cable/stainless_steel_cable.htm. Accessed 13 May 2013.
- [97] Tokyo Rope MFG. Carbon fiber composite cable.
<http://www.tokyoropeco.jp/product/cfcc/material/index.html>. Accessed 17 April 2014.
- [98] Meier U. Carbon fiber-reinforced polymers: modern materials in bridge engineering. *Structural Engineering International*;2(1):7-12.

APPENDIX A

Mindlin shell theory forms the relaxation of the Kirchhoff constraints: a transverse normal plane rotates with angles (ϕ_x) about the y-axis as shown in Figure A.1. [80]. Bending strain tensors are given in Equation (A.1), and the governing equations for Mindlin shell theory are expressed in Equations (A.2)-(A.4).

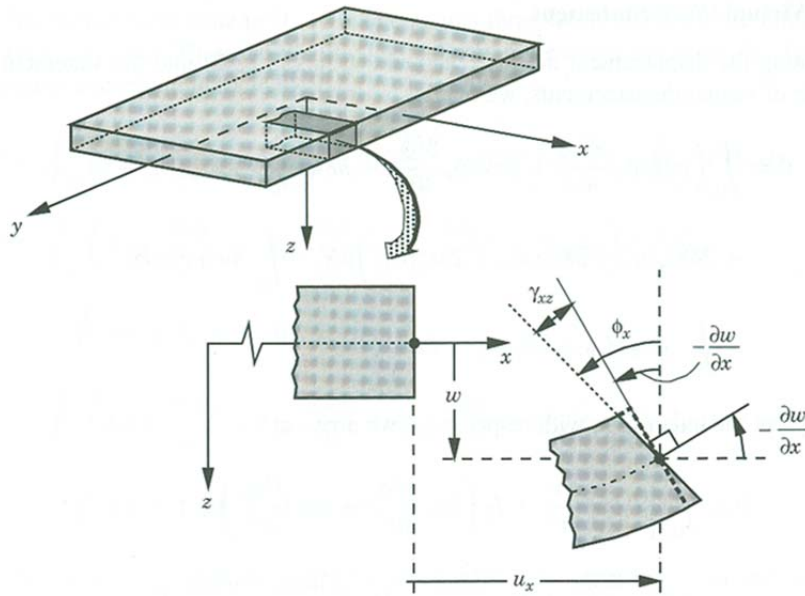


Figure A.1. Kinematics of Mindlin shell theory [80].

$$\begin{Bmatrix} \varepsilon_{xx} \\ \varepsilon_{yy} \\ 2\gamma_{xy} \\ 2\gamma_{xz} \\ 2\gamma_{yz} \end{Bmatrix} = z \begin{Bmatrix} \frac{\partial \phi_x}{\partial x} \\ \frac{\partial \phi_y}{\partial y} \\ \left(\frac{\partial \phi_x}{\partial y} + \frac{\partial \phi_y}{\partial x} \right) \\ \phi_x + \frac{\partial w}{\partial x} \\ \phi_y + \frac{\partial w}{\partial y} \end{Bmatrix} \quad (\text{A.1})$$

where w is the displacement on the mid-plane in the z -axis, ϕ_x and ϕ_y , the rotation of the transverse normal plane about the y -axis and the x -axis, respectively.

$$\frac{\partial Q_x}{\partial x} + \frac{\partial Q_y}{\partial y} + q = I_0 \frac{\partial^2 w}{\partial t^2} \quad (\text{A.2})$$

$$\frac{\partial M_{xx}}{\partial x} + \frac{\partial M_{xy}}{\partial y} - Q_x = I_2 \frac{\partial^2 \phi_x}{\partial t^2} \quad (\text{A.3})$$

$$\frac{\partial M_{xy}}{\partial x} + \frac{\partial M_{yy}}{\partial y} - Q_y = I_2 \frac{\partial^2 \phi_y}{\partial t^2} \quad (\text{A.4})$$

Similarly, the normality assumption may be relaxed in Timoshenko beam theory, and the kinematics of this theory are presented in Figure A.2 [80]. While the equilibrium equations of the Euler-Bernoulli beam are basically maintained in Timoshenko beam theory, a beam involving shear deformations has to be kinematically constrained. The

governing equations for Timoshenko beams are given in Equations (A.5) and (A.6), which are coupled, partial differential equations for two variables, the out-of-plane deflection (w) and rotation about the y -axis (Ψ).

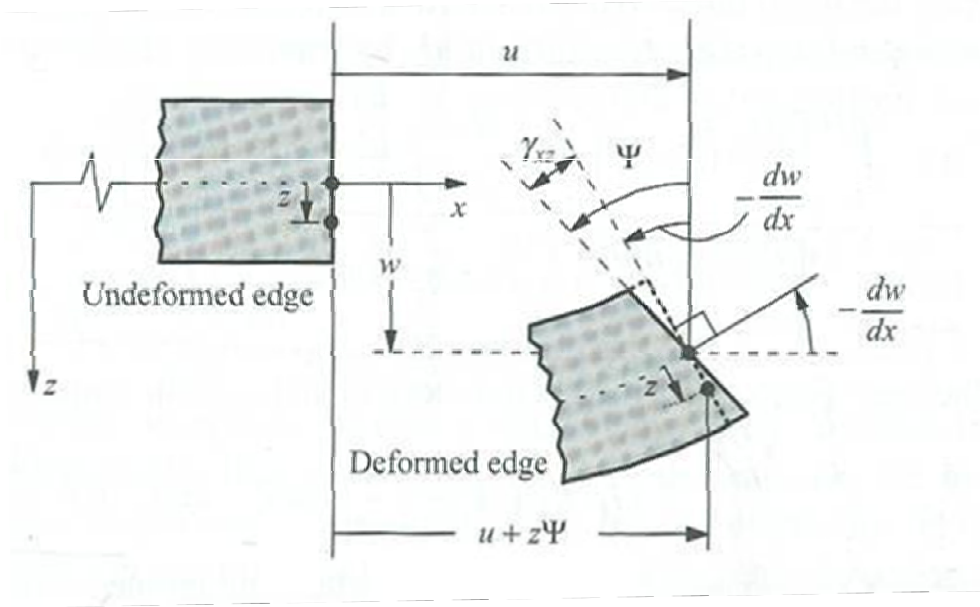


Figure A.2. Kinematics of Timoshenko beams [80].

$$-\frac{d}{dx} \left[GAK_{sc} \left(\Psi + \frac{dw}{dx} \right) \right] + c_f(x)w = q(x) \quad (\text{A.5})$$

and

$$-\frac{d}{dx} \left(E(x)I(x) \frac{d\Psi}{dx} \right) + GAK_{sc} \left(\Psi + \frac{dw}{dx} \right) = 0 \quad (\text{A.6})$$

where G denotes shear modulus; $E(x)$, Young's modulus; $I(x)$, the 2nd moment of inertia; A , the cross-sectional area; $q(x)$, the distributed transverse load; $c_f(x)$, the elastic foundation modulus; K_{sc} , the shear correction coefficient.

APPENDIX B

For in-plane stress problems, four different damage initiation mechanisms of Hashin's theory are presented as follows:

If $\hat{\sigma}_{11} \geq 0$, fiber tensile damage initiation:

$$\left(\frac{\hat{\sigma}_{11}}{X_T}\right)^2 + \alpha_c \left(\frac{\hat{\tau}_{12}}{S_L}\right)^2 \geq 1 \quad (\text{B.1})$$

If $\hat{\sigma}_{11} < 0$, fiber compressive damage initiation:

$$\left(\frac{\hat{\sigma}_{11}}{X_C}\right)^2 \geq 1 \quad (\text{B.2})$$

If $\hat{\sigma}_{22} \geq 0$, matrix tensile damage initiation:

$$\left(\frac{\hat{\sigma}_{22}}{Y_T}\right)^2 + \left(\frac{\hat{\tau}_{12}}{S_L}\right)^2 \geq 1 \quad (\text{B.3})$$

If $\hat{\sigma}_{22} < 0$, matrix compressive damage initiation:

$$\left(\frac{\hat{\sigma}_{22}}{2S_T}\right)^2 + \left[\left(\frac{Y_C}{2S_T}\right)^2 - 1\right] \frac{\hat{\sigma}_{22}}{Y_C} + \left(\frac{\hat{\tau}_{12}}{S_L}\right)^2 \geq 1 \quad (\text{B.4})$$

In the above equations, X_T denotes the longitudinal tensile strength; X_C , the longitudinal compressive strength; Y_T , the transverse tensile strength; Y_C , the transverse compressive strength; S_L , the longitudinal shear strength; S_T , the transverse shear strength; α_c , a coefficient to determine the contribution of the shear stress to the fiber tensile damage mode. The fiber tensile damage mode can be specified by using either the proposed model by setting $\alpha_c = 0$ and $S_T = Y_C / 2$ or the model with $\alpha_c = 1$ [84, 85].

APPENDIX C

Equivalent displacement, δ_{eq} , and stress, σ_{eq} , for each of the four damage modes are defined as follows [79]:

If $\hat{\sigma}_{11} \geq 0$, fiber tensile damage mode:

$$\delta_{eq}^{ft} = L^c \sqrt{\langle \varepsilon_{11} \rangle^2 + \alpha \varepsilon_{11}^2} \quad (C.1a)$$

$$\sigma_{eq}^{ft} = \frac{\langle \sigma_{11} \rangle \langle \varepsilon_{11} \rangle + \alpha \tau_{12} \varepsilon_{12}}{\delta_{eq}^{ft} / L^c} \quad (C.1b)$$

If $\hat{\sigma}_{11} < 0$, fiber compressive damage mode:

$$\delta_{eq}^{fc} = L^c \langle -\varepsilon_{11} \rangle \quad (C.2a)$$

$$\sigma_{eq}^{fc} = \frac{\langle -\sigma_{11} \rangle \langle -\varepsilon_{11} \rangle}{\delta_{eq}^{fc} / L^c} \quad (C.2b)$$

If $\hat{\sigma}_{22} \geq 0$, matrix tensile damage mode:

$$\delta_{eq}^{mt} = L^c \sqrt{\langle \varepsilon_{22} \rangle^2 + \varepsilon_{12}^2} \quad (C.3a)$$

$$\sigma_{eq}^{mt} = \frac{\langle \sigma_{22} \rangle \langle \varepsilon_{22} \rangle + \tau_{12} \varepsilon_{12}}{\delta_{eq}^{mt} / L^c} \quad (C.3b)$$

If $\hat{\sigma}_{22} < 0$, matrix compressive damage mode:

$$\delta_{eq}^{mc} = L^c \sqrt{\langle -\varepsilon_{22} \rangle^2 + \varepsilon_{12}^2} \quad (\text{C.4a})$$

$$\sigma_{eq}^{mc} = \frac{\langle -\sigma_{22} \rangle \langle -\varepsilon_{22} \rangle + \tau_{12} \varepsilon_{12}}{\delta_{eq}^{mc} / L^c} \quad (\text{C.4b})$$

where $\varepsilon_{11}, \varepsilon_{22}, \varepsilon_{12}$ are the components of the in-plane nominal strain tensor. The symbol

$\langle \rangle$ in the equations above represents the Macaulay bracket operator that is defined as

$$\langle \beta \rangle = (\beta + |\beta|) / 2 \quad (\text{C.5})$$

where β is a real number.

APPENDIX D

To make sure if no damage in the single continuous blade is caused by its own weight, the blade being subjected to gravitational loads is analyzed. It is considered that the blade is horizontally positioned with feathering condition since the moment due to gravity reaches the maximum value. The gravitational acceleration of 9.81 m/s is assigned for the blade along the Z-axis while the blade root is fully constrained. Note that the single continuous blade with the balsa core is employed in this analysis.

Tip displacements for the selected nodes of the upper and lower surfaces due to the blade's weight are presented in Figure D.1. Since the upper and lower surfaces deform for the same amount of the displacements, the deformed cross-section maintains its original shape under the loading condition. The U_3 displacements are much greater in magnitude than the U_1 and U_2 displacements. The U_3 displacement of 1.39 m that corresponds to 1.8% of the blade length is generated due to the blade's weight. Since stresses caused by the magnitudes of the displacements in the blade are much lower than materials' allowables, no damage in the blade is observed under gravitational loads. Therefore, gravitational loads are not considered as operational loads in the static analyses.

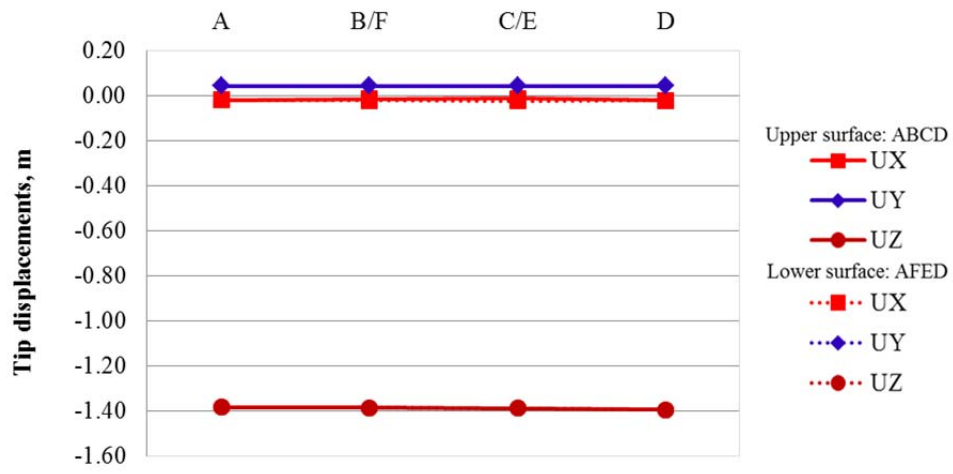


Figure D.1. Tip displacements due to the blade's weight.

APPENDIX E

Since the CEL approach is associated with mesh dependence, the convergence study for the optimal ratio of Lagrangian to Eulerian elements is demanded in order to describe a more realistic bird impact behavior. A bird is represented by EC3D8R Eulerian elements whereas a blade is modeled with Lagrangian S4R shell elements.

Impact Model Description

The blade geometry for this study is extracted as the last 5 m long section of the 80 m full-length blade [70, 72]. Thus at the origin, the chord length is 2.41 m, and the blade thickness is 0.417 m. At the blade tip, these dimensions taper to 2.08 m and 0.333 m for the chord length and blade thickness, respectively.

The simple isotropic blade has an ellipse as its cross-section with uniform wall thickness of 0.011 m and is constructed of an isotropic material. This is not reinforced by spar cap, shear web, and sandwich construction as presented in Figure E.1. The major and minor axes of the ellipse, respectively, correspond to the chord length and blade thickness of the extracted blade section as described above.

A 2 kg gelatin bird with a simplified bird geometry is employed for this study. The geometrical shape, dimension, and material behavior of the bird are described in Section 3.3.2. The 2kg-bird is assumed to have a translational velocity of 81.375 m/s along the Y-axis. The impact location is at the leading edge of $X = 77.5$ m as seen in Figure E.1. The three rotational and three displacement degrees of freedom are

constrained at $X = 75$ m. No initial stresses and displacements are applied to the blade. A general contact algorithm, which automatically detects which surfaces and edges come into contact, with a penalty method and frictionless surface is employed in the simulations [47, 82].

The blade model depicted with Lagrangian S4R shell elements is selected to assess the simulation development. Four mesh sizes (0.2 m, 0.1 m, 0.05 m, and 0.02 m along the X-axis) for Lagrangian elements are utilized to perform Lagrangian mesh convergence study while a common size of 0.01 m is used for the Eulerian domain of all models, as summarized in Table E.1. On the other hand, four Eulerian mesh sizes (0.1 m, 0.05 m, 0.02 m, and 0.01 m) are employed with a common Lagrangian mesh size of 0.02 m for the blade in order to investigate the influence of Eulerian mesh sizes on results, as summarized in Table E.2. Note that LM-0.02 and EM-0.01 Models are identical, and the model is referred as different model names for comparison purpose.

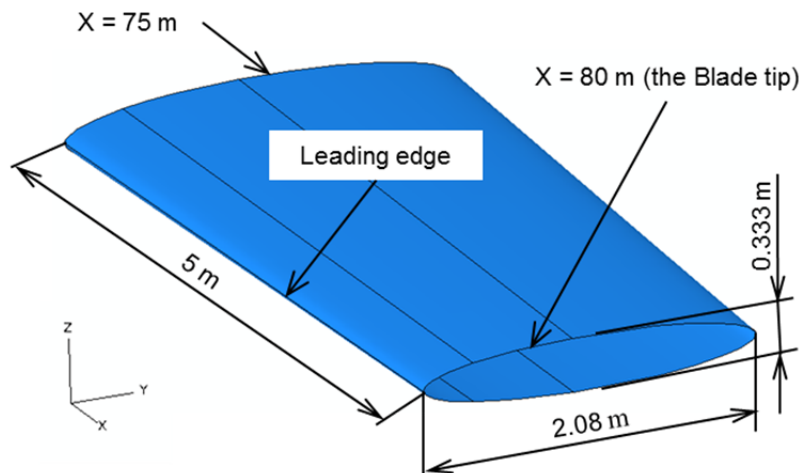


Figure E.1. Dimensions of the simplified partial blade.

Table E.1. Lagrangian mesh size variables

Model type	Mesh size (m)		Ratio of LM/EM
	Lagrangian (LM)	Eulerian (EM)	
LM-0.2	0.2	0.01	20
LM-0.1	0.1	0.01	10
LM-0.05	0.05	0.01	5
LM-0.02	0.02	0.01	2

Table E.2. Eulerian mesh size variables

Model type	Mesh size (m)		Ratio of LM/EM
	Lagrangian (LM)	Eulerian (EM)	
EM-0.1	0.02	0.10	0.2
EM-0.05	0.02	0.05	0.4
EM-0.02	0.02	0.02	1
EM-0.01	0.02	0.01	2

Results for the convergence study

Eulerian Volume Fraction Histogram

At the event of the bird (gel) impact, the motional states of the gel are described by Eulerian volume fractions (EVF). The mass of the bird, which is calculated from Equation (3.6) and the results of EVF, for Lagrangian and Eulerian mesh convergence study is plotted along time in Figures E.2 and E.3, respectively. Since all models on the Lagrangian mesh convergence study the same dimensions and mesh density of the Eulerian domain, the bird mass for all models is 2.01 kg. Generally, the mass of the bird is conserved during the analysis. However, the mass decreases as a function of the time

after the gel moves outside the domain. The mass in LM-0.2, LM-0.1, and LM-0.05 models starts leaking from the domain at 0.006s, 0.006s, and 0.0055s, respectively. At 0.010s, the mass loss for LM-0.2, LM-0.1, and LM-0.05 models corresponds to 28%, 45%, and 15% of the initial mass, respectively. LM-0.02 model shows its mass leaks from the domain at 0.006s, and the reduction of 4% is seen at 0.010s.

Additionally, it is found from the Eulerian mesh convergence study that coarse Eulerian meshes lead to an increase in bird mass at 0.0005s and thus an increase in kinetic energy of the bird. While the bird mass of EM-0.1 model at 0.0005s increases by 5.7% compared to its initial mass, EM-0.02 and EM-0.01 models show less than 0.5% difference between the masses at 0s and 0.0005s. Also, the bird mass for all models varies dependently on a mesh density of the domain.

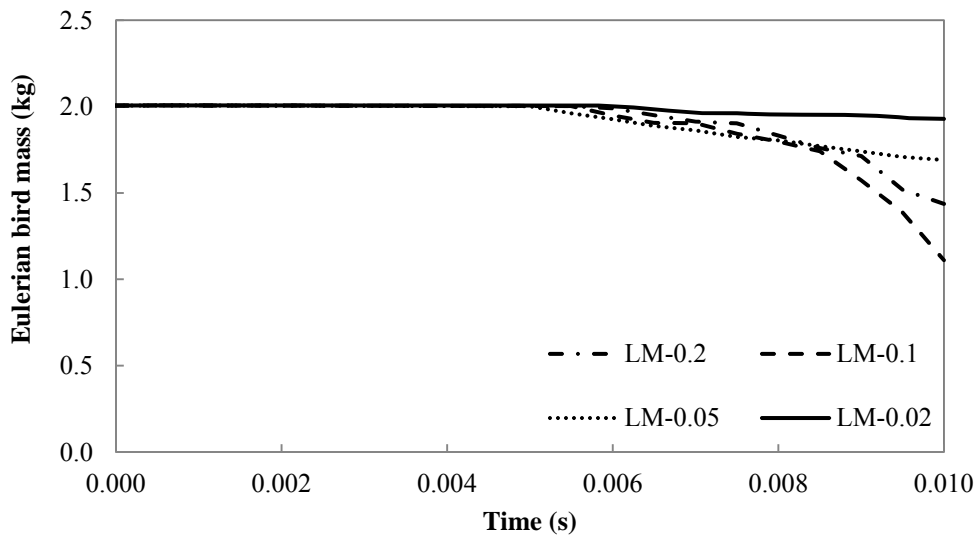


Figure E.2. Bird mass for Lagrangian mesh convergence study.

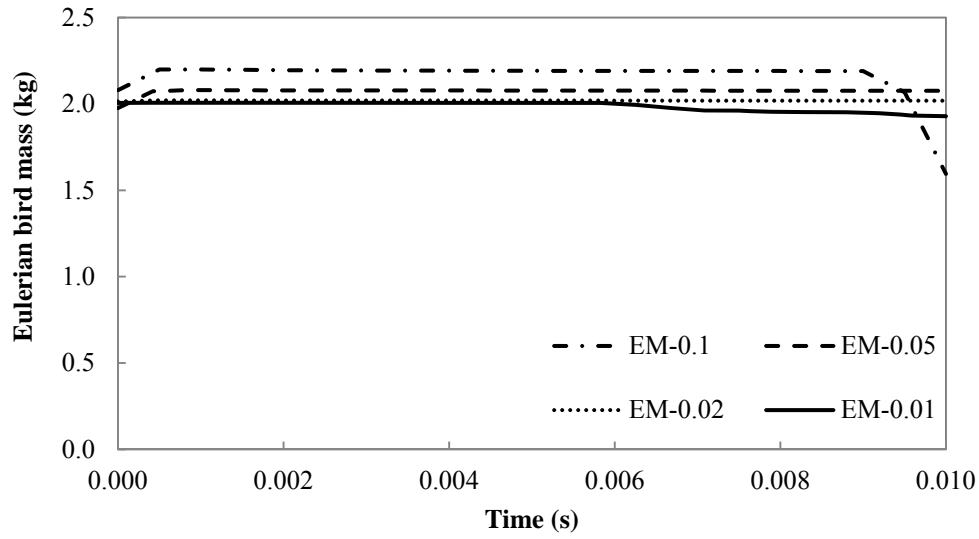


Figure E.3. Bird mass for Eulerian mesh convergence study.

Total Energy Balance

The total energy balance of the whole system containing the blade and Eulerian domain is selected as a parameter to check convergence of the results. The results for Lagrangian and Eulerian mesh convergence study are presented as a function of time in Figures E.4 and E.5. The total energy consists of the kinetic energy, internal energy, energy dissipated by the contact, and energy dissipated by bulk viscous effects. Generally, the total energy of a system is not conserved in impact problems due to heat generation and acoustic energy. However, the total energy in these simulations has to be conserved since adiabatic and non-acoustic conditions are not taken into account. As shown in Figure E.4, the energy balance for LM-0.02 model is almost constant. The other three models show a decrease in energy balance. Since the leakage of the gel occurs, the total energy balance for the three models also decreases significantly. It is

seen in Figure E.5 that Eulerian mesh sizes alter that the total energy balance of the whole system due to an increase in bird mass.

The differences in total energy balance among all models on Lagrangian mesh convergence study are attributed to the mesh density of the blade. This difference is diminished as the ratio of Lagrangian to Eulerian elements becomes smaller only if there is a fine meshed Eulerian domain. Finer meshes of the blade generate more nodes on the contact surface where the energy transfer between the blade and Eulerian domain is performed. Thus, the blade with finer mesh embodies the contact surface more efficiently. In this mesh refinement study, the blade with the finest mesh (LM-0.02 model) demonstrates the best energy balance.

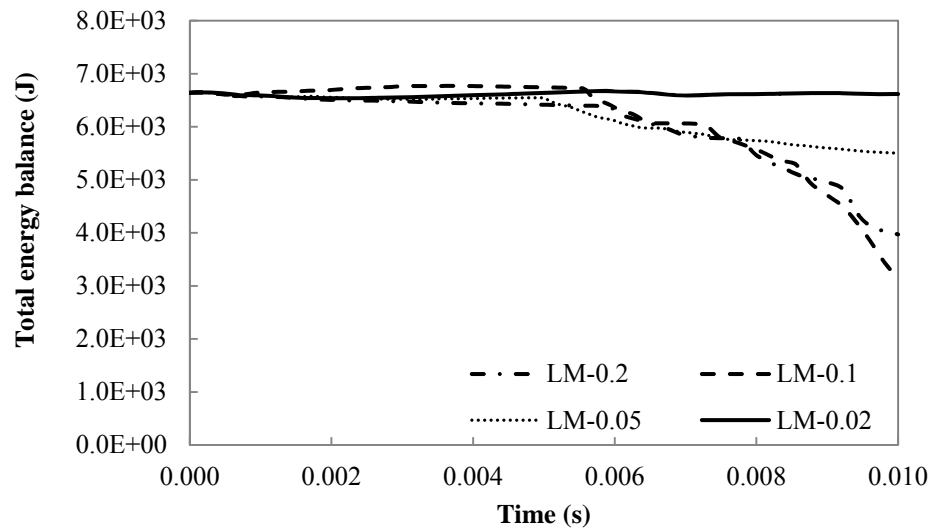


Figure E.4. Total energy balance of the whole system for Lagrangian mesh convergence study.

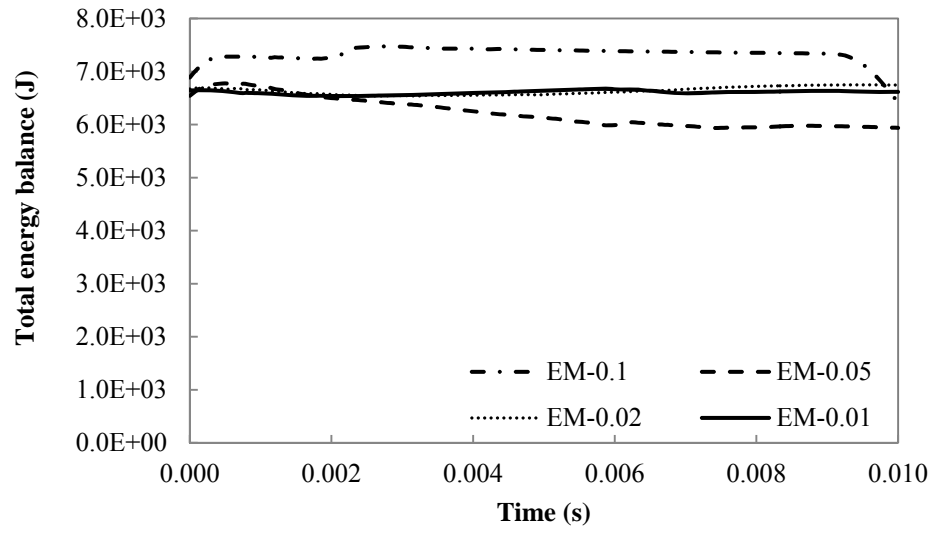


Figure E.5. Total energy balance of the whole system for Eulerian mesh convergence study.

APPENDIX F

Analysis Description

To confirm compressive stress state in the joint region of the MB Model, the axial forces generated by cable mechanisms are applied for the MB Model with virgin stress states (*i.e.*, no aerodynamic and centrifugal forces).

Since the MB model utilizes shell elements, the axial forces are assigned as line loads based on the S_{11} stresses multiplied by shell thickness. These loads for the analysis are summarized in Table F.1. The line loads are applied at $r = 40.05$ m where the joint region transitions to the reinforcement region as seen in Figure F.1 while the three rotations and displacements are fully constrained at one end of the reinforcement region in the inboard module ($r = 36.9$ m). The nodes where the line loads are applied are double nodes that enable line loads to be assigned in the FE model. The double nodes at $r = 40.05$ m are constrained with *TIE control.

Table F.1. Loads for the analysis

Location	Axial forces (N)	Line loads (N/m)
Lower Joint-BS/SC	3.49×10^6	2.36×10^6
Upper Joint-BS/SC	3.23×10^6	2.20×10^6
Joint-FSW	2.22×10^6	2.16×10^6
Joint-ASW	3.84×10^6	3.23×10^6

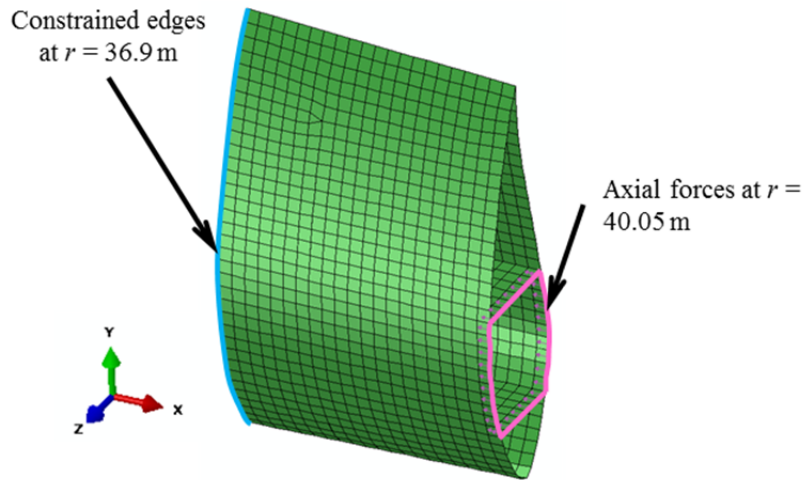


Figure F.1. Boundary and loading conditions for the analysis.

Results of The MB Model with axial forces

The most important parameter in the analysis is S_{11} stress, and it is used to confirm if compression is generated in the joint region. S_{11} stress contour in the innermost layer of the joint region of the MB Model is presented in Figure F.2. The joint region experiences S_{11} stress in the range from -47.0 MPa to -164 MPa. The stresses develop in response to the taper geometry and the complex cross-sectional geometry of the joint region. The highest stresses appear near the edge of Joint-ASW where the line load is applied. The applied load for the Joint-ASW is much greater in magnitude than the loads for the other joint regions.

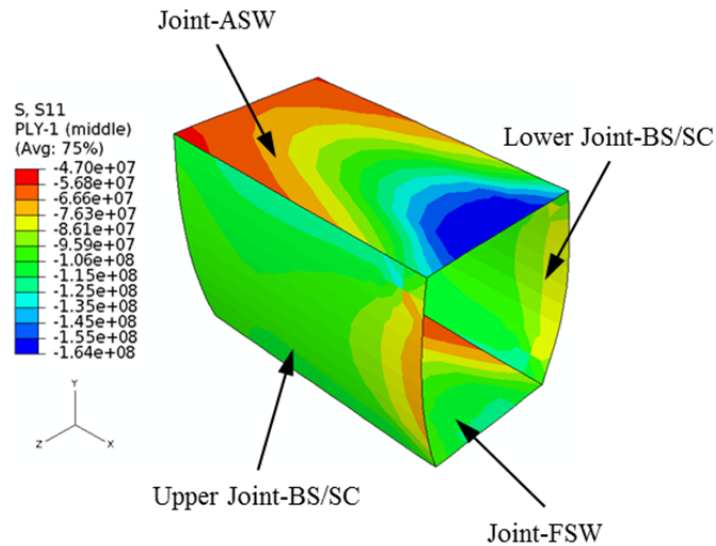
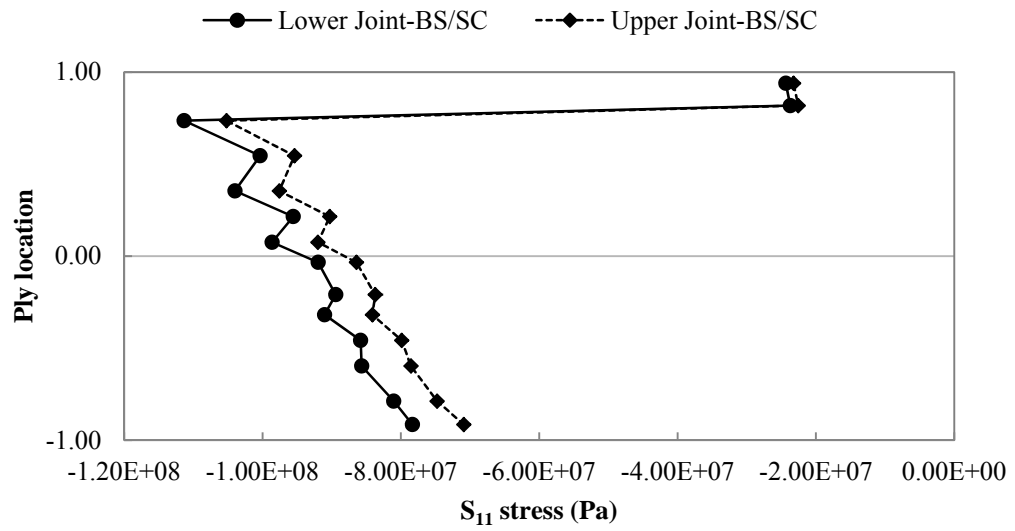
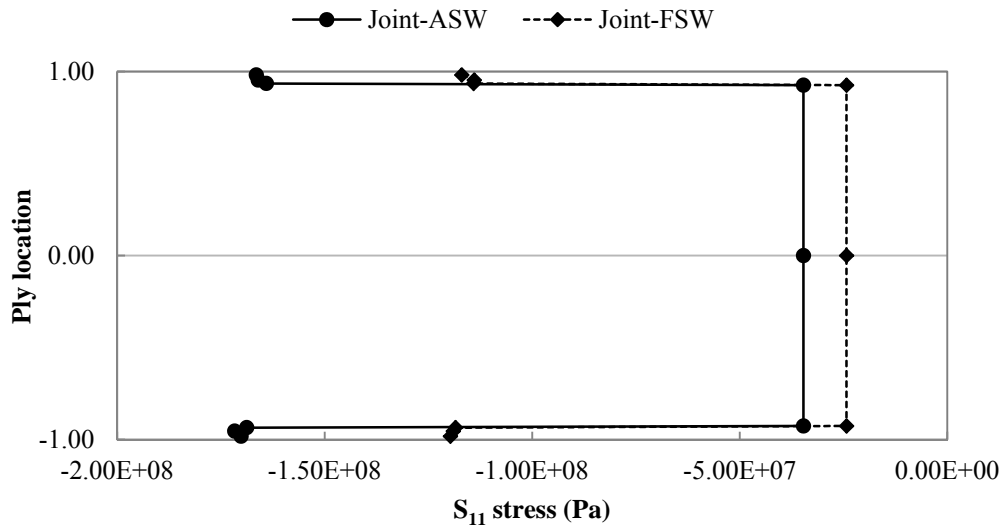


Figure F.2. S_{11} stress contour in the innermost layer of the joint region of the MB Model experiencing the axial forces.

Further examination in S_{11} stress distribution is performed, and S_{11} stress distribution through shell thickness in the joint region is presented in Figure F.3. The upper and lower Joint-BS/SC regions experience compression through the shell thickness. S_{11} stress distribution through shell thickness for the upper Joint-BS/SC region range between -22.6MPa to -105 MPa while the lower Joint-BS/SC region is subjected to S_{11} stress between -23.7 MPa to -111 MPa. The maximum compressive S_{11} stress in the lower Joint-BS/SC region is below the required stress level (71.6 MPa) to create a joint region.



(a)



(b)

Figure F.3. S_{11} stress distribution through shell thickness in the joint region: (a) Joint-BS/SC region, and (b) Joint-SW region.

The stress distributions are not matched between the lower and upper BS/SC regions since there is not symmetry in the shell surface geometry and the applied loading conditions between the upper and lower BS/SC regions. It is found in Figure F.3(b) that the S_{11} stress distribution between -120 MPa and -24.3 MPa is presented in the Joint-FSW region, and the S_{11} stress in the Joint-ASW region ranges from -170 MPa to -34.7 MPa. Compressive stresses along the shell thickness are presented in both the Joint-FSW and Joint-ASW regions, and the magnitude of the compressive stresses is greater than the required stress. Consequently, the overlapped region of the inboard and outboard modules is rigidly connected, leading to the formation of the joint region in the MB Model.